

AD-A195 760

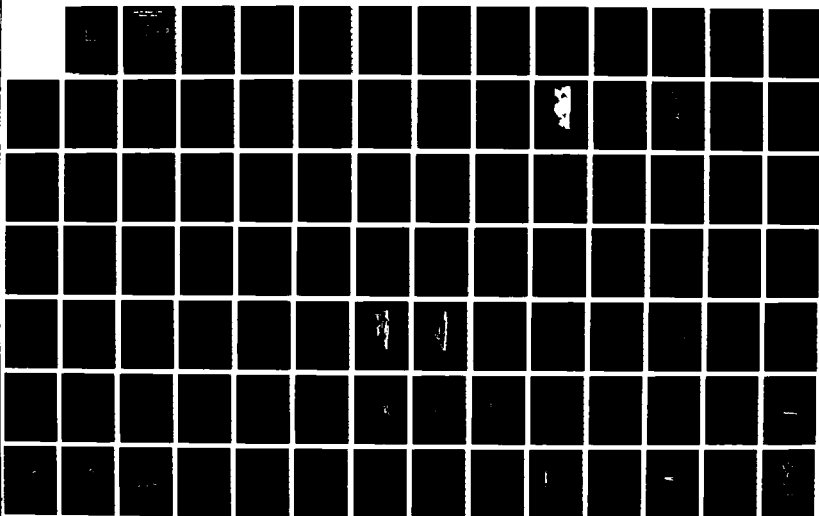
AN ANALYSIS OF RESULTS OF A HIGH-RESOLUTION WORLD OCEAN
CIRCULATION MODEL(U) NAVAL POSTGRADUATE SCHOOL MONTEREY
CA W A BARTON MAR 88

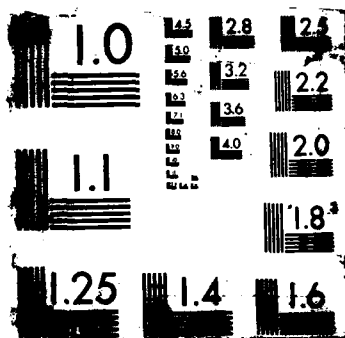
1/2

UNCLASSIFIED

F/G 8/3

NL





AD-A195 760

DTIC FILE COPY

(2)

NAVAL POSTGRADUATE SCHOOL Monterey, California



DTIC
ELECTE
JUN 14 1988
S H D

THESIS

AN ANALYSIS OF RESULTS
OF
A HIGH-RESOLUTION WORLD OCEAN CIRCULATION MODEL

by

Wesley A. Barton

March 1988

Thesis Advisor:

Albert J. Semtner, Jr.

Approved for public release; distribution is unlimited.

88 6 18 16 9

UNCLASSIFIED

SECURITY CLASSIFICATION OF THIS PAGE

REPORT DOCUMENTATION PAGE

AD-815 760

1a. REPORT SECURITY CLASSIFICATION UNCLASSIFIED			1b. RESTRICTIVE MARKINGS		
2a. SECURITY CLASSIFICATION AUTHORITY			3. DISTRIBUTION/AVAILABILITY OF REPORT Approved for public release; distribution is unlimited		
2b. DECLASSIFICATION/DOWNGRADING SCHEDULE					
4. PERFORMING ORGANIZATION REPORT NUMBER(S)			5. MONITORING ORGANIZATION REPORT NUMBER(S)		
6a. NAME OF PERFORMING ORGANIZATION Naval Postgraduate School		6b. OFFICE SYMBOL (If applicable) 68		7a. NAME OF MONITORING ORGANIZATION Naval Postgraduate School	
6c. ADDRESS (City, State, and ZIP Code) Monterey, CA 93943-5000			7b. ADDRESS (City, State, and ZIP Code) Monterey, CA 93943-5000		
8a. NAME OF FUNDING/SPONSORING ORGANIZATION National Science Foundation		8b. OFFICE SYMBOL (If applicable)		9. PROCUREMENT INSTRUMENT IDENTIFICATION NUMBER	
8c. ADDRESS (City, State, and ZIP Code)			10. SOURCE OF FUNDING NUMBERS		
PROGRAM ELEMENT NO.		PROJECT NO.		TASK NO.	
				WORK UNIT ACCESSION NO.	
11. TITLE (Include Security Classification) AN ANALYSIS OF RESULTS OF A HIGH-RESOLUTION WORLD OCEAN CIRCULATION MODEL (UNCLASSIFIED)					
12. PERSONAL AUTHOR(S) Barton, Wesley A.					
13a. TYPE OF REPORT Master's Thesis		13b. TIME COVERED FROM TO		14. DATE OF REPORT (Year, Month, Day) 1988 March	
15. PAGE COUNT 163					
16. SUPPLEMENTARY NOTATION The views expressed in this thesis are those of the author and do not reflect the official policy or position of the Department of Defense or the U.S.					
17. COSATI CODES			18. SUBJECT TERMS (Continue on reverse if necessary and identify by block number)		
FIELD	GROUP	SUB-GROUP	One-half-degree resolution; twenty levels; realistic physics, geometry, and forcing; robust-diagnostic strategy; strong advective features; fronts and meanders; meridional heat and		
19. ABSTRACT (Continue on reverse if necessary and identify by block number) The results of a highly vectorized and multitasked model of the world ocean circulation have been analyzed. This model employs realistic physics, geometry, and forcing on a high-resolution grid. The model was run on the NCAR Cray X-MP/48 using a robust-diagnostic strategy. Twenty years of model integration using one-half degree horizontal resolution and 20 levels of vertical resolution were accomplished after 200 wall-clock hours at a maximum FORTRAN performance speed of 450 megaflops. Seven key regions of the world ocean were analyzed using an ocean model processor. A representation of the global ocean circulation emerged that compared well with observations and that included strong advective features, fronts, and subtropical meanders. A diagnostic analysis program was developed to analyze meridional heat and volume transports. The results in all basins appear to be reasonable when compared to the results of other studies. For example, an anomalous northward heat transport of 3.8×10^{14} W at 30 S in the South Atlantic compares favorably with the estimate of 4.2×10^{14} W at 32 S by Bennett (1978) using hydrographic data. The results of the					
20. DISTRIBUTION/AVAILABILITY OF ABSTRACT <input checked="" type="checkbox"/> UNCLASSIFIED/UNLIMITED <input type="checkbox"/> SAME AS RPT <input type="checkbox"/> DTIC USERS			21. ABSTRACT SECURITY CLASSIFICATION Unclassified		
22a. NAME OF RESPONSIBLE INDIVIDUAL Albert J. Semtner, Jr.			22b. TELEPHONE (Include Area Code) (408) 646-3267		22c. OFFICE SYMBOL 68Se

DD FORM 1473, 34 MAR

82 APR edition may be used until exhausted.
All other editions are obsolete

SECURITY CLASSIFICATION OF THIS PAGE

U.S. Government Printing Office: 1985-5/17-0-57

UNCLASSIFIED

UNCLASSIFIED

SECURITY CLASSIFICATION OF THIS PAGE

Block 18 - SUBJECT TERMS (continued)

volume transports

Block 19 - ABSTRACT (continued)

simulations conducted in this study can be compared and contrasted against the results of future eddy-resolving simulations.



Accession For	
NTIS GRA&I	<input checked="checked" type="checkbox"/>
DTIC TAB	<input type="checkbox"/>
Unannounced	<input type="checkbox"/>
Justification	
By	
Distribution/	
Availability Codes	
Dist	Avail and/or Special
A-1	

UNCLASSIFIED

SECURITY CLASSIFICATION OF THIS PAGE

Approved for public release; distribution is unlimited

An Analysis of Results
of
A High-Resolution World Ocean Circulation Model

by

Wesley A. Barton
Lieutenant Commander, United States Naval Reserve
B.S., Rensselaer Polytechnic Institute, 1977

Submitted in partial fulfillment of the
requirements for the degree of

MASTER OF SCIENCE IN METEOROLOGY AND OCEANOGRAPHY

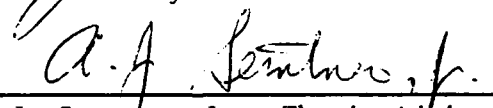
from the

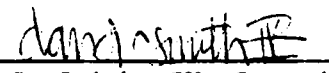
NAVAL POSTGRADUATE SCHOOL
March 1988

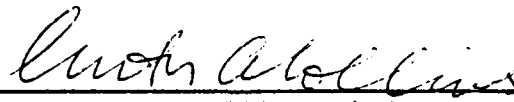
Author:



Wesley A. Barton

Approved by:


A. J. Semtner, Jr., Thesis Advisor


D. C. Smith, IV, Second Reader


C. A. Collins, Chairman
Department of Oceanography


Gordon E. Schacher
Dean of Science and Engineering

ABSTRACT

The results of a highly vectorized and multitasked model of the world ocean circulation ^{were} ~~have been~~ analyzed. This model, ^{which uses} ~~employs~~ realistic physics, geometry, and forcing on a high-resolution grid. The model was run on the NCAR Cray X-MP/48 using a robust-diagnostic strategy. Twenty years of model integration using one-half degree horizontal resolution and 20 levels of vertical resolution were accomplished after 200 wall-clock hours at a maximum FORTRAN performance speed of 450 megaflops. Seven key regions of the world ocean were analyzed using an ocean model processor. A representation of the global ocean circulation emerged that compared well with observations and that included strong advective features, fronts, and subtropical meanders. A diagnostic analysis program was developed to analyze meridional heat and volume transports. The results in all basins appear to be reasonable when compared to the results of other studies. For example, an anomalous northward heat transport of 3.8×10^{14} W at 30°S in the South Atlantic compares favorably with the estimate of 4.2×10^{14} W at 32°S by Bennett (1978) using hydrographic data. The results of the simulations conducted in this study can be compared and contrasted against the results of future eddy-resolving simulations. Keywords: Digital simulation; Advection; Heat transport;

Meridional volume transport Oceanographic fronts, etc. (Theses, etc.)
(Thermohaline, wind difference transport)

TABLE OF CONTENTS

I.	INTRODUCTION.....	1
II.	METHODOLOGY.....	4
A.	MODEL DESCRIPTION.....	4
1.	World Ocean Model.....	4
a.	Model Equations.....	4
b.	Domain and Boundary Conditions.....	5
c.	Resolution.....	7
d.	Finite Differencing Schemes.....	10
e.	Computational Efficiency.....	11
2.	Ocean Model Processor.....	11
3.	Diagnostic Analysis Program.....	12
a.	Meridional Heat Transport Formulation.....	13
b.	Meridional Volume Transport Formulation.....	14
B.	SPECIFIC EXPERIMENTAL CONDITIONS.....	15
1.	Robust-Diagnostic Strategy.....	15
2.	One Degree, Twenty Level Experiments.....	16
a.	Baseline (Laplacian Mixing) Integration.....	16
b.	Isopycnal Mixing Integration.....	18
3.	One-Half Degree, Twenty Level Experiments.....	18
a.	Baseline (Three Year Interior Restoring) Integration.....	18
b.	Free Thermocline Integration.....	19

III.	RESULTS AND DISCUSSION.....	20
A.	ONE DEGREE, TWENTY LEVEL EXPERIMENTS.....	21
1.	Baseline (Laplacian Mixing) Integration.....	21
2.	Isopycnal Mixing Integration.....	34
B.	ONE-HALF DEGREE, TWENTY LEVEL EXPERIMENTS.....	36
1.	Baseline (Three Year Interior Restoring) Integration.....	36
2.	Free Thermocline Integration.....	39
IV.	SUMMARY AND CONCLUSIONS.....	112
	APPENDIX: MERIDIONAL HEAT AND VOLUME TRANSPORT PLOTS.....	116
	LIST OF REFERENCES.....	141
	INITIAL DISTRIBUTION LIST.....	144

LIST OF TABLES

1. SEQUENCE OF EXPERIMENTS.....	17
2. GLOBAL MERIDIONAL HEAT TRANSPORT COMPARISON.....	42
3. INDIAN-PACIFIC MERIDIONAL HEAT TRANSPORT COMPARISON.....	43
4. ATLANTIC MERIDIONAL HEAT TRANSPORT COMPARISON.....	44

LIST OF FIGURES

2.1	Model domain.....	6
2.2	Bottom topography interpolated to the model grid. Bottom depth is contoured in units of km.....	8
2.3	Mean annual wind stresses of Hellerman and Rosenstein (1983) interpolated to the model grid in units of 0.1 dyn cm^{-2} in the (a) x and (b) y directions.....	9
3.1	Global overview of potential temperature in $^{\circ}\text{C}$ at 12.5 m depth for experiment 1.....	45
3.2	Global overview of horizontal volume transport in $\text{Sv}(-10^{12} \text{ cm}^3 \text{ s}^{-1})$ for experiment 1.....	46
3.3	Global overview of streamline flow at 62.5 m depth for experiment 1.....	47
3.4	Global overview of streamline flow at 12.5 m depth for experiment 1.....	48
3.5	Potential temperature in $^{\circ}\text{C}$ at 37.5 m depth in the Gulf Stream region for experiment 1.....	49
3.6	Fixed-length current vectors (with superimposed speed contours in cm s^{-1}) at 62.5 m depth in the Gulf Stream region for experiment 1.....	50
3.7	Horizontal volume transport in $\text{Sv}(-10^{12} \text{ cm}^3 \text{ s}^{-1})$ in the Gulf Stream region for experiment 1.....	51
3.8	Streamlines at 37.5 m depth in the Gulf Stream region for experiment 1.....	52
3.9	Streamlines at 1542.5 m depth in the Gulf Stream region for experiment 1.....	53
3.10	Potential temperature in $^{\circ}\text{C}$ at 62.5 m depth in the Kuroshio Current region for experiment 1.....	54
3.11	Fixed-length current vectors (with superimposed speed contours in cm s^{-1}) at 62.5 m depth in the Kuroshio Current region for experiment 1.....	55

3.12	Horizontal volume transport in $Sv(-10^{12} \text{ cm}^3 \text{ s}^{-1})$ in the Kuroshio Current region for experiment 1.....	56
3.13	Streamlines at 37.5 m depth in the Kuroshio Current region for experiment 1.....	57
3.14	Streamlines at 1542.5 m depth in the Kuroshio Current region for experiment 1.....	58
3.15	Horizontal volume transport in $Sv(-10^{12} \text{ cm}^3 \text{ s}^{-1})$ in the Drake Passage region for experiment 1.....	59
3.16	Fixed-length current vectors (with superimposed speed contours in cm s^{-1}) at 12.5 m depth in the Drake Passage region for experiment 1.....	60
3.17	Potential temperature in $^{\circ}\text{C}$ at 37.5 m depth in the Drake Passage region for experiment 1.....	61
3.18	Potential temperature in $^{\circ}\text{C}$ at 37.5 m depth in the East Australian Current region for experiment 1.....	62
3.19	(a) Meridional and (b) zonal velocity in cm s^{-1} at 12.5 m depth in the East Australian Current region for experiment 1.....	63
3.20	Horizontal volume transport in $Sv(-10^{12} \text{ cm}^3 \text{ s}^{-1})$ in the East Australian Current region for experiment 1.....	64
3.21	Streamlines at 62.5 m depth in the East Australian Current region for experiment 1.....	65
3.22	Potential temperature in $^{\circ}\text{C}$ at 37.5 m depth in the Agulhas Current region for experiment 1.....	66
3.23	Zonal velocity in cm s^{-1} at 12.5 m depth in the Agulhas Current region for experiment 1.....	67
3.24	Meridional velocity in cm s^{-1} at 12.5 depth in the Agulhas Current region for experiment 1.....	68
3.25	Horizontal volume transport in $Sv(-10^{12} \text{ cm}^3 \text{ s}^{-1})$ in the Agulhas Current region for experiment 1.....	69
3.26	Streamlines at 37.5 m depth in the Agulhas Current region for experiment 1.....	70
3.27	Horizontal volume transport in $Sv(-10^{12} \text{ cm}^3 \text{ s}^{-1})$ in the western Australia region for experiment 1.....	71

3.28	Zonal cross-section of potential temperature in °C at 30.5°S latitude off of western Australia for experiment 1.....	72
3.29	Zonal cross-section of zonal velocity in cm s ⁻¹ at 30.0°S latitude off of western Australia for experiment 1....	73
3.30	Zonal cross-section of meridional velocity in cm s ⁻¹ at 30.0°S latitude off of western Australia for experiment 1....	74
3.31	Zonal cross-section of salinity in units of 0.1 PPT at 30.5°S latitude off of western Australia for experiment 1....	75
3.32	Meridional cross-section of potential temperature in °C at 179.5°W longitude for experiment 1.....	76
3.33	Zonal cross-section of potential temperature in °C at 0.5°S latitude in the Pacific Ocean for experiment 1.....	77
3.34	Meridional cross-section of zonal velocity in cm s ⁻¹ at 180.0° longitude in the equatorial Pacific region for experiment 1.....	78
3.35	Zonal cross-section of zonal velocity in cm s ⁻¹ at 0.0° latitude in the Pacific Ocean for experiment 1.....	79
3.36	Global overview of potential temperature difference (experiment 1 results minus annual mean Levitus data) in units of 0.1°C at 62.5 m depth.....	80
3.37	Global meridional heat transport for experiment 1.....	81
3.38	Same as Figure 3.37 only from (a) Bryan and Lewis (1979) and (b) Meehl <i>et al.</i> (1982).....	82
3.39	Indian-Pacific meridional heat transport for experiment 1....	83
3.40	Atlantic meridional heat transport for experiment 1.....	84
3.41	Global meridional volume transport in units of 10 ¹¹ cm ³ s ⁻¹ for experiment 1.....	85
3.42	Same as Figure 3.41 only in units of 10 ¹² cm ³ s ⁻¹ for (a) observed values of Gordon (1971), (b) modeled values of Cox (1975), and (c) modeled values of Bryan and Lewis (1979).....	86
3.43	Indian-Pacific meridional volume transport in units of 10 ¹¹ cm ³ s ⁻¹ for experiment 1.....	87
3.44	Atlantic meridional volume transport in units of 10 ¹¹ cm ³ s ⁻¹ for experiment 1.....	88

3.45	Zonal cross-section near 16°S latitude in the Atlantic Ocean of (a) potential temperature in °C for experiment 1 and (b) observed temperature in °C (from Pickard and Emery, 1982).....	89
3.46	Zonal cross-section near 16°S latitude in the Atlantic Ocean of (a) salinity in units of 0.1 PPT for experiment 1 and (b) observed salinity in PPT (from Pickard and Emery, 1982).....	90
3.47	Streamlines at 5000.0 depth in the Gulf Stream region for experiment 1.....	91
3.48	Zonal cross-section of potential temperature in °C at 30.5°S latitude off of western Australia (a) for experiment 1 and (b) for experiment 2.....	92
3.49	Zonal cross-section of meridional velocity in cm s ⁻¹ at 30.0°S latitude off of western Australia (a) for experiment 1 and (b) for experiment 2.....	93
3.50	Potential temperature in °C at 37.5 m depth in the Gulf Stream region (a) for experiment 1 and (b) for experiment 3.....	94
3.51	Horizontal volume transport in Sv(-10^{12} cm ³ s ⁻¹) in the Gulf Stream region (a) for experiment 1 and (b) for experiment 3.....	95
3.52	Horizontal volume transport in Sv(-10^{12} cm ³ s ⁻¹) in the Kuroshio Current region (a) for experiment 1 and (b) for experiment 3.....	96
3.53	Horizontal volume transport in Sv(-10^{12} cm ³ s ⁻¹) in the Drake Passage region (a) for experiment 1 and (b) for experiment 3.....	97
3.54	Potential temperature in °C at 37.5 m depth in the Drake Passage region (a) for experiment 1 and (b) for experiment 3.....	98
3.55	Horizontal volume transport in Sv(-10^{12} cm ³ s ⁻¹) in the East Australian Current region (a) for experiment 1 and (b) for experiment 3.....	99
3.56	Potential temperature in °C at 37.5 m depth in the East Australian Current region (a) for experiment 1 and (b) for experiment 3.....	100
3.57	Potential temperature in °C at 37.5 m depth in the Agulhas Current region (a) for experiment 1 and (b) for experiment 3.....	101

3.58	Horizontal volume transport in $\text{Sv} (= 10^{12} \text{ cm}^3 \text{ s}^{-1})$ in the Agulhas Current region (a) for experiment 1 and (b) for experiment 3.....	102
3.59	Horizontal volume transport in $\text{Sv} (= 10^{12} \text{ cm}^3 \text{ s}^{-1})$ in the western Australia region (a) for experiment 1 and (b) for experiment 3.....	103
3.60	Potential temperature in $^{\circ}\text{C}$ at 37.5 m depth in the Gulf Stream region (a) for experiment 3 and (b) for experiment 4.....	104
3.61	Meridional cross-section of potential temperature in $^{\circ}\text{C}$ at 179.75°W longitude (a) for experiment 3 and (b) for experiment 4.....	105
3.62	Zonal cross-section of potential temperature in $^{\circ}\text{C}$ at 30.25°S latitude off of western Australia (a) for experiment 3 and (b) for experiment 4.....	106
3.63	Zonal cross-section of salinity in units of 0.1 PPT at 30.25°S latitude off of western Australia (a) for experiment 3 and (b) for experiment 4.....	107
3.64	Zonal cross-section of meridional velocity in cm s^{-1} at 30.00°S latitude off of western Australia (a) for experiment 3 and (b) for experiment 4.....	108
3.65	Potential temperature in $^{\circ}\text{C}$ at 62.5 m depth in the Kuroshio Current region (a) for experiment 3 and (b) for experiment 4.....	109
3.66	Potential temperature in $^{\circ}\text{C}$ at 37.5 m depth in the East Australian Current region (a) for experiment 3 and (b) for experiment 4.....	110
3.67	Zonal velocity in cm s^{-1} at 37.5 m depth in the Agulhas Current region (a) for experiment 3 and (b) for experiment 4.....	111
A.1	Global meridional heat transport for experiment 1.....	117
A.2	Same as Figure A.1 but for Indian-Pacific ocean basin.....	118
A.3	Same as Figure A.1 but for Atlantic ocean basin.....	119
A.4	Global meridional volume transport in units of $10^{11} \text{ cm}^3 \text{ s}^{-1}$ for experiment 1.....	120
A.5	Same as Figure A.4 but for Indian-Pacific ocean basin.....	121
A.6	Same as Figure A.4 but for Atlantic ocean basin.....	122

A.7	Global meridional heat transport for experiment 2.....	123
A.8	Same as Figure A.7 but for Indian-Pacific ocean basin.....	124
A.9	Same as Figure A.7 but for Atlantic ocean basin.....	125
A.10	Global meridional volume transport in units of $10^{11} \text{ cm}^3 \text{ s}^{-1}$ for experiment 2.....	126
A.11	Same as Figure A.10 but for Indian-Pacific ocean basin.....	127
A.12	Same as Figure A.10 but for Atlantic ocean basin.....	128
A.13	Global meridional heat transport for experiment 3.....	129
A.14	Same as Figure A.13 but for Indian-Pacific ocean basin.....	130
A.15	Same as Figure A.13 but for Atlantic ocean basin.....	131
A.16	Global meridional volume transport in units of $10^{11} \text{ cm}^3 \text{ s}^{-1}$ for experiment 3.....	132
A.17	Same as Figure A.16 but for Indian-Pacific ocean basin.....	133
A.18	Same as Figure A.16 but for Atlantic ocean basin.....	134
A.19	Global meridional heat transport for experiment 4.....	135
A.20	Same as Figure A.19 but for Indian-Pacific ocean basin.....	136
A.21	Same as Figure A.19 but for Atlantic ocean basin.....	137
A.22	Global meridional volume transport in units of $10^{11} \text{ cm}^3 \text{ s}^{-1}$ for experiment 4.....	138
A.23	Same as Figure A.22 but for Indian-Pacific ocean basin.....	139
A.24	Same as Figure A.22 but for Atlantic ocean basin.....	140

ACKNOWLEDGEMENTS

In the words of Moses, "You may say to yourself, 'My power and the strength of my hands have produced this wealth for me.' But remember the Lord your God, for it is He who gives you the ability to produce wealth..." God has graciously given me the strength to complete this thesis through the guidance, patience, and support of many people. I would first like to thank my advisor, Professor Albert J. Semtner--for many long hours of teaching, advising, and answering my questions; and for allowing me to share the excitement of his world ocean circulation model. I would next like to thank the co-author of this model, Dr. Robert M. Chervin of the National Center for Atmospheric Research (NCAR)--for his faithful production runs of the world ocean model, on which this thesis is based; and for his assistance in tailoring my diagnostic analysis program for the Cray X-MP/48. Mr. Thomas W. Bettge of NCAR also provided invaluable assistance through his responsive updates to the ocean model processor and through his patient guidance concerning NCAR graphics. Thank you, too, to Professor David C. Smith, IV, who graciously substituted for my planned second reader (away on travel); and to Miss Jeannie E. Bennett, who saved me many hours of time (and frustration) by preparing this manuscript on a word processor.

My wife, Denise, deserves much of the credit for this thesis--for keeping the home fires burning (with two small babies); and for

encouraging me with her smile. Thank you, too, to my daughters Laura and Kelly--for giving up their daddy many evenings and weekends.

This research was sponsored by a grant (agreement number ATM-8705980) from the National Science Foundation. NCAR generously provided many, many hours of computer resources in support of this research.

I. INTRODUCTION

For as long as man has plied the seas he has sought to understand the behavior of the ocean as it affects his vessel. The effects of wind-generated waves and circulations have been of concern to every sailor and every mission. With the advent of submarine warfare in the twentieth century, man's interest in the ocean extended to beneath the surface and to synoptic-scale oceanic phenomena such as fronts and eddies. Since World War II, the effects of increased urbanization on global climate have also necessitated a better understanding of the ocean's ability to buffer large-scale climate changes.

While man has long known the geophysical fluid dynamic equations that govern world ocean circulation, he has historically suffered from a lack of observational data and analytical techniques for solving these nonlinear equations. The development of numerical solution techniques and computer technology after World War II brought numerical solutions within reach of meteorologists, but not physical oceanographers. Physical considerations require that oceanic model resolution be ten times as great in each horizontal coordinate and that time integrations be tenfold as long as those in atmospheric modeling. As a result, physical oceanographers of the 1960's and 1970's were constrained to limited-domain, coarse grid, or filtered model ocean simulations. Only recently, in the mid-1980's, has the problem facing physical oceanographers become tractable through recent

advances in observational techniques, both in-situ and remote (especially satellite), and in supercomputer technology.

Dr. Albert J. Semtner, Jr. of the Naval Postgraduate School (NPS) and Dr. Robert M. Chervin of the National Center for Atmospheric Research (NCAR) have developed a high-resolution world ocean circulation model capable of numerically solving the primitive equations using the maximum capacity of computer power currently available or likely to be available in the next several years. This model has already achieved a horizontal resolution of one-half degree and a vertical resolution of 20 levels over the world ocean using a robust-diagnostic methodology and NCAR's Cray X-MP/48 supercomputer. This time integration has produced a very realistic representation of global ocean circulation that includes strong advective features as well as fronts and meanders. The authors of this model believe that a horizontal resolution of one-third degree with 15 vertical levels is possible on the Cray X-MP/48, and that a horizontal resolution of one-fourth degree with 25 vertical levels may be possible on the Cray X-MP/416. These simulations would be fully eddy-resolving. Such impressive statistics are achieved using a computer code that is fully vectorized and that is designed for "multitasking" on multiple processors--something no other world ocean model currently can boast.

This paper reports the results of an analysis performed on the robust-diagnostic model integrations of Semtner and Chervin through February, 1988. The fields of potential temperature, horizontal velocity components, and horizontal volume transport are analyzed using the ocean model processor of Bettge (1987). This processor also

permitted the analysis of streamlines, velocity vectors, and potential temperature difference fields resulting from the one degree horizontal resolution model integrations. In addition, the author has developed a diagnostic program for analyzing meridional heat transports and meridional volume transports resulting from the various model integrations. The goal of all analysis discussed in this paper is the validation of the world ocean model of Semtner and Chervin as a viable tool for understanding world ocean circulation. Such a tool should ultimately permit the assessment of oceanic influences on climate and the forecasting of oceanic phenomena for military and civilian use.

Chapter II of this paper discusses the basic methodology used in this study; including descriptions of the world ocean model, the ocean model processor, and the diagnostic analysis program. Specific experimental conditions are also discussed in Chapter II. In Chapter III, the results of these specific experiments are reported and discussed as they compare to observations and to the results of other studies. Finally, in Chapter IV, the findings of this study are summarized and a track is charted for the future testing and application of the world ocean model.

II. METHODOLOGY

A. MODEL DESCRIPTION

1. World Ocean Model

The numerical model used in this analysis is a multi-level primitive equation, world ocean, general circulation model. It is essentially an update of the model of Semtner (1974). The finite-difference formulation of the world ocean model is described in Semtner (1986b). The historical development of such models and the rationale behind many of the numerical choices of this model are described in Semtner (1986a).

a. Model Equations

The governing equations in spherical coordinates are presented in Semtner (1986b). Seven variables specify the physical condition of the ocean: the x-, y-, and z- components of velocity (u , v , and w , respectively), potential temperature T , salinity S , pressure p , and density ρ . The horizontal volume transport stream function ψ_{xy} is a derived quantity that is also used to compute the barotropic component of the horizontal velocity. The ocean is assumed to be an incompressible fluid that is horizontally isotropic. Several standard approximations are used to simplify the governing equations: the thin-shell approximation, the hydrostatic approximation, and the Boussinesq approximation. Also, the Coriolis term involving w in the u momentum equation is neglected to maintain energetic consistency with the hydrostatic relation.

Eddy effects in the horizontal are parameterized using eddy viscosity and eddy diffusivity coefficients. Specific values of these coefficients are dependent on the horizontal resolution and are given in Chapter II. B. in the discussion of specific experimental conditions. Options for isopycnal mixing (in coarse-grid calculations) or biharmonic mixing (in eddy-resolving calculations) are incorporated into the model, after Cox (1984). Vertical mixing in the model is based upon the Richardson-number dependent parameterization of Pacanowski and Philander (1981).

A large-scale hydrostatic model such as this cannot handle convective processes explicitly. Therefore, a simple convective adjustment is applied in order to treat situations of static instability.

b. Domain and Boundary Conditions

The model domain includes all longitudes, and latitudes from 75°S to 65°N (Figure 2.1). East and west boundaries are cyclically continuous. North and south boundaries are closed. This northern restriction thus neglects the exchange of waters between the North Atlantic Ocean and the Arctic Ocean, as well as flow through the Bering Strait. Asia, Europe, North America, and South America are considered to comprise one interconnected, primary continent. Antarctica, Australia, and New Zealand are treated as islands. All other actual islands have been either submerged to 100 m depth or else connected to the nearest land mass. Also, a number of inland seas and shallow bays have been filled. At lateral walls, a no-slip condition ($u=v=0$) is imposed, and no flux of heat or salt is allowed.



Figure 2.1 Model domain.

Bottom topography has been interpolated to the model grid and is accommodated in the model by using a variable number of gridboxes in the vertical, stacked downward from the surface until the bottom is reached (Figure 2.2). At the ocean bottom, fluxes of heat and salt are assumed to be zero. Flow is required to parallel the bottom slope. Bottom friction is neglected.

At the ocean surface, momentum transfer is based upon the annual mean observed wind stresses of Hellerman and Rosenstein (1983) (Figure 2.3). Adopting the robust-diagnostic strategy of Sarmiento and Bryan (1982), modeled potential temperature and salinity are linearly damped to the climatological values of Levitus (1982), with a short damping time constant used at the surface and a longer damping time constant used in the ocean interior. A rigid lid approximation ($w=0$) is made at the ocean surface in order to permit a longer model time step and to filter out high frequency external gravity waves. The rigid lid condition also complicates the solution of the governing equations by creating an elliptic problem to be solved at every time step for the volume transport stream function. This problem is solved by using a successive over-relaxation procedure.

c. Resolution

Model resolution in the horizontal and in the vertical is variable within the limitations of the supercomputer employed. Uniform grid spacing in both latitude and longitude is used regardless of the horizontal resolution chosen. Vertical resolution should be adequate to resolve the vertical structure of known oceanic phenomena and to resolve the bottom topography. A stretched grid is employed to



Figure 2.2

Bottom topography interpolated to the model grid. Bottom depth is contoured in units of km.

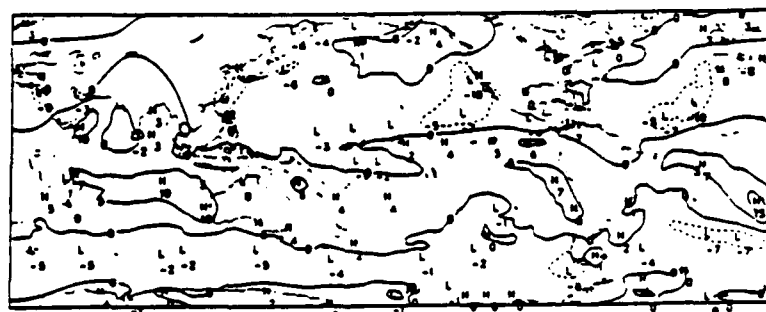
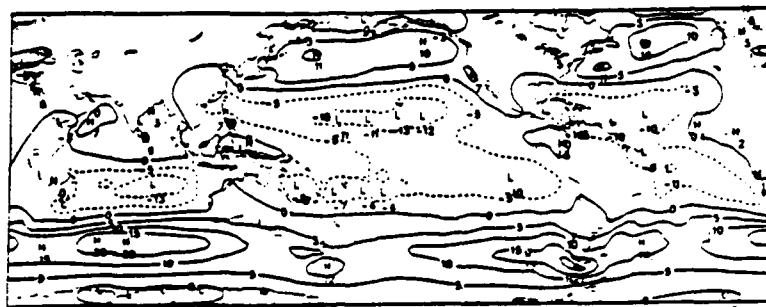


Figure 2.3 Mean annual wind stresses of Hellerman and
Rosenstein (1983) interpolated to the model
grid in units of 0.1 dyn cm^{-2} in the (a) x and
(b) y directions.

allow better resolution of upper-ocean processes regardless of the number of vertical levels chosen. Specific experimental resolutions are discussed in Chapter II. B.

d. Finite Differencing Schemes

For the most part, the energetically consistent, space-staggered B-scheme of Bryan (1969) is used for horizontal space differencing. For advective processes, this spatial differencing scheme conserves water mass, heat, salt, variance of potential temperature, variance of salinity, angular momentum, and kinetic energy as well as total energy. It does not conserve linear momentum or enstrophy (mean square vorticity). Experience has shown that the conservation of linear momentum at lateral boundaries is not critical in highly geostrophic systems such as the world ocean. The conservation of enstrophy, however, may become important in high resolution experiments in order to prevent the false computational cascade of energy to high wave numbers. With regard to the vertically averaged flow, the methods of Takano (1974) for semi-implicit treatment of the beta term and for hole relaxation of islands are generalized to the case of variable bottom topography. The pressure term can also be treated semi-implicitly for the baroclinic mode.

The model uses a leapfrog time step for advective processes and a forward time step for diffusive processes within a basic leapfrog time differencing structure. Such a time differencing scheme is simple and provides second-order accuracy. An occasional forward time step is inserted within the basic leapfrog structure in order to suppress computational mode noise. Stability considerations

dictate that the length of each time step vary with the horizontal resolution chosen. Shorter time steps are needed in higher resolution experiments.

e. Computational Efficiency

The model was designed for Cray X-MP class and other anticipated supercomputers with fast vector startup times. It is 98% vectorized in longitude across individual ocean basins and 99.6% parallel processed in latitude for four to 64 processors. Computational efficiency is also enhanced by taking a longer time step for the more slowly adjusting fields of potential temperature and salinity, and by not computing through land masses. Using the four processors and eight megaword main memory of a Cray X-MP/48 a maximum FORTRAN performance speed of 450 megaflops has been achieved.

2. Ocean Model Processor

The ocean model processor of Bettge (1987) was used as a tool to analyze data output from time integrations of the world ocean model. This processor was designed to execute within the National Center for Atmospheric Research (NCAR) Scientific Computing Division environment on Cray supercomputers using data sets that reside on the mass storage system.

The primary product from the ocean model processor is a two-dimensional contour analysis of data that was originally represented in the four dimensions of space and time. Data can be averaged over any dimension and plotted within any two-dimensional cross-section subset. For the purposes of this study, spatial cross-sections of T , u , v , and ψ_{xy} were analyzed at the time iterations of interest by

focusing on selected individual values of the excluded spatial dimension. Subsequent improvements to the ocean model processor by Bettge also permitted analysis of spatial cross-sections of streamlines, velocity vectors, and difference fields. As an example of the utility of graphic representation of difference fields, this feature facilitated the comparison of the potential temperature field at any time iteration to the climatological field of Levitus (1982).

The specific regions of the world ocean analyzed using the ocean model processor were:

- The Gulf Stream region.
- The Kuroshio Current region.
- The Drake Passage region.
- The East Australian Current region.
- The Agulhas Current region.
- The western Australia region.
- The equatorial Pacific region.

These regions were chosen first as key regions that would permit validation of the world ocean model, and second as regions of significant operational and research interest. The ocean model processor permitted graphic enlargement of these regions and the various contoured fields from the ocean model as desired. These contour plots were then compared to observed fields in an attempt to validate the world ocean model as a viable general circulation model.

3. Diagnostic Analysis Program

A diagnostic analysis program based upon the formulations of Bryan and Lewis (1979) was developed in order to assess the meridional

heat and volume transports of the world ocean and the individual ocean basins. Bryan (1982) combines the Indian and Pacific ocean basins because of work by Godfrey and Golding (1981) that suggests significant flow of surface waters from the Pacific Ocean into the Indian Ocean between Australia and southeast Asia. A similar approach is adopted in this study.

a. Meridional Heat Transport Formulation

In order to gain insight into the mechanisms of meridional heat transport in the ocean model, it is necessary to divide the total heat transport into three components. Defining $[()]$ as the zonal average of $()$, i.e.

$$[()] = \frac{1}{\Delta\lambda} \sum_{\lambda}^{\lambda+\Delta\lambda} () \delta\lambda,$$

and defining $()'$ as the departure of $()$ from the zonal average, the total meridional heat transport across a given latitude may be written as

$$HT = \rho c_p \sum_O ([T][v] + [T'v'] - A_H [\frac{\delta T}{\delta y}]) (\delta x \cos \phi) (\delta z).$$

O is the overturning component and can be attributed to ocean circulation in the meridional plane associated with wind-driven Ekman cells and with thermohaline circulations. G is the gyre component and can be attributed to flow in the horizontal plane associated with the major mid-latitude gyres. D is the diffusive component and is a parameterization of heat transport by synoptic scale eddies, which are represented only implicitly in the ocean model. The specific heat of water is c_p , A_H is the horizontal eddy diffusivity coefficient, δT is the north-south potential temperature gradient, δy is the north-south

grid spacing, δx is the east-west grid spacing at the equator, and δz is the (variable) thickness of a vertical grid box. Longitude is represented by λ , and latitude is represented by ϕ .

The meridional heat transport calculation was performed throughout the world ocean model's range of latitude at selected time iterations of interest for the global ocean. In order to maintain the condition of non-divergence during the zonal integrations for the Indian-Pacific and Atlantic ocean basins, basin heat transport calculations were performed north of 30°S only, where the basins are physically isolated from each other by Africa and South America. Next, the total heat transport results from the individual basins were summed and compared to the global ocean total heat transports (north of 30°S) in order to ensure consistency. Finally, the heat transport curves from all basins were compared to other results obtained using direct, indirect, residual, and numerical ocean model methods in an attempt to validate the world ocean model as a viable tool for studying ocean influences on climate.

b. Meridional Volume Transport Formulation

In order to better understand ocean circulation in the meridional plane, it is profitable to compute the zonally integrated volume transport stream function. At a given latitude and depth, zonal integration results in

$$\psi_{yz}(\phi, z) = \sum_0^z (F) (2\pi a \cos\phi) [v] (\delta z).$$

In this expression, a is the radius of the earth at the equator, $(2\pi a \cos\phi)$ represents the circumference of the earth at a given latitude ϕ , and F is the fraction of grid boxes at a given latitude

and depth that represent ocean (vice land). The zonally integrated circulation at a given depth z is arrived at by summing from the surface (where the volume transport is, by definition, equal to zero) down to depth z . Values at the ocean bottom were verified to be near zero.

The meridional volume transport calculation was performed throughout the world ocean model's range of latitude at selected time iterations of interest for the global ocean. The Indian-Pacific and Atlantic ocean basin calculations are performed north of 30°S only, in keeping with the reasoning already discussed for the meridional heat transport calculations. All stream function results were then subjected to a nine-point smoothing in order to reduce the effects of computational noise. Next, the results from the individual ocean basins were summed and compared to the global ocean results (north of 30°S) in order to ensure consistency. Finally, the contour plots for the global, Indian-Pacific, and Atlantic ocean basins were compared to observed meridional circulations and to the results of other numerical studies in an attempt to validate the world ocean model as a viable simulator of thermohaline and wind-driven circulations in the meridional plane.

B. SPECIFIC EXPERIMENTAL CONDITIONS

1. Robust-Diagnostic Strategy

At time zero, the world ocean is assumed to be at rest, stably stratified, and with horizontally uniform profiles of potential temperature and salinity. Near the beginning of the experimentation, a decision was made to forego fully prognostic modeling until such

time as greater computer power is available than with the Cray X-MP/48. The robust-diagnostic strategy adopted from Sarmiento and Bryan (1982) consists of linear restoring to the annual mean potential temperature and salinity values of Levitus (1982). At the surface, a restoring time constant of one month was used throughout the experimentation. In the interior of the ocean, the restoring time constant was progressively increased from experiment to experiment. Baseline integrations at each of the resolutions tested were continued until the diagnostic adjustment times of potential temperature and salinity were within two percent of full equilibrium, and until the rates of increase of baroclinic and barotropic mode energies became less than one percent of the work done by the wind stress. The sequence of experiments described below is summarized in Table 1. It is important that the reader observes the desired progress of this (and future) experimentation toward greater resolution, longer model integration time, and more fully prognostic modeling--within the limits of available supercomputer technology.

2. One Degree, Twenty Level Experiments

a. Baseline (Laplacing Mixing) Integration

In this experiment the world ocean model was integrated for four years using one degree horizontal resolution, 20 levels of vertical resolution, and Laplacian mixing. At this time an equilibrium was reached. Each wall-clock hour of computer time on the Cray X-MP/48 accomplished eight-tenths of a year of model integration time. The horizontal eddy viscosity and eddy diffusivity coefficients used were identically $2.0 \times 10^7 \text{ cm}^2 \text{ s}^{-1}$. In the interior of the

TABLE 1: SEQUENCE OF EXPERIMENTS

EXPERIMENT #	HORIZONTAL RESOLUTION	HORIZONTAL MIXING	HORIZONTAL EDDY COEFF. (VISCOSITY AND DIFFUSIVITY)	RESTORING TIME CONSTANT		MODEL INTEGRATION TIME
				25-710 m	DEEP OCEAN	
1	1°	Laplacian	$2.0 \times 10^7 \text{ cm}^2 \text{ s}^{-1}$	1 year	1 year	0 - 4 years
2	1°	Isopycnal	$2.0 \times 10^7 \text{ cm}^2 \text{ s}^{-1}$	1 year	1 year	2.8 - 4 years
3	1/2°	Laplacian	$1.0 \times 10^7 \text{ cm}^2 \text{ s}^{-1}$	3 years	3 years	0 - 10 years
4	1/2°	Laplacian	$1.0 \times 10^7 \text{ cm}^2 \text{ s}^{-1}$	None	3 years	10 - 20 years

ocean, the model employed a one year restoring time constant. Results from this experiment are presented and discussed in Chapter III. A.1.

b. Isopycnal Mixing Integration

In this experiment, isopycnal mixing replaced Laplacian mixing after 2.8 years of integration of the world ocean model. Model integration was then continued out to four years total integration time. All other aspects of this experiment were identical to the baseline (Laplacian mixing) integration. Results from this experiment are presented and discussed in Chapter III. A.2.

3. One-Half Degree, Twenty Level Experiments

a. Baseline (Three Year Interior Restoring) Integration

In this experiment, the world ocean model was integrated for ten years (one decade) using one-half degree horizontal resolution and 20 levels of vertical resolution. The restoring time constant in the interior of the ocean was relaxed from one year to three years after four years of the model integration. An equilibrium was reached after four years of integration time and then again prior to reaching the decadal mark. Each wall-clock hour of computer time on the Cray X-MP/48 accomplished one-tenth of a year of model integration time. Ten years of model integration thus consumed 100 wall-clock hours or 400 processor hours. The horizontal eddy viscosity and eddy diffusivity coefficients used were identically $1.0 \times 10^7 \text{ cm}^2 \text{ s}^{-1}$. Laplacian mixing was used throughout the model integration. Results from this experiment are presented and discussed in Chapter III. B.1.

b. Free Thermocline Integration

This experiment was essentially a continuation of the baseline (three year interior restoring) integration out to 20 years total integration time, but without robust-diagnostic forcing between 25 m and 710 m depths. The waters above the main thermocline were thus allowed to evolve prognostically within the constraints of the surface and deep forcing. All other aspects of this experiment were identical to the baseline (three year interior restoring) integration. Results from this experiment are presented and discussed in Chapter III. B.2.

III. RESULTS AND DISCUSSION

In this chapter, the most significant results of the various model integration experiments are presented and discussed. Illustrative figures and tables are consolidated at the end of this chapter. Meridional heat transport and meridional volume transport plots for all experiments and all ocean basins are contained in the Appendix. Concerning the output of the ocean model processor, the reader is advised that the appearance of a second, outer coastal outline signifies the ocean-land boundary at the specified depth. In the plots of meridional heat transport, positive values indicate northward heat transport and negative values indicate southward heat transport. In the contour plots of meridional volume transport, positive values indicate clockwise circulation and negative values indicate counterclockwise circulation. The general strategy of the author in the following discussion is to compare the one degree baseline integration results to climatology, to compare the one degree isopycnal mixing and the one-half degree baseline integration results to those of the one degree baseline integration, and to compare the one-half degree free thermocline integration results to those of the one-half degree baseline integration. Comparisons made between world ocean model results and observations are to the values and descriptions cited in Pickard and Emery (1982), except where otherwise stated. In all such comparisons the model of Semtner and Chervin is simply referred to as "the world ocean model."

A. ONE DEGREE, TWENTY LEVEL EXPERIMENTS

1. Baseline (Laplacian Mixing) Integration

A global overview of the world ocean model results after four years of integration is encouraging. The model currently depicts the Gulf Stream and the Kuroshio Extension as regions of tight isotherm packing (Figure 3.1). The volume transport field illustrates the expected dominance of the Antarctic Circumpolar Current and the major midlatitude and subarctic gyres (Figure 3.2). The flow in these gyres is vividly apparent by looking at a global plot of streamlines at 62.5 m depth (Figure 3.3). Nearer the surface, the streamline flow reveals an excellent simulation of Ekman convergences near 30°S and 30°N, and divergence near the equator (Figure 3.4) -- in keeping with the climatological wind pattern.

In the Gulf Stream region, the potential temperature field reveals the expected advection of isotherms off Cape Hatteras, corresponding to the location where the Gulf Stream leaves the coast (Figure 3.5). The model does not, however, clearly define the north wall of the Gulf Stream. A proper representation of the Gulf Stream probably requires mass exchange between the North Atlantic Ocean and the Arctic Ocean (W. Schmitz, personal communication). (In the case of the world ocean model, this mass exchanged can be accomplished by "transplanting" the Arctic Ocean grid into the unused data arrays of the primary continent, and then by coupling the Arctic grid to the North Atlantic at 65°N.) Meanwhile, increased horizontal resolution will result in some improvement in the model's Gulf Stream simulation. Plots of fixed-length current vectors with superimposed speed

contours (Figure 3.6) and volume transport (Figure 3.7) show a Gulf Stream that is somewhat weaker than expected, with a maximum speed of 73 cm s^{-1} and a maximum volume transport of 67 Sv (where $1 \text{ Sv} = 10^{12} \text{ cm}^3 \text{ s}^{-1}$) off Cape Hatteras. Again, a proper simulation of the Gulf Stream awaits inclusion of mass exchange between the North Atlantic and Arctic Oceans. The eddy-like features in the southwestern Sargasso Sea in Figure 3.7 are in fact computational noise that will be eliminated in higher resolution experiments. Streamline plots of the Gulf Stream region display the generally eastward flow of the Gulf Stream near the surface (Figure 3.8) and the generally westward flow of a very wide undercurrent below about 1500 m depth (Figure 3.9).

Results for the Kuroshio Current region are shown in Figures 3.10 (potential temperature), Figure 3.11 (current vectors), Figure 3.12 (volume transport), Figure 3.13 (streamlines near the surface), and Figure 3.14 (streamlines at about 1500 m depth). The potential temperature field shows the expected advection of isotherms as the Kuroshio Current leaves the Japanese coast at about 30°N latitude. A maximum current speed of 87 cm s^{-1} and a maximum volume transport of 91 Sv south of Japan are comparable with observed values. The streamline plots faithfully reproduce the Kuroshio Extension at the surface, but do not show a well-defined undercurrent.

In the Drake Passage, the model reveals a net volume transport for the Antarctic Circumpolar Current (ACC) of up to 180 Sv (Figure 3.15). Year-long current meter records have provided an average value of 139 Sv. Current speed is generally less than 20 cm s^{-1} , although higher values are apparent over small areas (Figure 3.16). The

complexity of the flow in this region can be attributed to very complex bottom topography as well as to computational noise (which will be reduced in higher resolution experiments). Thus, the world ocean model correctly reproduces an ACC of very large volume transport but relatively low current speed. The potential temperature field in this region also reveals a frontal region at 40°S off the South American east coast, where the Falkland and Brazil Currents meet (Figure 3.17).

In the region of the East Australian Current (EAC), the potential temperature field reveals advection of isotherms corresponding to southward flowing western boundary currents off Australia and New Zealand (Figure 3.18). Plots of the y- and x-components of velocity reveal a western boundary current that flows south along Australia at up to 40 cm s^{-1} , turns east at approximately 33°S with a speed of less than 10 cm s^{-1} , and then turns southward again along the northeast coast of New Zealand with speeds of up to 15 cm s^{-1} (Figure 3.19). The anticyclonic loop made by the EAC as it leaves the Australian coast is well depicted in the plot of volume transport, where the EAC is shown to penetrate southward to almost 40°S before turning to the northeast (Figure 3.20). The eddy-like features that appear to emanate from this anticyclonic loop are computational noise that will disappear in higher resolution experiments. Similar eddy-like features appear to the east of New Zealand. A maximum volume transport of 56 Sv off the Australian coast is consistent with an estimate cited by Kamenkovich *et al.* (1986). However, the fields of current speed and volume transport in the EAC

region have been observed to be very variable. A streamline plot at 62.5 m depth is representative in showing how the EAC turns eastward into the Tasman Sea and how the ACC remains predominantly to the south of Australia and New Zealand (Figure 3.21).

Model results for the Agulhas Current region are interesting on many accounts. First, the potential temperature field (Figure 3.22) reveals upwelling off the west coast of Africa. Second, a tightening of isotherms along 40°S corresponds to a frontal region between the Agulhas Return Current and the ACC. Third, a tongue of warm water spreading westward around the southern tip of Africa suggests at least partial flow of the Agulhas Current around Africa and into the South Atlantic Ocean. The u velocity contour plot near the surface confirms this suspicion by revealing large westward speeds (associated with the Agulhas Current) propelling warm Indian Ocean water around the southern tip of Africa (Figure 3.23). This plot also reveals a cyclonic circulation in the Indian Ocean just south of the equator -- indicating that the Southwest Monsoon dominates the wind-driven circulation on an annual mean basis. The v velocity contour plot near the surface shows the dominance of the northward-flowing Somali Current (121 cm s^{-1} maximum) and the southward-flowing Agulhas Current (66 cm s^{-1} maximum) (Figure 3.24). The volume transport plot reveals a maximum Agulhas Current transport of 84 Sv (Figure 3.25). These numbers suggest a stronger Agulhas Current than is commonly thought. The Agulhas Retroflexion (where the Agulhas Current is turned anticyclonically to the east by the ACC) is very well depicted in a near-surface streamline plot (Figure 3.26).

In the western Australia region, a volume transport of up to 20 Sv is calculated to flow southwestward between Indonesia and Australia (Figure 3.27). This value is of the same order of magnitude as the estimates of Godfrey and Golding (1981). Godfrey and Golding (1981) also suggest that geostrophic balance of this transport requires a bank of warm water on its left (southern) side. Such a balance would result in the observed suppression of upwelling along the western coast of Australia. Model results confirm this theory with a downward bending of isotherms toward the coast (Figure 3.28), weak (4 cm s^{-1}) on-shore flow in the upper layers (Figure 3.29), and weak (2 cm s^{-1}) southward flow along the coast (Figure 3.30) at 30°S . This warm southward flow along the western coast of Australia is also relatively fresh, suggesting that the seasonal Leeuwin Current dominates the flow on an annual mean basis (Figure 3.31). Beneath this southward flow, at 300 m depth in Figure 3.30, we can also see the beginnings of a northward flowing undercurrent. The "busyness" in the northeast corner of the volume transport plot (Figure 3.27) is computational noise.

The equatorial Pacific is perhaps the best region of all for validating the world ocean model circulations. The complicated system of eastward- and westward- flowing currents, which have been well observed, were well simulated by the world ocean model of Semtner and Chervin. A cut of the entire Pacific Ocean along the international dateline reveals midlatitude frontal regions between near-surface equatorial and subarctic waters, as well as the bending upward of isotherms near the equator in association with Ekman

divergence (Figure 3.32). A potential temperature contour plot along the equatorial plane reveals a very prominent upward sloping of the 14°C and warmer isotherms from the Western Pacific to the Eastern Pacific (Figure 3.33). This feature supports observations of a deep thermocline in the Western Pacific and a shallow thermocline in the Eastern Pacific during non- El Niño years. Concerning the zonal velocity field, a meridional enlargement of the equatorial region at the dateline (Figure 3.34) reveals, from south to north:

- A very weak eastward-flowing South Equatorial Countercurrent at the surface at $9 - 11^{\circ}\text{S}$.
- A strong (36 cm s^{-1}) westward-flowing South Equatorial Current from 8°S to 4°N and extending to almost 300 m depth near 5°S .
- A very strong (54 cm s^{-1}) eastward-flowing Equatorial Undercurrent (EUC) with a core at about 160 m depth under the equator.
- A moderate eastward-flowing North Equatorial Countercurrent from $4 - 9^{\circ}\text{N}$ and extending to perhaps 200 m depth.
- A weak westward-flowing North Equatorial Current from $9 - 17^{\circ}\text{N}$ and extending to 300 m depth.

A u velocity contour plot along the equatorial plane also reveals that the EUC tilts upward to the east and reaches a maximum eastward speed of 94 cm s^{-1} at about 115 m depth and a longitude of 143°W (Figure 3.35). All of the model-produced current speeds for the equatorial Pacific region are certainly reasonable given annual mean forcing.

The Levitus (1982) data are based upon averages on one-degree squares of all available hydrographic data, where obviously erroneous data have been removed. The final data set is a smoothed analysis of these one-degree square averages. While filling in holes in the original data and generally increasing the reliability of the data

set, this smoothing process also causes a loss of information-- particularly near boundaries, where gradients in water mass properties are most pronounced. The effective horizontal resolution of the Levitus (1982) data set thus turns out to be about three degrees in latitude and longitude (Sarmiento and Bryan, 1982). Even with this smoothing, however, it has been shown that the world ocean model faithfully simulated most of the significant features of world ocean circulation. A global overview of potential temperature difference (D-T) between world ocean model results and annual mean Levitus data shows significant differences in potential temperature along the western boundary currents (Figure 3.36). Thus, the world ocean model may be considered truly robust in that its solution is resistant to minor inconsistencies in the input data (Sarmiento and Bryan, 1982).

World ocean model results for the meridional transport of heat are presented in Figures 3.37, 3.39, and 3.40 for the global, Indian-Pacific, and Atlantic ocean basins, respectively. Curve D represents the total meridional heat transport; curves A, B, and C represent the overturning, gyre, and diffusive components, respectively.

For the global ocean basin (Figure 3.37), we at once notice that the total heat transport is poleward in each hemisphere. This pattern appears to be well supported by the results of other studies (Table 2), although there is quite a bit of variation in the total heat transport magnitudes. In this table, results from studies employing four different methods are compared. The indirect method of Hastenrath (1982) and Hsiung (1985) uses surface oceanic heat fluxes based on many years of ship observations. By assuming no net oceanic

heat storage over an annual cycle, the net annual oceanic heat transport is computed. Miller et al. (1983) use essentially the same method but instead derive the surface heat flux data from an atmospheric general circulation model. The indirect method tends to suffer from systematic errors in the surface heat flux balance calculations, which are particularly troublesome in the tropics where heat flux into/out of the ocean is but a small difference between net radiative heating and cooling by evaporation (Bryan, 1982). The residual method uses satellite measurements of net radiation at the top of the planet earth and subtracts climatological atmospheric heat transport to compute oceanic heat transport as a residual. The major source of error for this method is believed to be systematic biases in the satellite data of about 5 W m^{-2} (Bryan, 1982). The direct method uses hydrographic data across an east-west vertical section to estimate heat transport across a given latitude. Unfortunately, in situ measurements are costly and have thus far provided only limited heat transport information for single, synoptic sections at a few latitudes (Bryan, 1982). Finally, the numerical method uses numerical methods to model ocean circulation and then diagnostically determine heat transports. Until recently, however, computer resource limitations have permitted only coarse-grid model calculations such as those of Bryan and Lewis (1979) (approximately 2.5° horizontal resolution) and Meehl et al. (1982) (5.0° horizontal resolution). The world ocean model of Semtner and Chervin has facilitated the first fine-grid numerical computation of meridional heat transports on a global ocean basis.

An examination of the individual components of the total meridional heat transport for the global ocean is revealing. In Figure 3.37 we can see that the overturning component (curve A) follows the Ekman transport in the tropics and in the southern midlatitudes. It can also be seen that the total meridional heat transport is dominated by the overturning component at low latitudes. The gyre component (curve B) is associated with horizontal gyres and becomes most significant to the total meridional heat transport in the middle latitudes, where east-west temperature differences are great. The diffusive component (curve C) becomes significant to the total meridional heat transport also in the midlatitudes, where large north-south temperature gradients develop between equatorial and subarctic/subantarctic waters. These results are generally consistent with those resulting from the January-July average experiment of Bryan and Lewis (1979) and from the decreased horizontal heat diffusion experiment of Meehl *et al.* (1982) (Figure 3.38).

For the Indian-Pacific ocean basin (Figure 3.39), we again notice that the total heat transport is poleward in each hemisphere. This pattern also appears to be well supported by the results of other studies employing indirect and numerical methods (Table 3), although there is quite a bit of variation in the total heat transport magnitudes. In this table, the reader is advised that the study of Bryan (1982) uses the world ocean model of Bryan and Lewis (1979) to compute basin heat transports. In Figure 3.39, the individual components of the total heat transport north of 30°S appear to contribute to the total heat transport with about the same latitudinal

weighting as in the global ocean case. Within the Indian-Pacific ocean basin, Talley (1984) has estimated a heat transport into the Indian Ocean of 10×10^{14} W to 60×10^{14} W associated with the volume transport estimate of Godfrey and Golding (1981) for flow through the Indonesian Archipelago.

For the Atlantic ocean basin (Figure 3.40), the glaring result of the world ocean model integration is the anomalous northward total heat transport in the Southern Hemisphere. As can be seen in Table 4, however, this anomaly is well supported by the results of many other studies employing indirect, direct, and numerical methods. In this table, the results of Bryan (1982) are again computed using the world ocean model of Bryan and Lewis (1979). The reason for the anomalous northward heat transport observed and calculated in the Southern Hemisphere is unknown. Gordon (1985) calculated a net northwestward geostrophic transport (relative to 1500 dbar) of 14 Sv from the Indian Ocean into the South Atlantic Ocean that he associates with partial steering of the Agulhas Current by anticyclonic eddies spawned at the Agulhas Retroflexion. He further computes a resultant northward heat transport in the South Atlantic of 0.23×10^{14} W to 4.7×10^{14} W, depending on whether the Atlantic return water is relatively warm South Atlantic thermocline water or relatively cold North Atlantic Deep Water (or some mixture thereof). Gordon (1985) goes on to state that an interocean exchange around the southern tip of South America is unlikely to contribute significantly to a northward heat transport in the South Atlantic, because the eastward flow through the Drake Passage is nearly as cold as North Atlantic

Deep Water (NADW) and would thus require a very large production rate of NADW. Olson and Evans (1985), on the other hand, believe that the anticyclonic Agulhas Retroflection eddies themselves may contribute significantly to the northward heat transport of the South Atlantic, as the encircled warm waters of the Indian Ocean thermocline propagate to the northwest with their captor eddies. Finally, Bryan (1986) has demonstrated in a process study that, with symmetric forcing and a symmetric basin, a positive surface layer salinity anomaly introduced in the Northern Hemisphere polar region will induce cross-equatorial thermohaline circulations that will cause an equatorward transport of heat over much of the Southern Hemisphere. Based upon Bryan's result, no interocean exchange of heat is required to explain an anomalous northward heat transport in the Southern Hemisphere.

World ocean model results for the meridional volume transport of water are presented in Figures 3.41, 3.43, and 3.44 for the global, Indian-Pacific, and Atlantic ocean basins, respectively. In Figure 3.41, we first note that meridional gyres are set up in the upper 200-300 m of the global water column by near-surface Ekman transports. In the vicinity of the ACC, however, the wind-driven cell is modeled to penetrate down to the base of the thermocline. The larger equatorward transport near the surface in this Southern Hemisphere gyre results at least in part from stronger westerly winds and from a greater ratio of ocean to land than in the Northern Hemisphere (Bryan and Lewis, 1979). Another meridional gyre set up in mid-depths supports a cross-equatorward circulation that brings cold NADW southward from the far north and warmer thermocline waters northward from the Southern

Hemisphere tropics. Examination of Figures 3.43 and 3.44 confirms that this meridional circulation is mainly driven by water mass movements in the Atlantic vice Indian-Pacific ocean basin. A final meridional gyre appears near the bottom in the Southern Hemisphere of the global ocean basin. Though generally associated with the northward flow of Antarctic Bottom Water in the Atlantic ocean basin, examination of Figures 3.43 and 3.44 suggests instead the northward flow of Common Water in the Indian-Pacific ocean basin. In the Atlantic, Antarctic Bottom Water (AABW) formed in the Weddell Sea is generally believed to flow northward in the western deep basin formed by the Mid-Atlantic Ridge and the continental slope of South America. The eastern deep basin formed by the Mid-Atlantic Ridge and the continental slope of Africa provides a channel for a compensating southward flow of NADW and modified AABW. Zonal cross-sections of modeled potential temperature and salinity at 16°S in the Atlantic Ocean support this view by showing excellent agreement with similar observed sections (as expected in the deep ocean, where a one year robust-diagnostic time constant easily overdrives much slower physical processes) (Figures 3.45 and 3.46). As a consequence, a zonal summation of volume transport across the South Atlantic reveals only a very weak near-bottom meridional gyre, as the southward flow in the eastern deep basin effectively cancels out most of the northward flow in the western deep basin. Moreover, a streamline plot of the Gulf Stream region at 5000 m depth (Figure 3.47) supports the flow of AABW north of the equator, and this feature is certainly not reflected in the near-bottom gyre of the global ocean basin. Thus, the near-bottom

gyre of the global ocean basin is linked with meridional circulations in the Indian-Pacific ocean basin. Common Water represents a mixture of transformed AABW and NADW as they are advected into the Indian and Pacific Oceans by the ACC, as well as less dense AABW formed in the Ross Sea and perhaps also along the Amery Ice Shelf (Pickard and Emery, 1982). This very large water mass spreads northward along the bottom in the Indian and Pacific ocean basins, thus driving a very large meridional cell confined to the Southern Hemisphere.

For the purpose of comparison, world ocean meridional circulation results from other studies are provided in Figure 3.42. Figure 3.42(a) is a schematic view of the observed meridional circulation according to Gordon (1971). His values represent yearly averages calculated from salt budget considerations and from estimates of the transport of NADW. Perhaps the best comparison to make with Gordon's results concerns the cross-equatorial transport of NADW, where Gordon's value of 15 Sv compares well with the world ocean model's value of up to 12.5 Sv. Figure 3.42(b) is a contour plot of the global meridional circulation according to the numerical model results of Cox (1975). This figure resulted from 2.3 years of integration of a prognostic model initialized with observed data and using two degrees horizontal resolution and annual mean forcing. A steady-state condition was not reached. We see from this figure that Cox also computes a cross-equatorial transport of NADW of more than 10 Sv. His model also produces a near-bottom gyre in the Southern Hemisphere -- in agreement with the world ocean model's simulation. With respect to the near-surface wind-driven cells, Cox's model

produces results that are very similar to those of the world ocean model, including a Southern Hemisphere midlatitude gyre that extends to the base of the thermocline. Figure 3.42(c) is a contour plot of the global meridional circulation according to the numerical model results of Bryan and Lewis (1979). This figure is an average of the seasonal results from January and July, and is derived from 50 years of integration using a robust-diagnostic strategy. Horizontal resolution is 2.4° in latitude and 2.8° in longitude. While the near-surface wind-driven cells of Bryan and Lewis match up well with those of the world ocean model, the cross-equatorial gyre circulation does not. The world ocean model depicts the southward flow of NADW being balanced by a northward flow of thermocline waters from the Southern Hemisphere tropics, whereas the model of Bryan and Lewis suggests that AABW crossing the equator will provide the balancing flow. Perhaps Bryan and Lewis are revealing a seasonal effect not distinguishable when using annual mean forcing. The increased latitudinal domain of Bryan and Lewis also allows polar meridional cells to develop which accommodate the formation of NADW and AABW.

2. Isopycnal Mixing Integration

According to Semtner (1984), eddy diffusion in the real ocean may act more along isopycnal surfaces than purely in the horizontal. In ocean areas of significant baroclinicity, the effect of horizontal Laplacian diffusion is to flatten out isopycnals and thus to reduce the baroclinicity. By contrast, isopycnal diffusion will preserve the baroclinicities. Thus we might expect that a switch from Laplacian to isopycnal mixing would result in enhanced boundary currents--

particularly in coarse-grid calculations. This trend was in fact observed in the one degree, twenty level world ocean model. The Gulf Stream increased in strength from 74 cm s^{-1} to 86 cm s^{-1} and from 67 Sv to 76 Sv off Cape Hatteras. The Kuroshio Current increased in strength from 87 cm s^{-1} to 133 cm s^{-1} and from 91 Sv to 101 Sv south of Japan. The Agulhas Current increased dramatically in strength from 84 Sv to 125 Sv and from a maximum v velocity of 66 cm s^{-1} to over 95 cm s^{-1} . Westward flow around the southern tip of Africa has also increased in magnitude as a consequence. The Somali Current increased only slightly in speed as a result of isopycnal mixing. The EAC increased in speed from 40 cm s^{-1} to 56 cm s^{-1} along the Australian coast, resulting in a more southward penetration of the EAC (46°S versus 40°S) before completing its anticyclonic turn to the northeast. Greater current speeds were also apparent along the Tasman Front and to the northeast of New Zealand. West of Australia, the effect of isopycnal versus Laplacian mixing is dramatically illustrated by comparing zonal sections of potential temperature and v velocity at 30°S (Figures 3.48 and 3.49). In the isopycnal mixing case, the isotherms are observed to bend much more sharply downward at the coast, supporting a southward flow at the surface of 7 cm s^{-1} (versus 2 cm s^{-1} in the Laplacian mixing case).

Meridional heat transport and meridional volume transport results for the world ocean model using isopycnal mixing were very close to those of the baseline (Laplacian mixing) integration. The only noteworthy difference is that there appears to be a trend toward even greater northward heat transports in the South Atlantic Ocean.

It is interesting to note that this trend occurs simultaneously with a trend toward increased westward flow around the southern tip of Africa. Heat transport results for the isopycnal mixing integration are summarized in Tables 2, 3, and 4, for the global, Indian-Pacific, and Atlantic ocean basins, respectively. Plots of meridional heat transport and meridional volume transport for all basins are contained in the Appendix.

B. ONE-HALF DEGREE, TWENTY LEVEL EXPERIMENTS

1. Baseline (Three Year Interior Restoring) Integration

There were several noteworthy changes in the world ocean model integration results stemming from increased horizontal resolution and reduced climatological damping in the ocean interior. First, an examination of Figure 3.50 reveals a more clearly defined Gulf Stream north wall when compared to the one degree baseline integration. Also evident is the emergence of a frontal zone extending southeastward from Newfoundland over the Grand Banks. However, reduced climatological damping in the ocean interior permitted the flow field of the Gulf Stream to degrade even further -- once again suggesting that mass exchange with the Arctic Ocean may be needed for a proper simulation. The maximum volume transport off Cape Hatteras is now only 53 Sv (versus 67 Sv) (Figure 3.51). Note also from this figure that the computational noise in the southwestern Sargasso Sea that was present in the one degree baseline integration has been eliminated in the one-half degree integration.

In the Kuroshio Current region, the reduced eddy viscosity and increased interior restoring time constant resulted in a stronger

Kuroshio Current and a stronger Kuroshio Extension. In particular, the maximum speed of the Kuroshio Current south of Japan increased from 87 cm s^{-1} to in excess of 114 cm s^{-1} . Greater volume transports were also computed further to the east than in the one degree baseline integration (Figure 3.52). Notice also in Figure 3.52 the emergence of subtropical flow instabilities that were not present in the one degree baseline integration. The ACC in the vicinity of the Drake Passage maintained about the same net volume transport, although current speeds were somewhat increased in localized areas. Much of the computational noise present in the vicinity of the Drake Passage for the one degree baseline integration has also been eliminated (Figure 3.53). One dramatic result of increased resolution, however, was the strengthening and increased definition of a near-surface front where the Falkland and Brazil Currents meet (Figure 3.54). In the EAC region, somewhat greater current speeds were computed along the Australian coast (64 versus 40 cm s^{-1}), but the volume transport of the EAC was about the same. Current speeds were also slightly increased along the Tasman Front. In this experiment the EAC is depicted as extending southward only to 36°S (versus 40°S), and computational noise is no longer evident (Figure 3.55). Subtropical instabilities have also emerged in the potential temperature field (Figure 3.56).

The near-surface potential temperature field in the region of the Agulhas Current is interesting in a couple of respects: the frontal region between the Agulhas Return Current and the ACC has sharpened considerably, and the South Equatorial Current in the Indian

Ocean is now simulated as meandering considerably as it approaches the African coast (Figure 3.57). This latter result is also evident in the volume transport field (Figure 3.58). Other results in this region include a stronger Agulhas Current (94 Sv versus 84 Sv) and a Somali Current that has increased in speed from 121 cm s^{-1} to in excess of 155 cm s^{-1} .

West of Australia, we first note that the computational noise that appeared in the northeast corner of the volume stream function plot for the one degree baseline integration has been eliminated by the shift to one-half degree horizontal resolution (Figure 3.59). The transport between Indonesia and Australia has remained at about 20 Sv -- consistent with the estimates of Godfrey and Golding (1981). Along the west coast of Australia, southward flow at the surface has increased slightly from 2 cm s^{-1} to 3 cm s^{-1} . In the equatorial Pacific region, the only significant change over the one degree baseline integration is a stronger EUC, reaching a maximum eastward speed of 114 cm s^{-1} (versus 94 cm s^{-1}) at about 138°W (versus 143°W) longitude and 115 m depth. Again, stronger currents in this integration can generally be attributed to decreased eddy viscosity.

The meridional heat transport results of the one degree baseline integration were fine-tuned in the one-half degree baseline integration. These results are summarized in Tables 2, 3, and 4 for the global, Indian-Pacific, and Atlantic ocean basins, respectively. The actual curves from which these values were derived are contained in the Appendix. For the global ocean, we note less of a northward total heat transport north of 20°S . and less of a southward total heat

transport south of 20°S. Several effects accomplish these trends. First, we note in all ocean basins a flattened curve for the diffusive heat transport. This effect can be attributed to decreased eddy diffusivity. Second, the overturning component in the tropics has shifted southward (i.e., toward a more southward or less northward heat transport) for the global and Indian-Pacific ocean basins. This effect probably results from a more prognostic evolution of the waters above the main thermocline. Lastly, we can detect a reduced gyre component in the Northern Hemisphere midlatitudes of the Atlantic Ocean that also reflects in the global ocean results. This effect is erroneous in that a longer interior restoring time constant permitted the Gulf Stream to degrade further from climatology than in the one degree baseline integration. The only noteworthy change in the meridional volume transport contour plots was reduced cross-equatorial volume transport in the Atlantic Ocean. This effect results from the combination of no mass exchange with the Arctic Ocean and a less robust damping of the ocean interior. Volume transport contour plots for each of the ocean basins are contained in the Appendix.

2. Free Thermocline Integration

Sarmiento and Bryan (1982) found that the most realistic results from their robust-diagnostic model occurred when climatological damping was reduced to zero in the top 870 m of the water column. Following their "free thermocline" approach in the top 710 m of the water column, the world ocean model produced results that were generally very similar to those obtained using a three year restoring constant in the ocean interior. All current systems

examined in this study maintained nearly constant speeds and transports. The north wall of the Gulf Stream is somewhat weakened and the frontal region off Newfoundland is considerably altered -- but these results may stem from the lack of mass exchange with the Arctic Ocean, and therefore may be erroneous (Figure 3.60). One noteworthy result of the free thermocline experiment was the general warming of the upper several hundred meters of the water column. This trend can be observed by close examination (at 30°N latitude, for example) of a meridional cross-section of potential temperature along the international dateline (Figure 3.61). The free thermocline integration also brought increased definition to a cool and fresh countercurrent/undercurrent flowing northward beneath and offshore from the Leeuwin Current (Figures 3.62, 3.63, and 3.64). Lastly, the free thermocline experiment brought increased amplitude to subtropical instabilities that initially emerged in the one-half degree baseline integration (Figures 3.65 and 3.66). The meanders of the South Equatorial Current as it approaches the African coast in the Indian Ocean are now associated with greater zonal velocities than in the one-half degree baseline integration (Figure 3.67). Meridional heat transport and volume transport plots for the free thermocline experiment are contained in the Appendix. Meridional heat transport results for this integration are also summarized in Tables 2, 3, and 4 for the global, Indian-Pacific, and Atlantic ocean basins, respectively. Heat transport results were very consistent with those of the one-half degree baseline integration. Northward heat transport in the northern tropics and southward heat transport in the southern

tropics of the global ocean basin were somewhat reduced, owing largely to a reduced magnitude of the overturning component in the Indian-Pacific ocean basin. This trend is consistent with that observed when the damping time constant in the ocean interior was increased from one year to three years. Similarly, the erroneous trend toward reduced cross-equatorial transport in the Atlantic Ocean was continued in the free thermocline integration.

TABLE 2: GLOBAL MERIDIONAL HEAT TRANSPORT COMPARISON

STUDY	METHOD	HEAT TRANSPORT ($\times 10^{14}\text{W}$) AT													
		60°N	50°N	40°N	30°N	20°N	10°N	0°	10°S	20°S	30°S	40°S	50°S	60°S	
Hastenrath (1982)	Indirect	2.5	8.0	17.5	22.5	20.0	13.0	1.0	-15.0	-20.0	-17.5	-12.0	-9.0	-6.5	
Miller et al. (1983)	Indirect	5.0	8.0	10.0	21.0	27.0	25.0	8.0	-7.0	-16.0	-11.0	-4.0	-1.0	-1.0	
Hsung (1985)	Indirect	2.4	4.3	6.5	15.0	16.3	12.4	0.7	-16.8	-19.5	-16.2	-9.6	-	-	
Oort and Vonder Haar (1976)	Residual	-2.0	10.0	18.0	20.0	29.0	11.0	-7.0	-	-	-	-	-	-	
Trenberth (1979)	Residual	-	-	-	-	-	-	0.0	-17.0	-25.0	-27.0	-18.0	-11.0	-10.0	
Bryden (1979)	Direct	-	-	-	-	-	-	-	-	-	-	-	-	-5.5	
Bryan and Lewis (1979)	Numerical	2.0	4.0	7.5	9.5	9.0	7.0	0.0	-6.0	-7.0	-5.5	-7.5	-7.5	-3.0	
Meehl et al. (1982)	Numerical	5.0	10.0	14.0	16.0	17.5	16.0	-8.0	-24.0	-18.0	-17.0	-18.5	-20.0	-22.5	
1° Baseline	Numerical	2.9	6.8	9.3	9.7	14.5	18.5	9.0	-7.2	-7.1	-4.4	-8.6	-16.3	-8.3	
1° Isopycnal Mixing	Numerical	2.9	6.5	10.3	10.9	15.0	19.1	10.2	-6.2	-6.3	-3.9	-11.6	-16.8	-9.5	
1/2° Baseline	Numerical	2.0	4.5	5.5	8.4	13.9	13.0	0.7	-9.8	-7.3	-3.0	-2.8	-9.6	-4.6	
1/2° Free Thermocline	Numerical	2.5	6.2	6.7	8.2	9.9	12.2	5.7	-7.5	-6.6	-3.1	-2.8	-8.9	-5.2	

TABLE 3: INDIAN-PACIFIC MERIDIONAL HEAT TRANSPORT COMPARISON

STUDY	METHOD	HEAT TRANSPORT ($\times 10^{14} \text{W}$) AT										
		60°N	50°N	40°N	30°N	20°N	10°N	0°	10°S	15°S	20°S	30°S
Hastenrath (1982)	Indirect	0.1	1.0	5.5	11.4	9.0	3.0	-7.1	-23.0	-26.7	-27.7	-24.1
Miller et al. (1983)	Indirect	0.5	2.0	2.0	7.0	10.5	11.0	-3.5	-16.5	-21.5	-22.0	-19.0
Hsiung (1985)	Indirect	0.0	-0.2	0.0	5.5	7.2	4.5	-4.7	-19.0	-21.3	-20.9	-16.6
Bryan (1982)	Numerical	0.0	1.5	2.5	3.5	3.0	1.5	-3.0	-9.0	-9.5	-9.0	-8.0
Neel et al. (1982)	Numerical	0.0	0.5	1.0	3.0	6.5	5.5	-8.0	-21.0	-22.0	-22.0	-17.5
1° Baseline	Numerical	0.0	1.0	2.5	4.0	7.5	10.3	1.9	-11.9	-12.6	-11.5	-7.6
1° Isopycnal Mixing	Numerical	0.1	0.9	2.4	4.3	7.4	10.5	2.7	-11.1	-11.6	-11.8	-8.7
1/2° Baseline	Numerical	0.0	0.7	1.0	3.2	7.5	5.7	-5.8	-14.1	-14.0	-11.5	-7.0
1/2° Free Thermocline	Numerical	0.1	1.6	1.5	2.8	4.1	6.2	1.0	-10.6	-11.5	-10.2	-6.9

TABLE 4: ATLANTIC MERIDIONAL HEAT TRANSPORT COMPARISON

STUDY	METHOD	HEAT TRANSPORT ($\times 10^{14}\text{W}$) AT													
		60°N	50°N	40°N	36°N	30°N	25°N	15°N	10°N	0°	10°S	15°S	20°S	25°S	30°S
Hastenrath (1982)	Indirect	2.6	6.5	7.5	8.5	10.7	11.0	11.1	10.8	9.8	8.5	8.5	8.0	7.5	6.9
Miller et al. (1983)	Indirect	5.0	6.5	8.0	11.0	14.0	15.5	15.5	14.5	10.5	8.0	7.0	6.5	7.0	8.0
Hsiong (1985)	Indirect	2.4	4.5	6.3	-	9.5	9.6	8.7	8.0	5.4	2.3	2.0	1.5	0.8	0.4
Bennett (1978)	Direct	-	-	-	-	-	-	-	-	-	-	-	-	5.1 (24°S)	4.2 (32°S)
Wunsch (1980)	Direct	-	-	-	7.5	-	12.0	-	-	-	-	-	-	-	-
Bryden and Hall (1980)	Direct	-	-	-	-	-	11.0	-	-	-	-	-	-	-	-
Roemmich (1980)	Direct	-	-	-	8.0	-	12.0	-	-	-	-	-	-	-	-
Fu (1981, METEOR)	Direct	-	-	-	-	-	-	-	-	-	4.2 (8°S)	8.6 (16°S)	5.4 (21°S)	-	8.3 (28°S)
Fu (1981, IGY)	Direct	-	-	-	-	-	-	-	-	-	1.8 (8°S)	7.3 (16°S)	-	5.4 (24°S)	7.7 (32°S)
Bryan (1982)	Numerical	1.5	3.5	4.5	5.0	5.5	5.5	5.0	5.0	3.5	3.0	2.5	2.0	2.0	2.0
Meehl et al. (1982)	Numerical	-0.5	0.5	3.0	4.8	6.5	7.5	9.5	8.0	5.0	3.5	3.0	3.0	3.5	3.0
1° Baseline	Numerical	2.8	5.7	6.8	6.2	5.6	6.4	7.9	8.2	7.1	4.7	4.6	4.4	3.6	3.2
1° Isopycnal Mixing	Numerical	2.8	5.6	7.9	6.2	6.6	7.1	7.6	8.6	7.5	4.8	5.3	5.5	4.8	4.8
1/2° Baseline	Numerical	2.0	3.8	4.5	4.9	5.1	5.8	7.1	7.3	6.5	4.3	4.3	4.2	4.0	4.1
1/2° Free Thermocline	Numerical	2.4	4.6	5.2	5.4	5.4	5.5	6.0	6.0	4.7	3.0	3.6	3.7	3.7	3.8

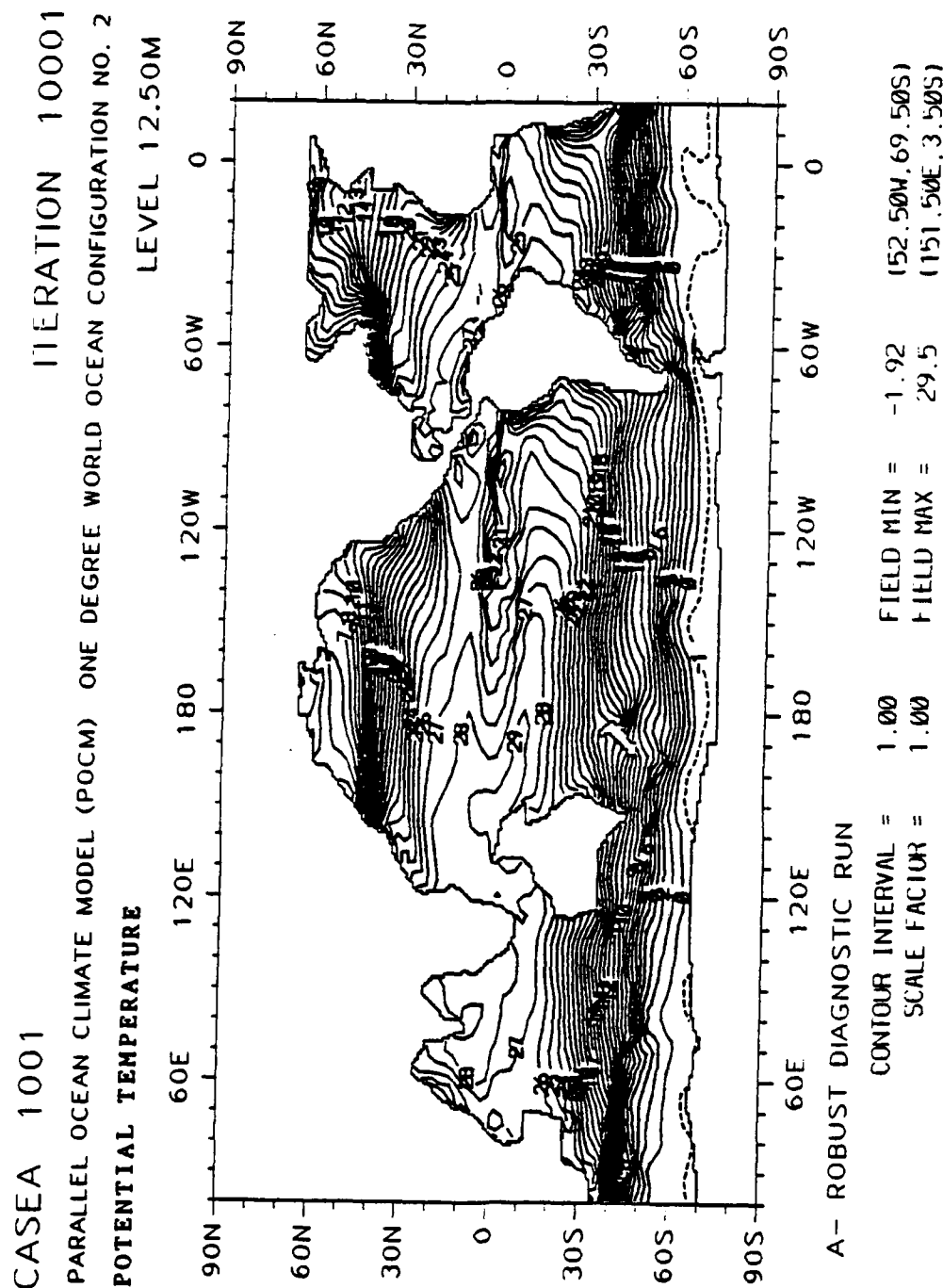


Figure 3.1 Global overview of potential temperature in °C at 12.5 m depth for experiment 1.

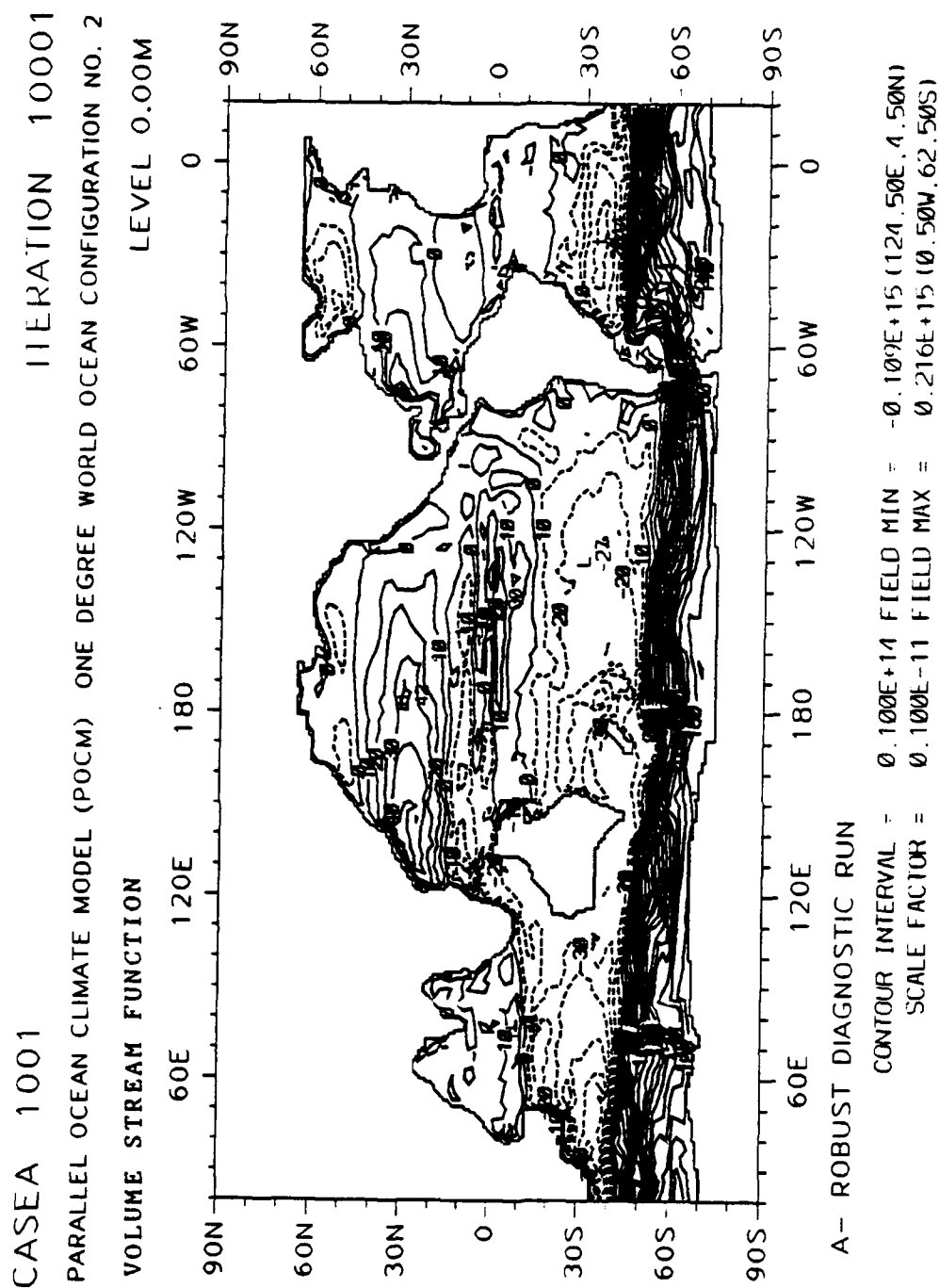
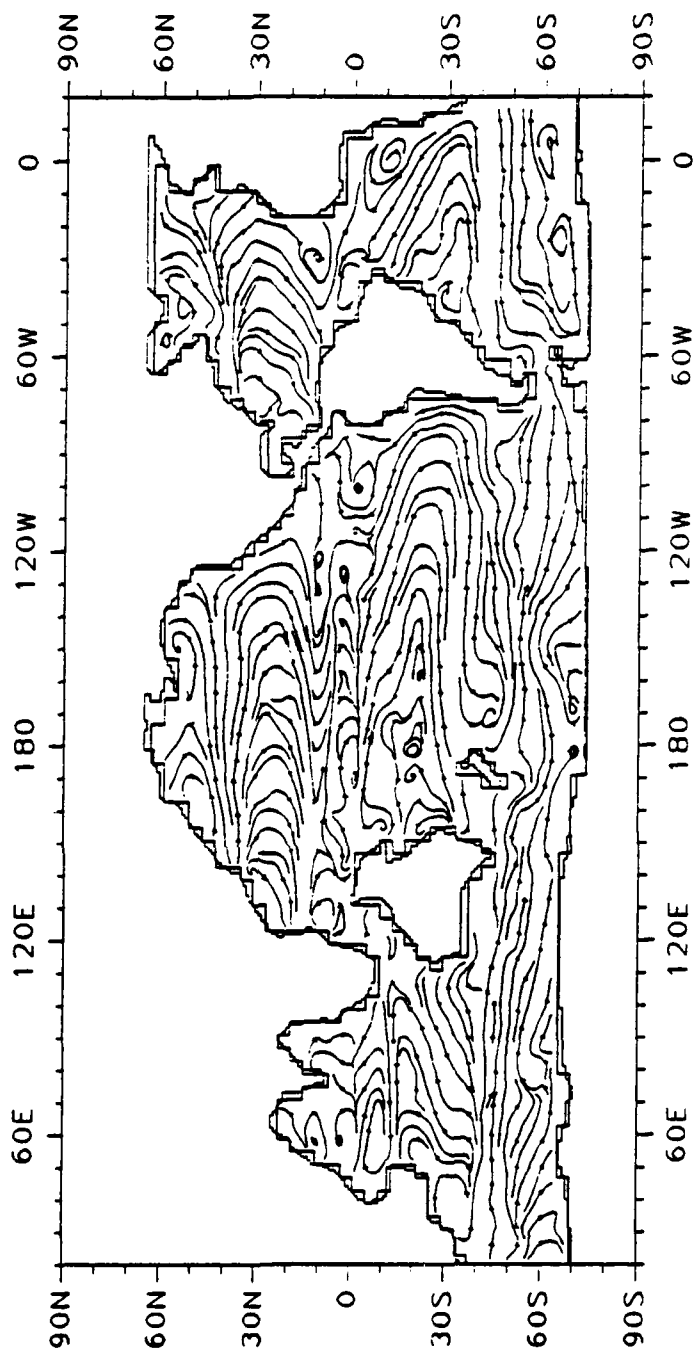


Figure 3.2 Global overview of horizontal volume transport in Sv ($-10^{12} \text{ cm}^3 \text{ s}^{-1}$) for experiment 1.

CASEA 1001
 PARALLEL OCEAN CLIMATE MODEL (POCM) ONE DEGREE WORLD OCEAN CONFIGURATION NO. 2
 STREAMLINES
 LEVEL 62.50M
 ITERATION 10001



A- ROBUST DIAGNOSTIC RUN

Figure 3.3

Global overview of streamline flow at 62.5 m depth for experiment 1. Streamlines are everywhere tangent to the current vectors and are selectively originated/discontinued to maintain near-uniform spacing.

CASEA 1001
 PARALLEL OCEAN CLIMATE MODEL (POCM) ONE DEGREE WORLD OCEAN CONFIGURATION NO. 2
 STREAMLINES
 LEVEL 12.50M
 ITERATION 10001

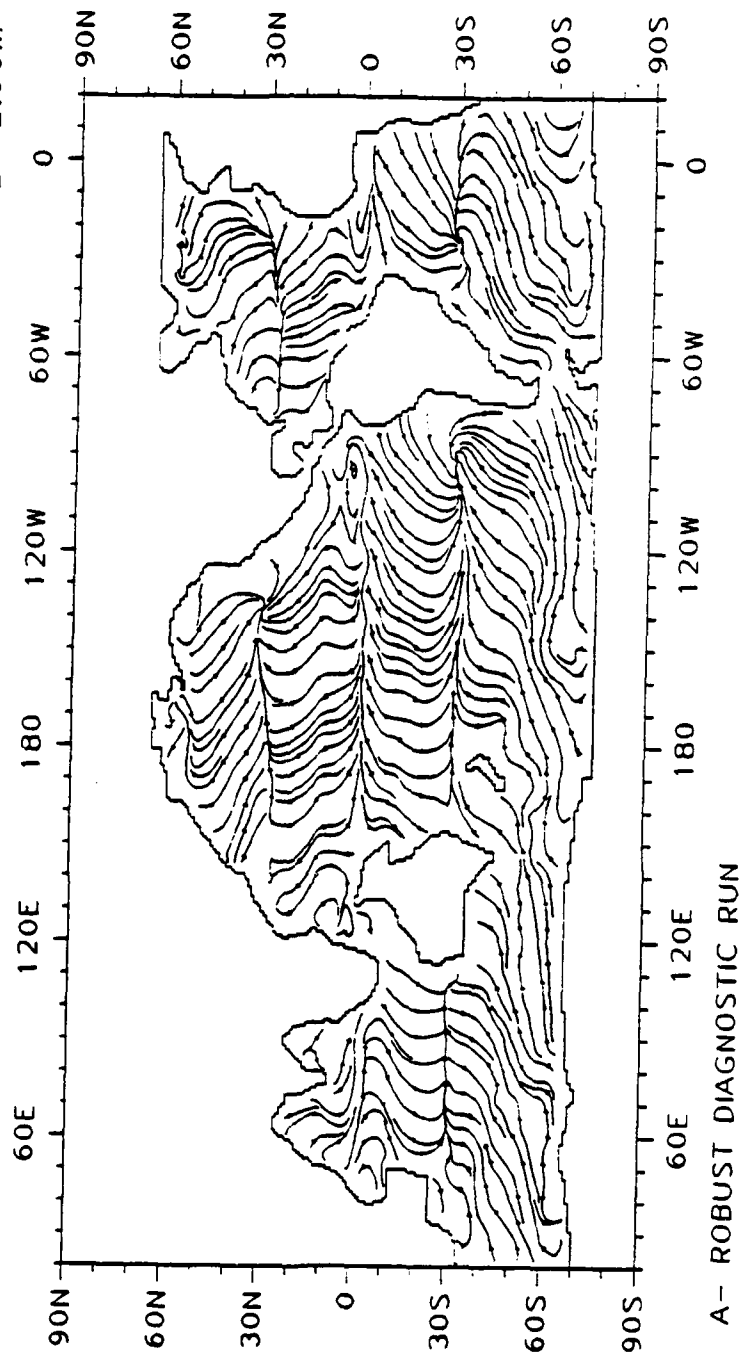


Figure 3.4

Global overview of streamline flow at 12.5 m depth for experiment 1. Streamlines are everywhere tangent to the current vectors and are selectively originated/discontinued to maintain near-uniform spacing.

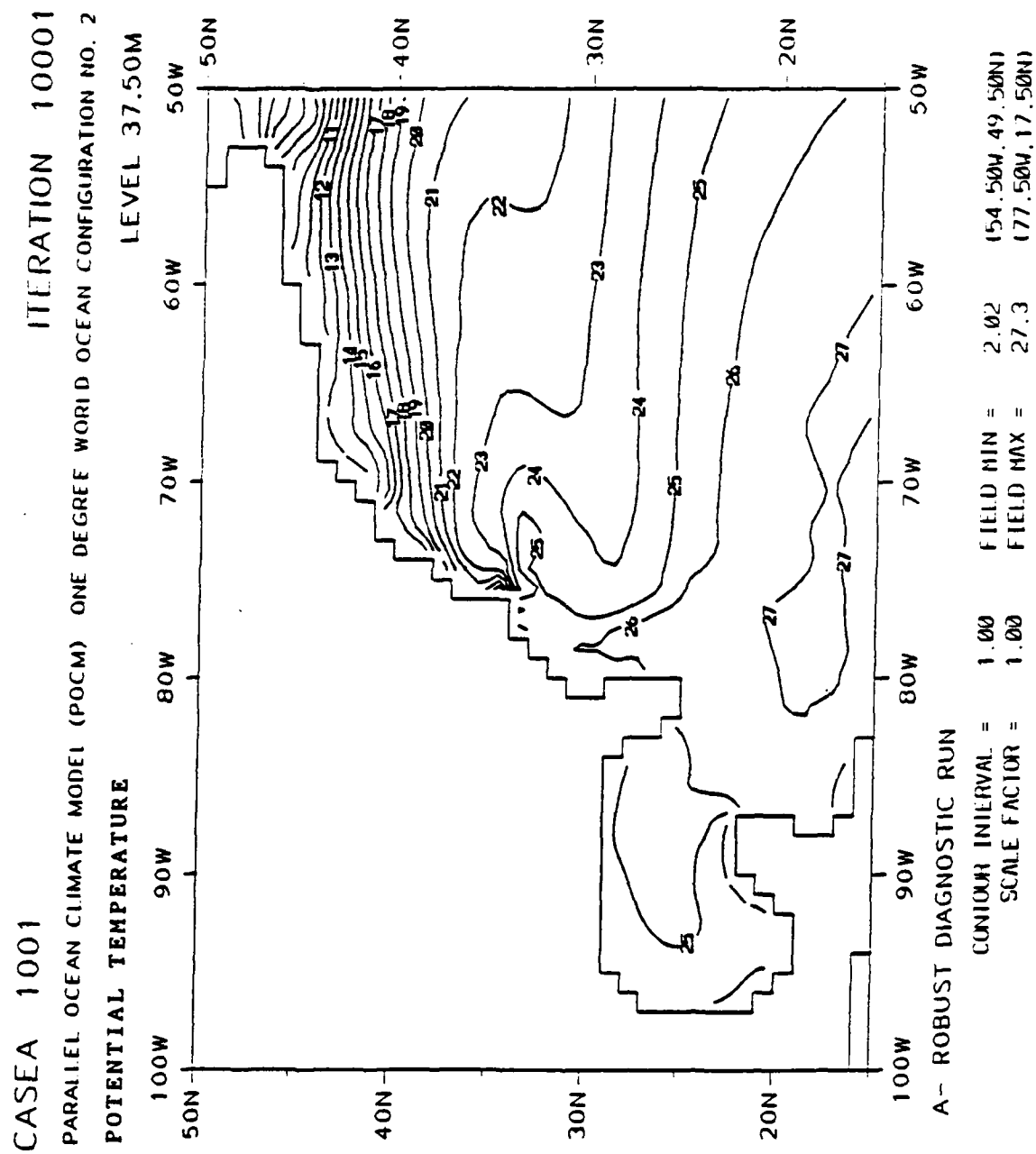


Figure 3.5 Potential temperature in °C at 37.5 m depth in the Gulf Stream region for experiment 1.

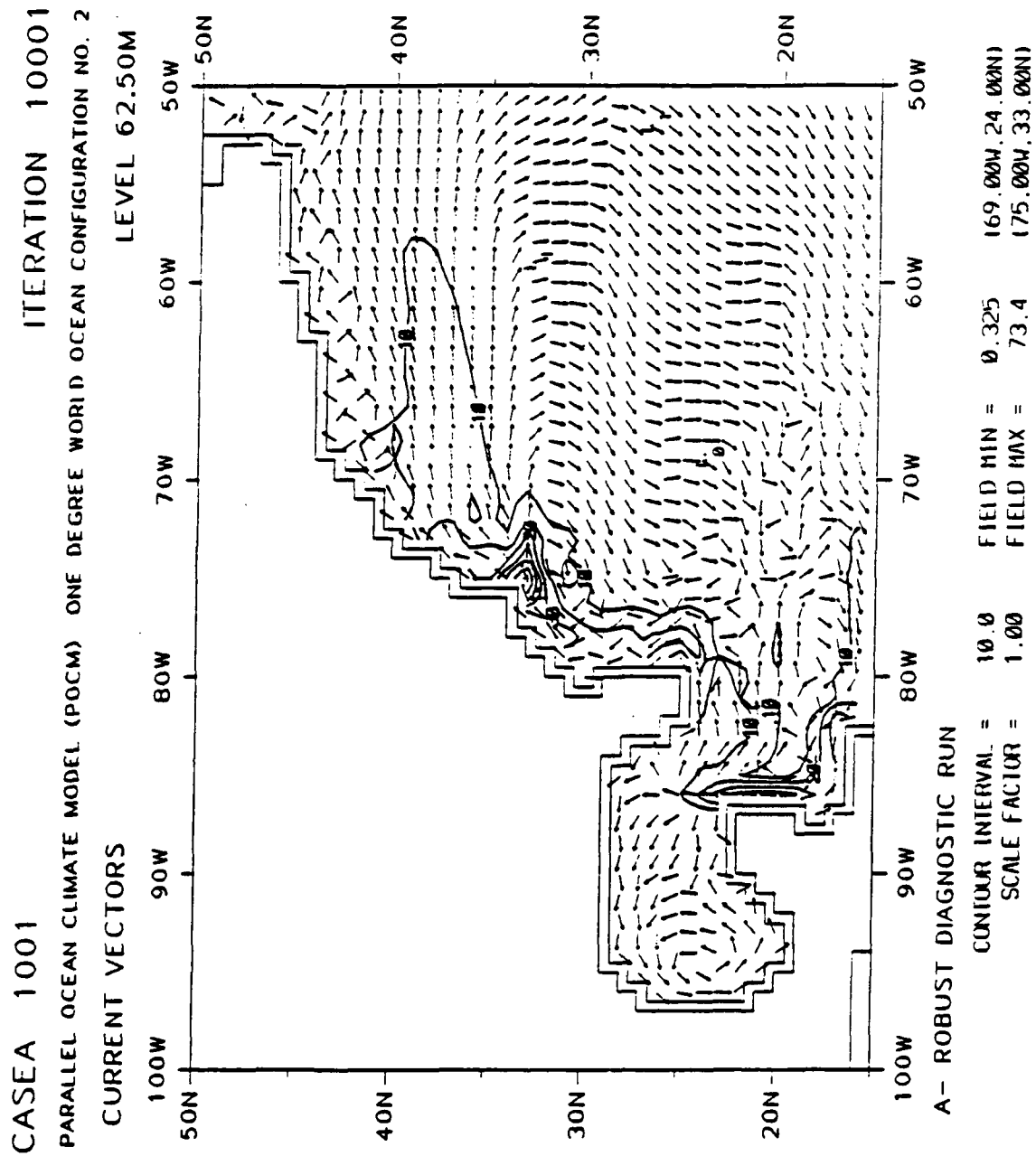
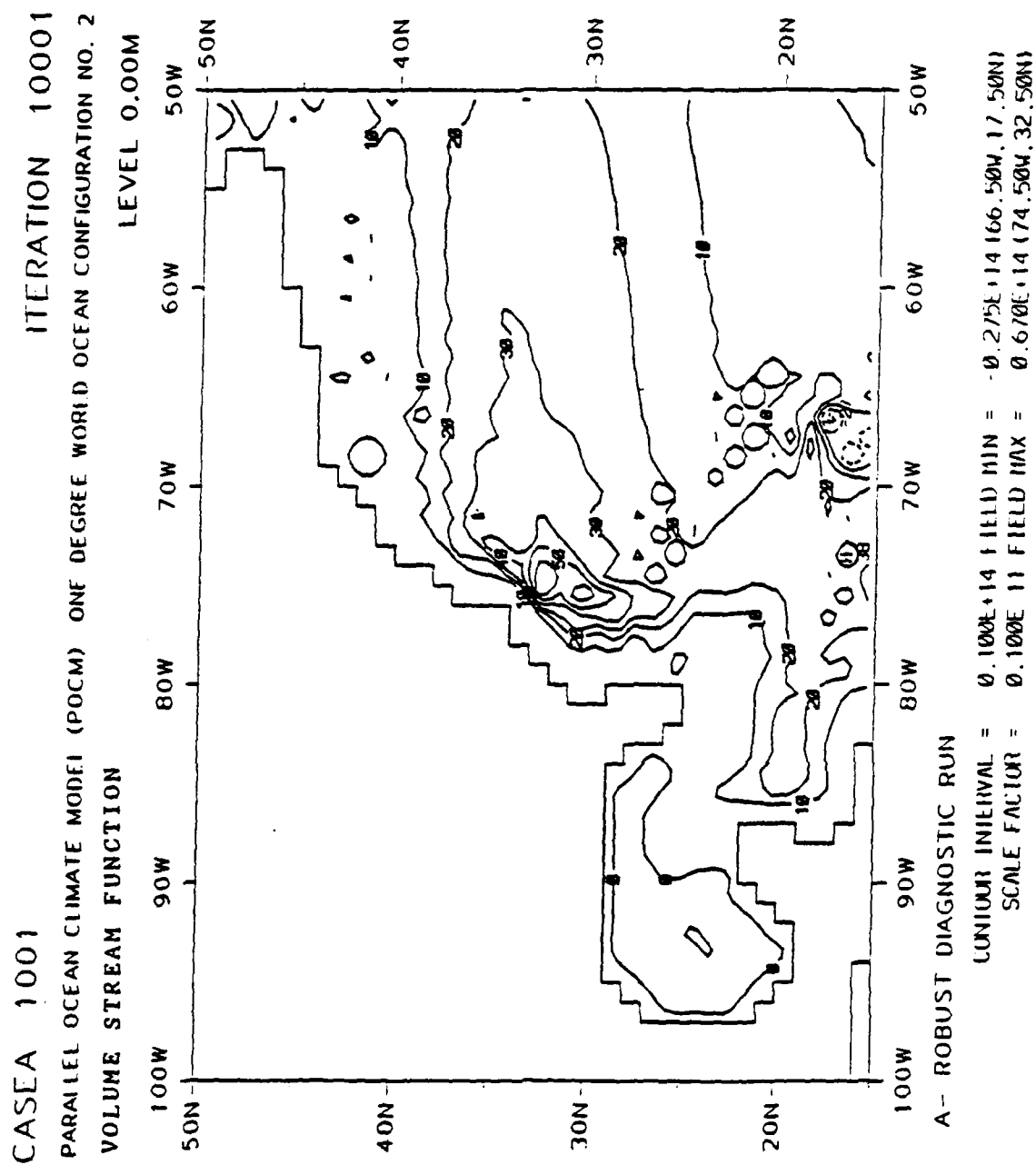


Figure 3.6 Fixed-length current vectors (with superimposed speed contours in cm s^{-1}) at 62.5 m depth in the Gulf Stream region for experiment 1.



CASEA 1001
 PARALLEL OCEAN CLIMATE MODEL (POCM) ONE DEGREE WORLD OCEAN CONFIGURATION NO. 2
 STREAMLINES
 LEVEL 37.50M
 ITERATION 10001

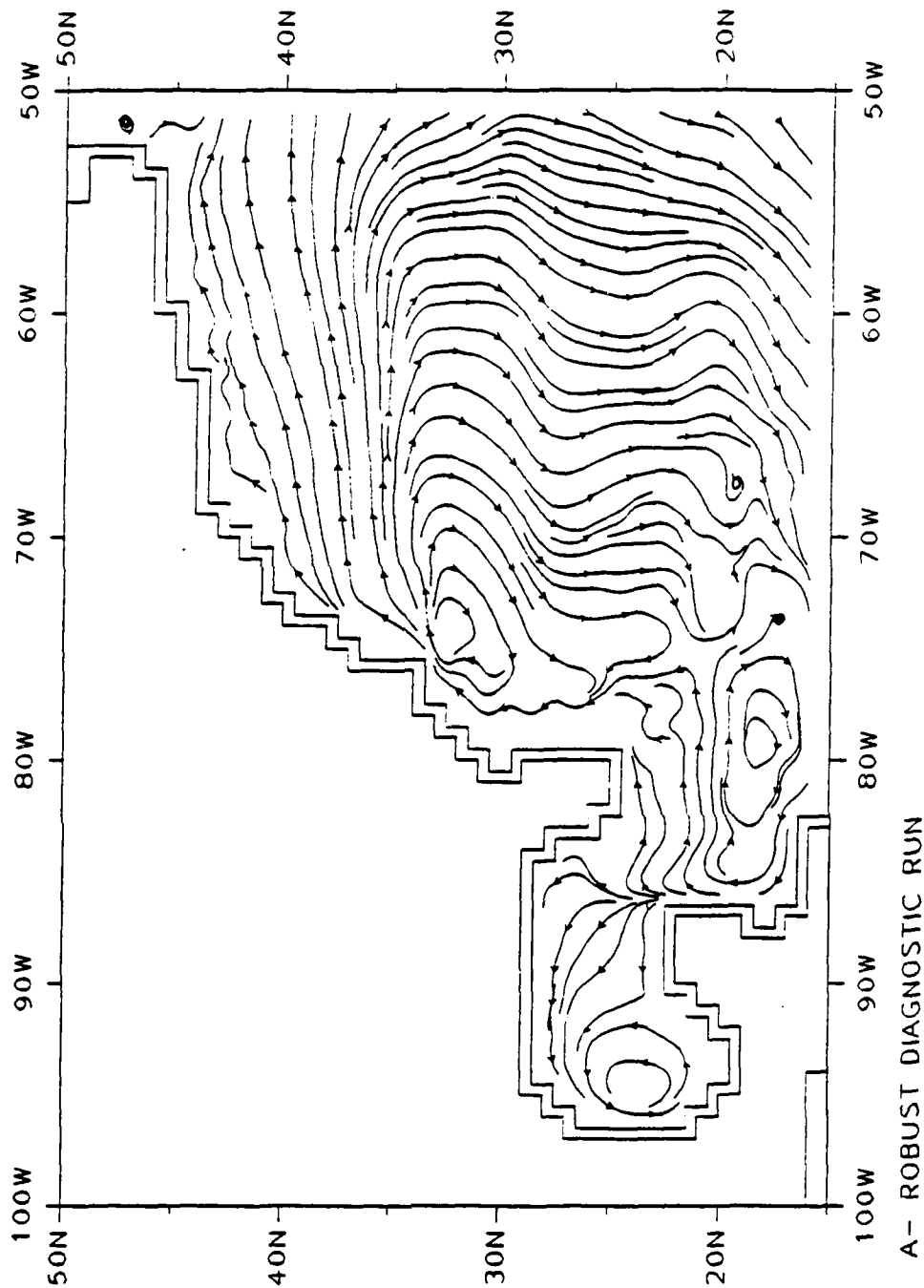


Figure 3.8

Streamlines at 37.5 m depth in the Gulf Stream region for experiment 1. Streamlines are everywhere tangent to the current vectors and are selectively originated/discontinued to maintain near-uniform spacing.

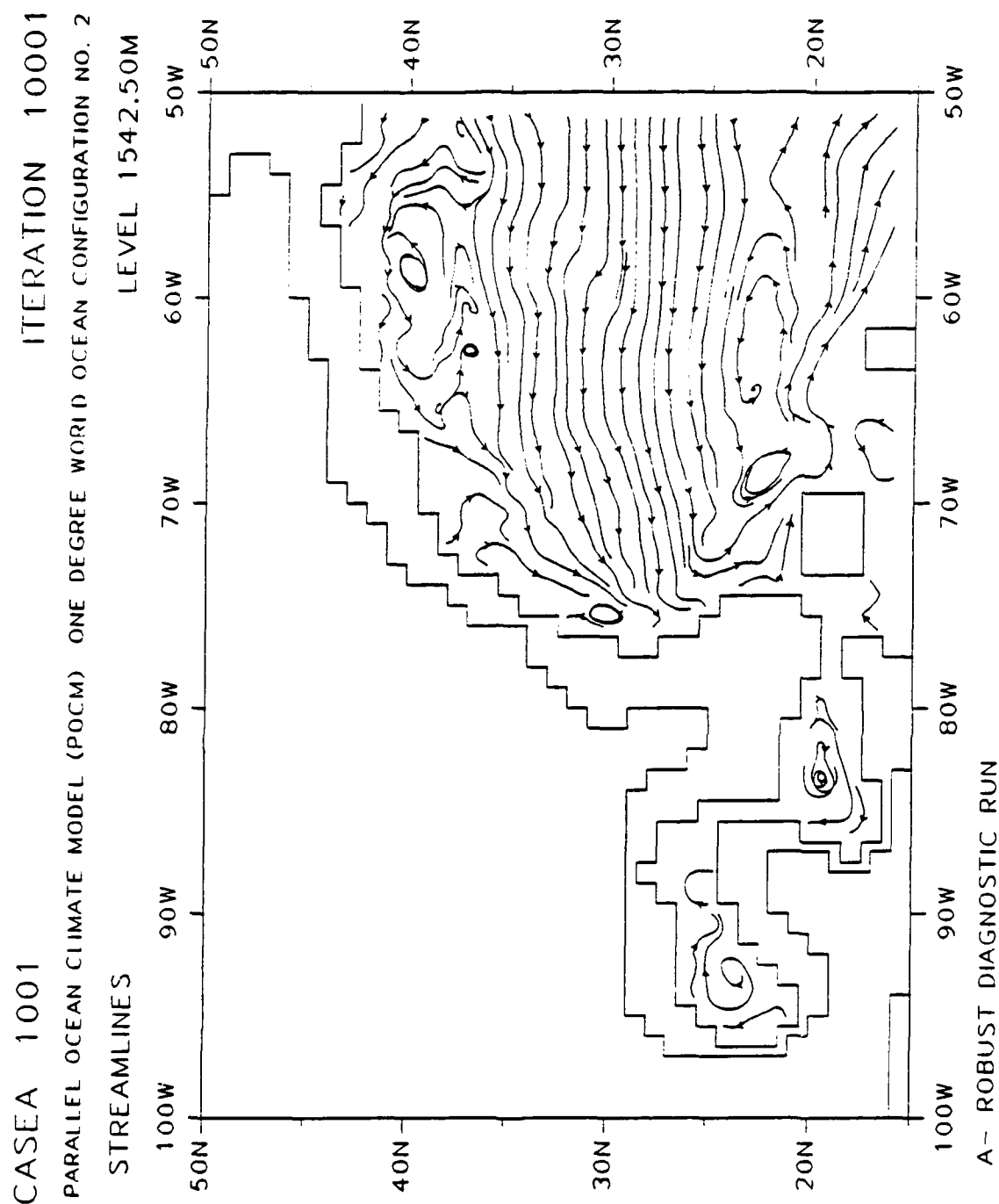


Figure 3.9

Streamlines at 1542.5 m depth in the Gulf Stream region for experiment 1. Streamlines are everywhere tangent to the current vectors and are selectively originated/discontinued to maintain near-uniform spacing.

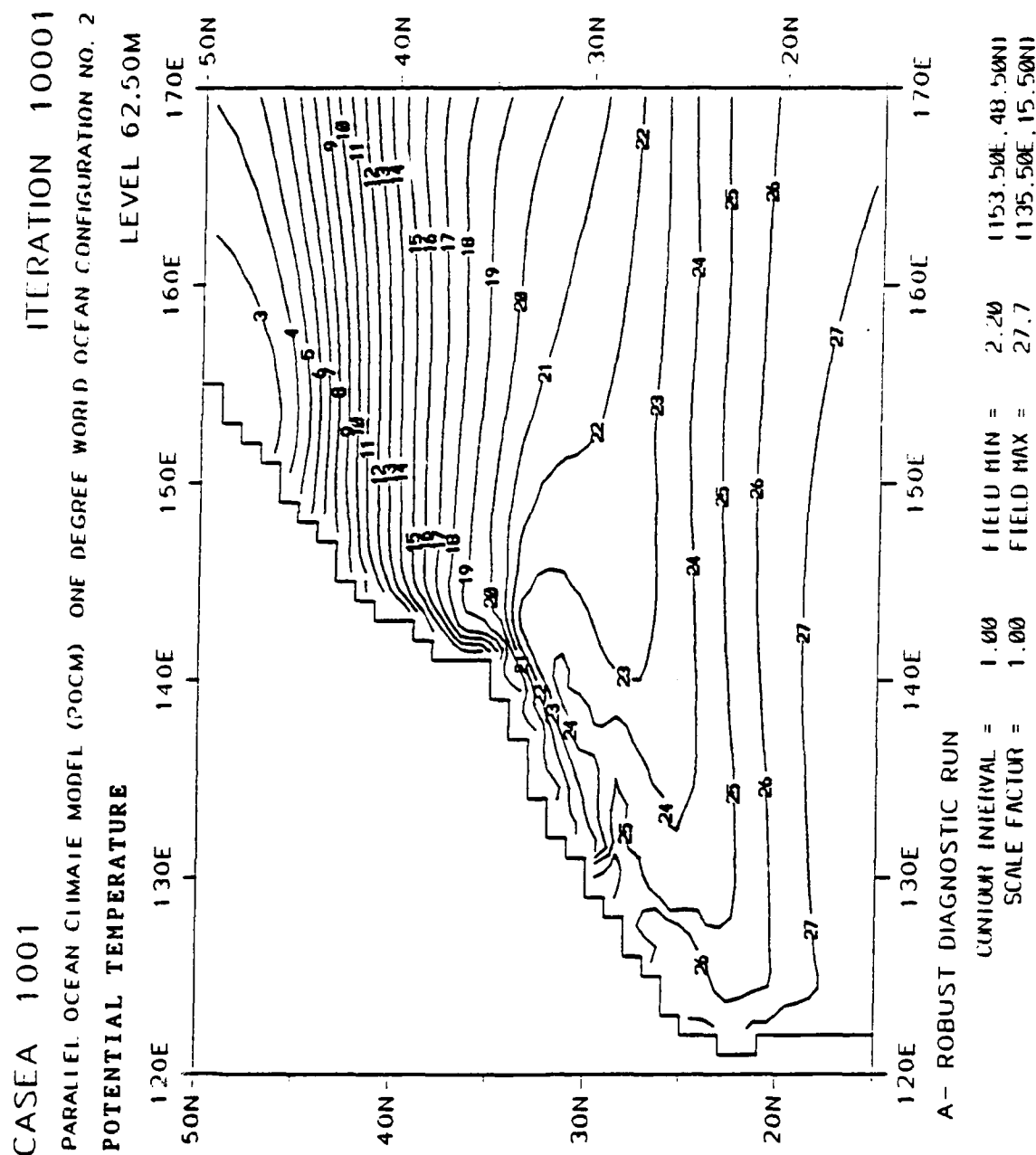


Figure 3.10 Potential temperature in °C at 62.5 m depth in the Kuroshio Current region for experiment 1.

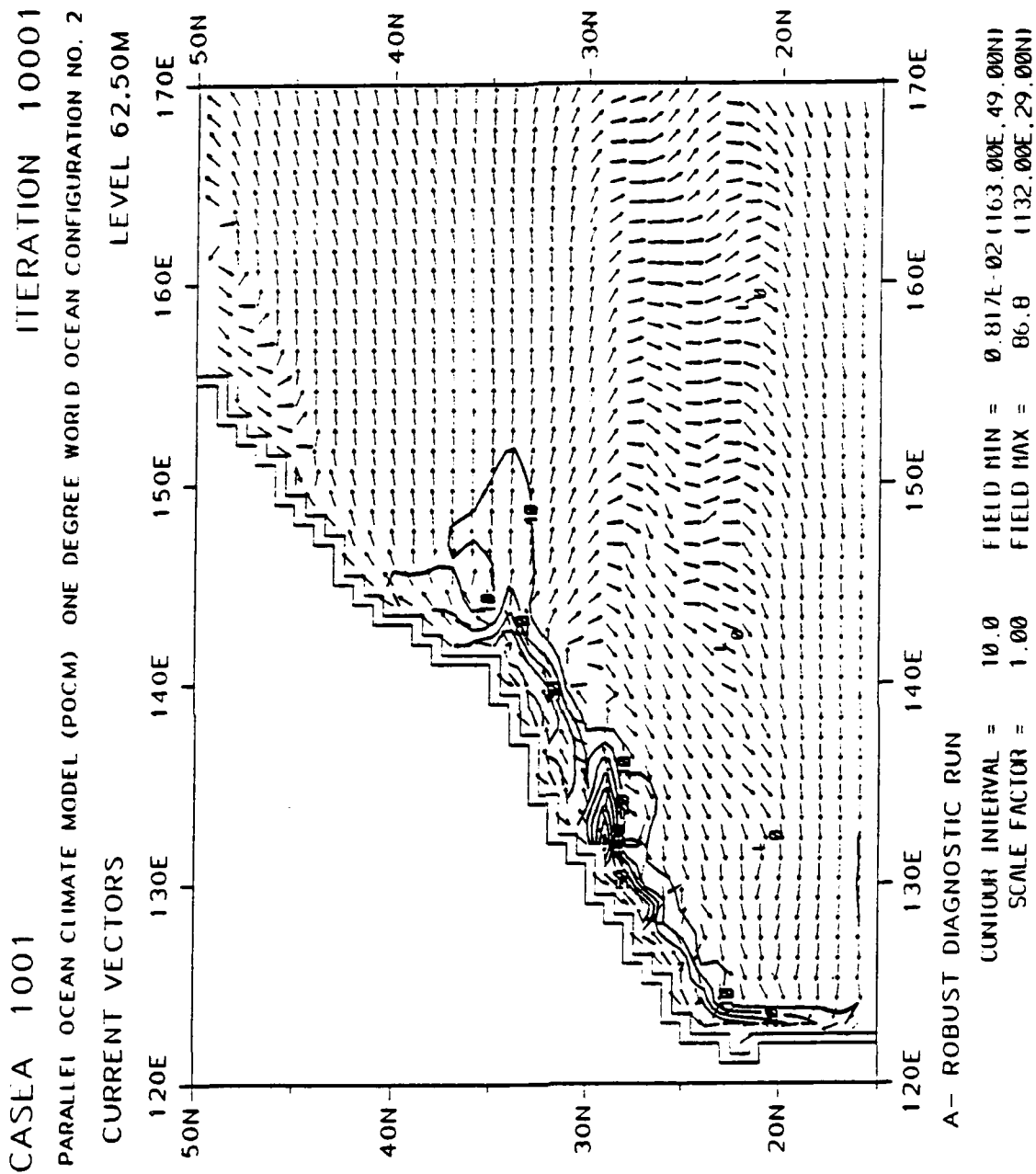


Figure 3.11 Fixed-length current vectors (with superimposed speed contours in cm s^{-1}) at 62.5 m depth in the Kuroshio Current region for experiment 1.

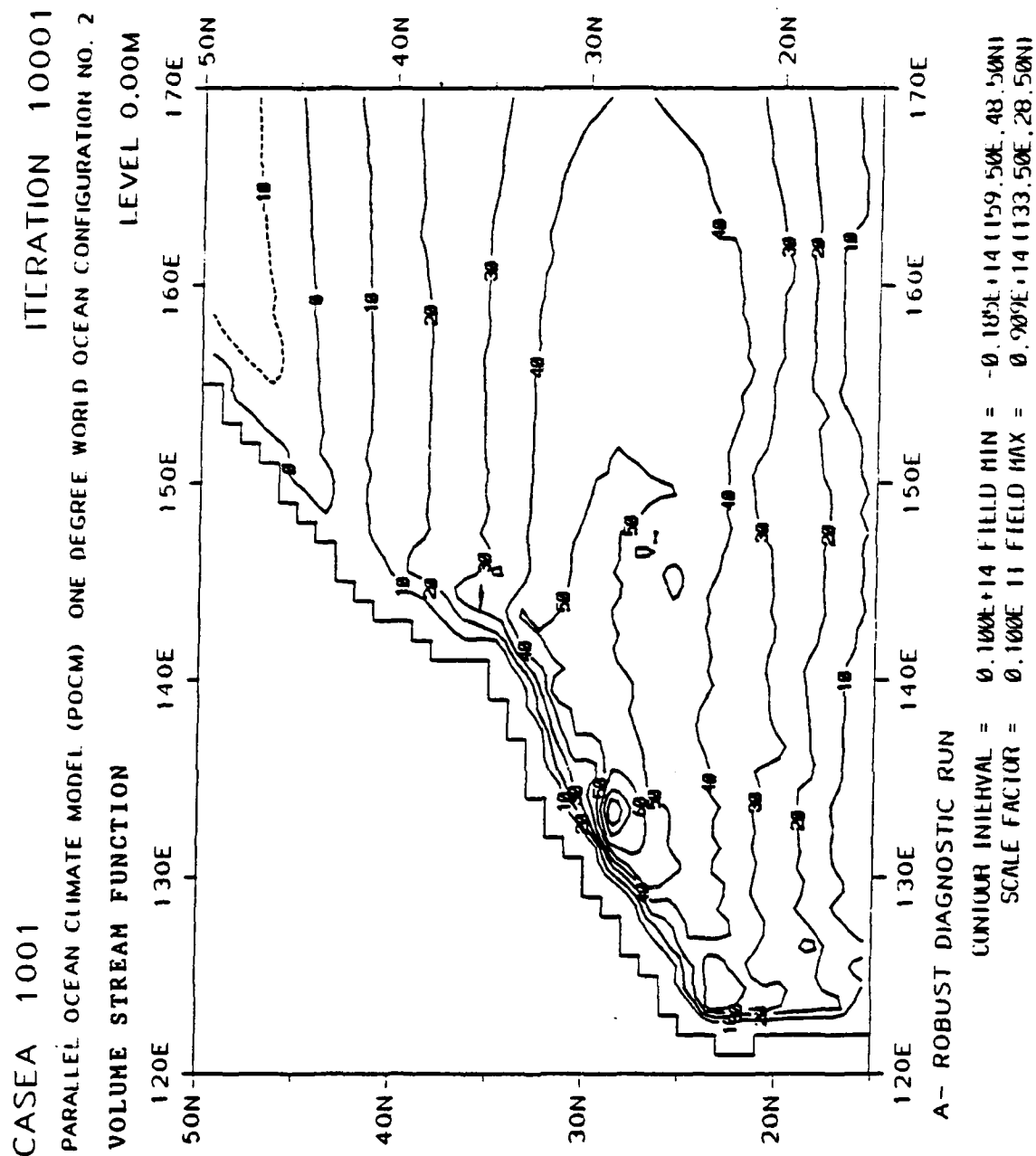


Figure 3.12 Horizontal volume transport in Sv ($-10^{12} \text{ cm}^3 \text{ s}^{-1}$) in the Kuroshio Current region for experiment 1.

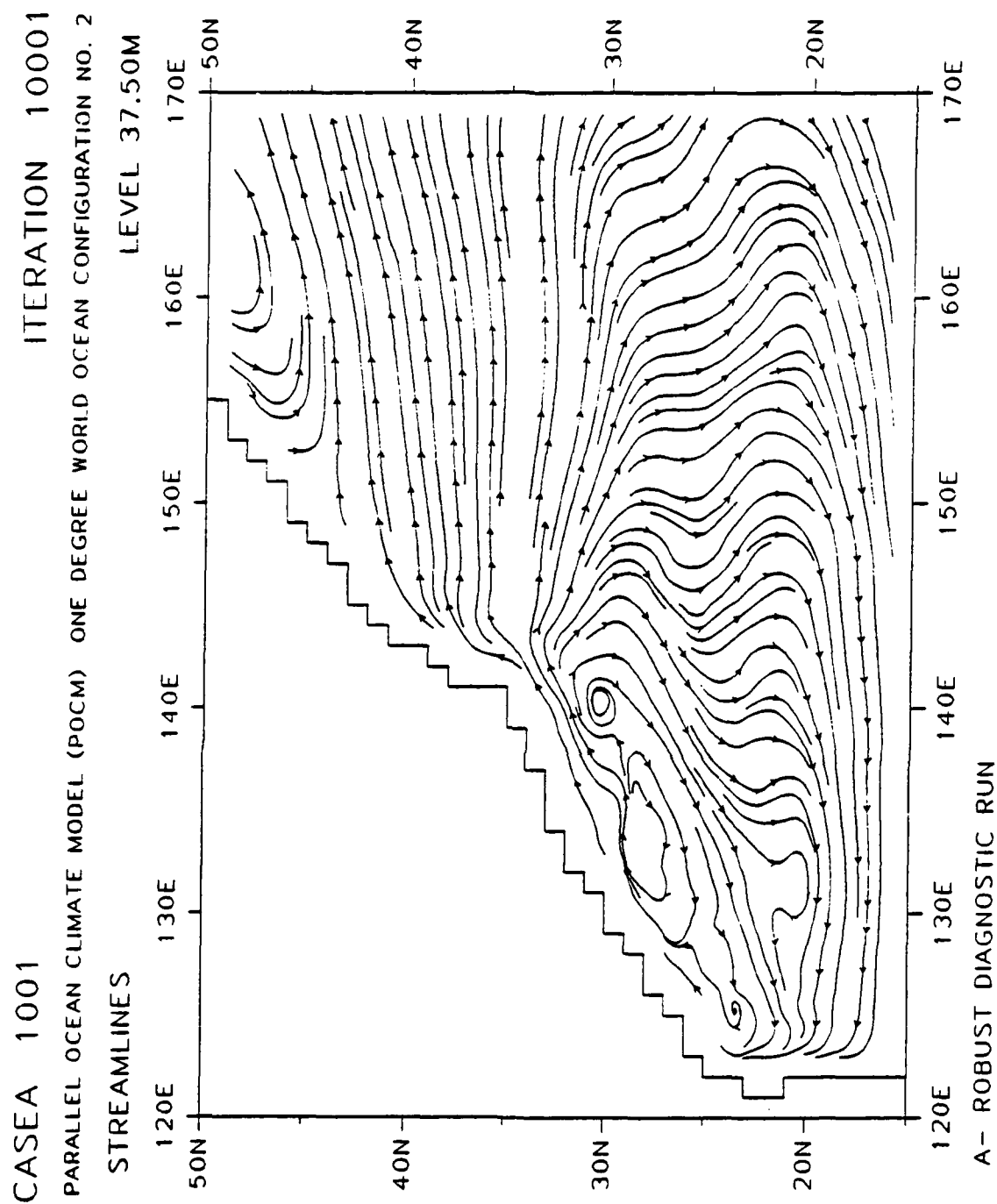


Figure 3.13

Streamlines at 37.5 m depth in the Kuroshio Current region for experiment 1. Streamlines are everywhere tangent to the current vectors and are selectively originated/discontinued to maintain neat-uniform spacing.

CASEA 1001

ITERATION 10001

PARALLEL OCEAN CLIMATE MODEL (POCM) ONE DEGREE WORLD OCEAN CONFIGURATION NO. 2
STREAMLINES

LEVEL 1542.50M

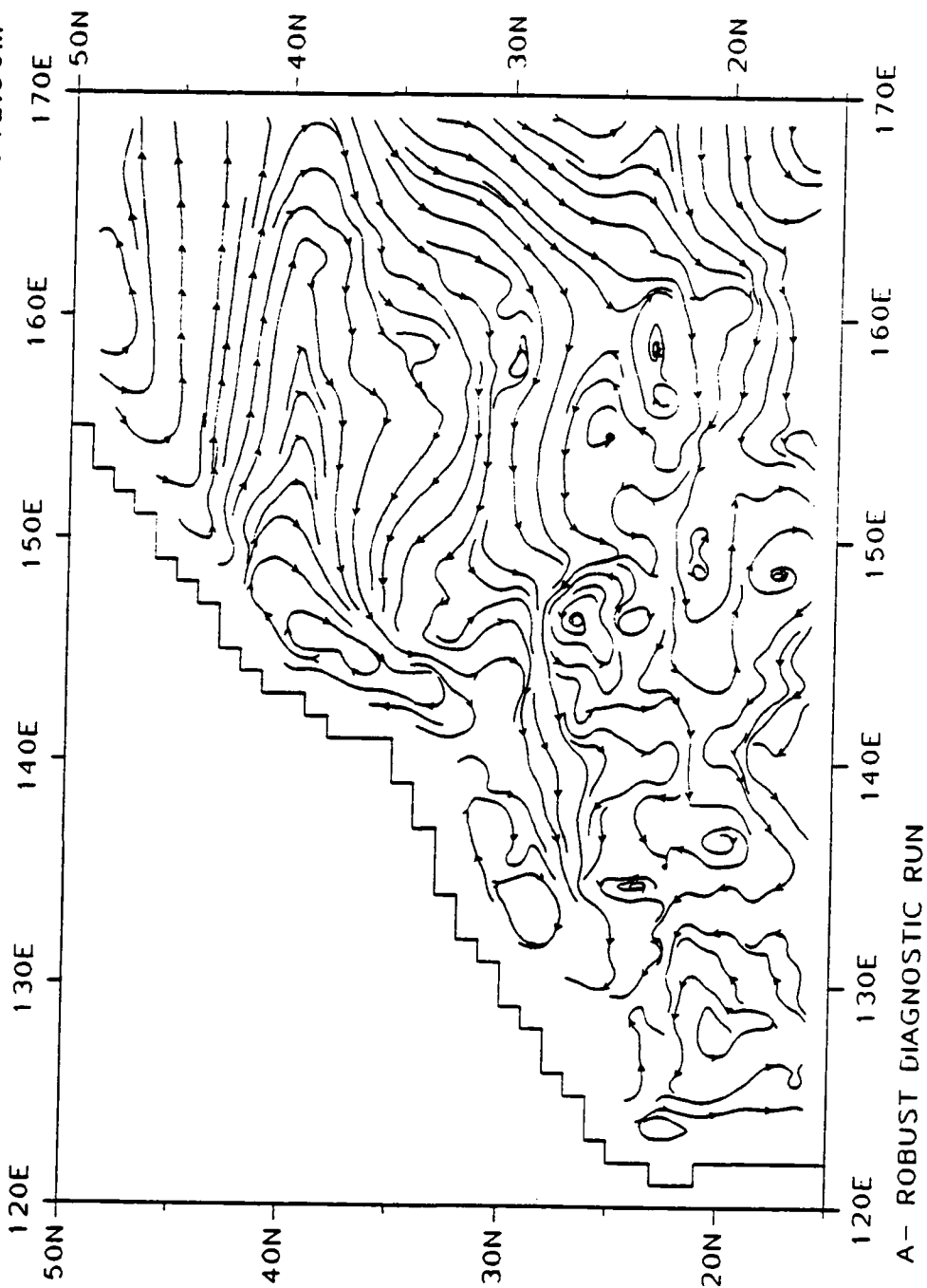
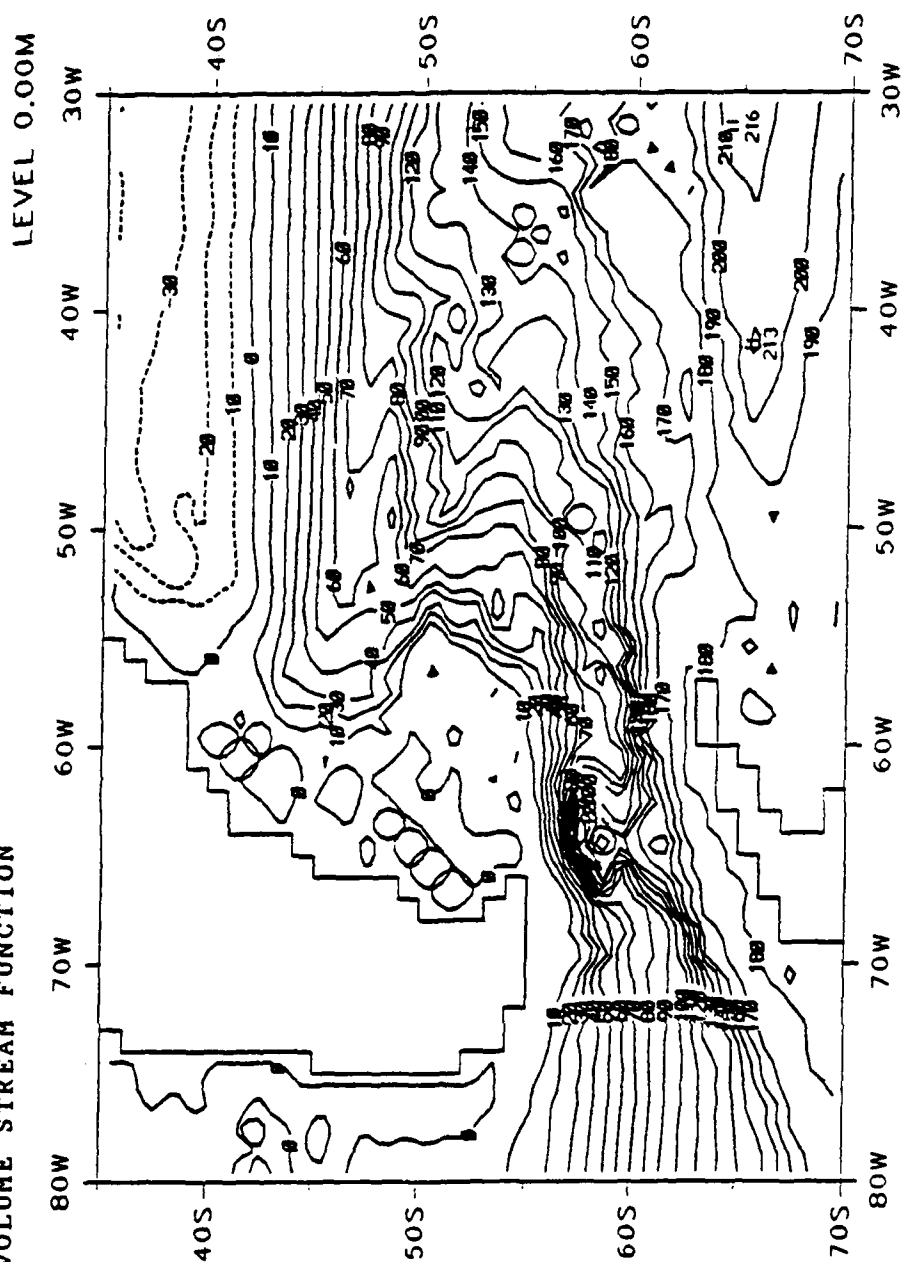


Figure 3.14

Streamlines at 1542.5 m depth in the Kuroshio Current region for experiment 1. Streamlines are everywhere tangent to the current vectors and are selectively originated/discontinued to maintain near-uniform spacing.

ITERATION 10001

PARALLEL OCEAN CLIMATE MODEL (POCM) ONE DEGREE WORLD OCEAN CONFIGURATION NO. 2
VOLUME STREAM FUNCTION

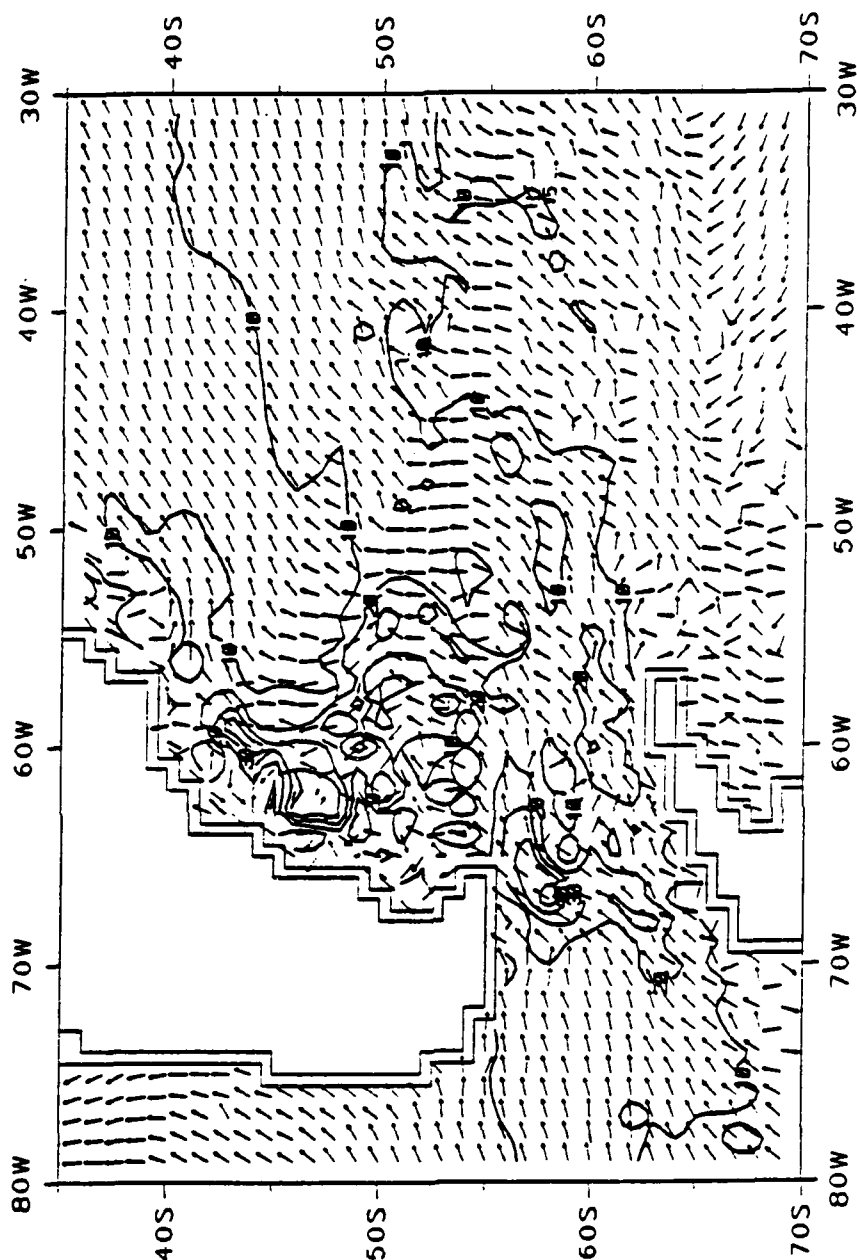


A- ROBUST DIAGNOSTIC RUN

```
CONTOUR INTERVAL = 0.100E+14 FIELD MIN = -0.402E+14 (34.50W,35.50S)
SCALE FACTOR = 0.100E-11 FIELD MAX = 0.216E+15 (31.50W,64.50S)
```

Figure 3.15 Horizontal volume transport in $\text{Sv} (10^{12} \text{ cm}^3 \text{ s}^{-1})$ in the Drake Passage region for experiment 1.

CASEA 1001
 PARALLEL OCEAN CLIMATE MODEL (POCM) ONE DEGREE WORLD OCEAN CONFIGURATION NO. 2
 CURRENT VECTORS
 LEVEL 12.50M
 ITERATION 10001



A- ROBUST DIAGNOSTIC RUN

CONTOUR INTERVAL =	10.0	FIELD MIN =	0.136	168.00W, 66.00S)
SCALE FACTOR =	1.00	FIELD MAX =	59.1	167.00W, 58.00S)

Figure 3.16 Fixed-length current vectors (with superimposed speed contours in cm s^{-1}) at 12.5 m depth in the Drake Passage region for experiment 1.

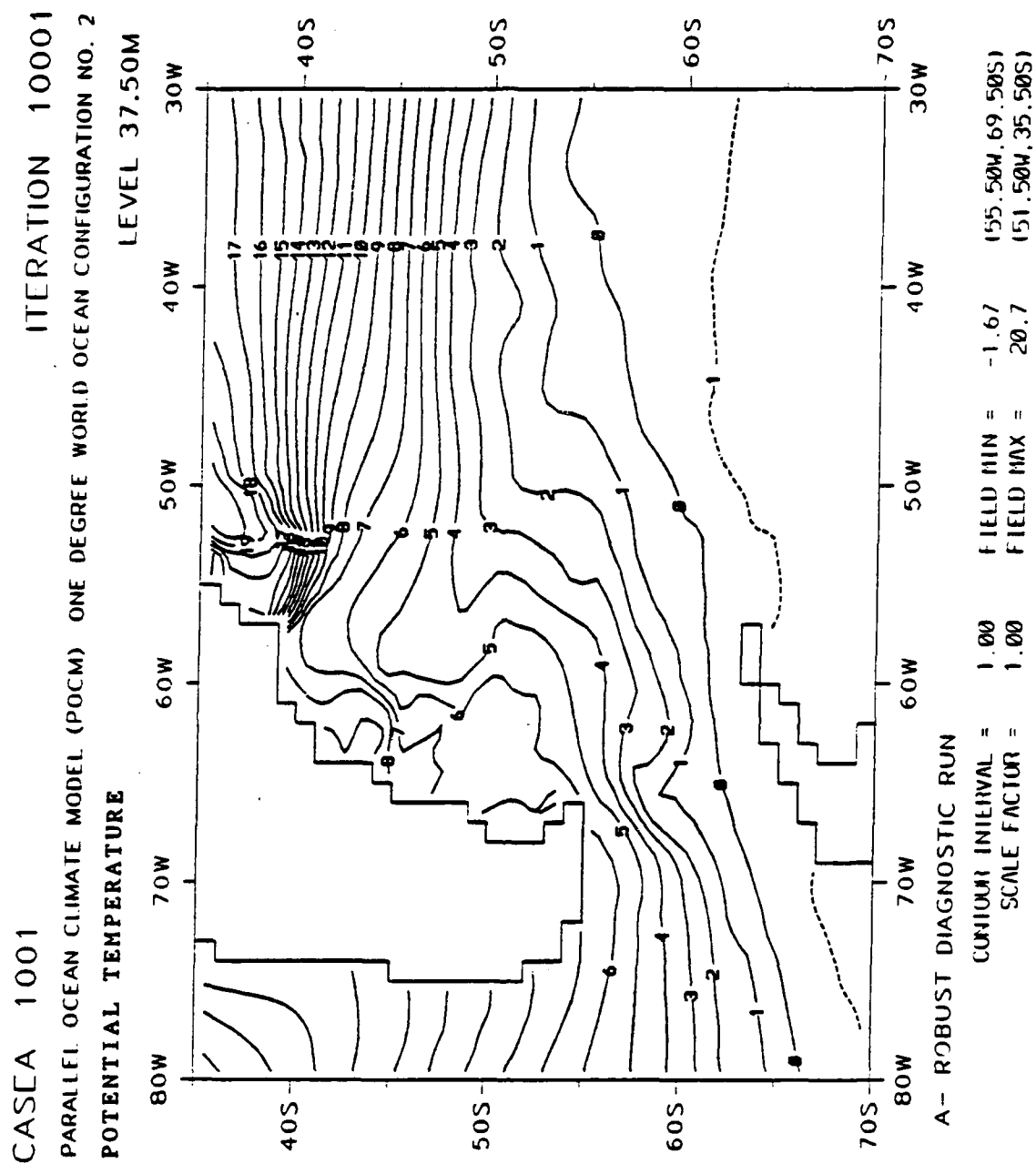


Figure 3.17 Potential temperature in °C at 37.5 m depth in the Drake Passage region for experiment 1.

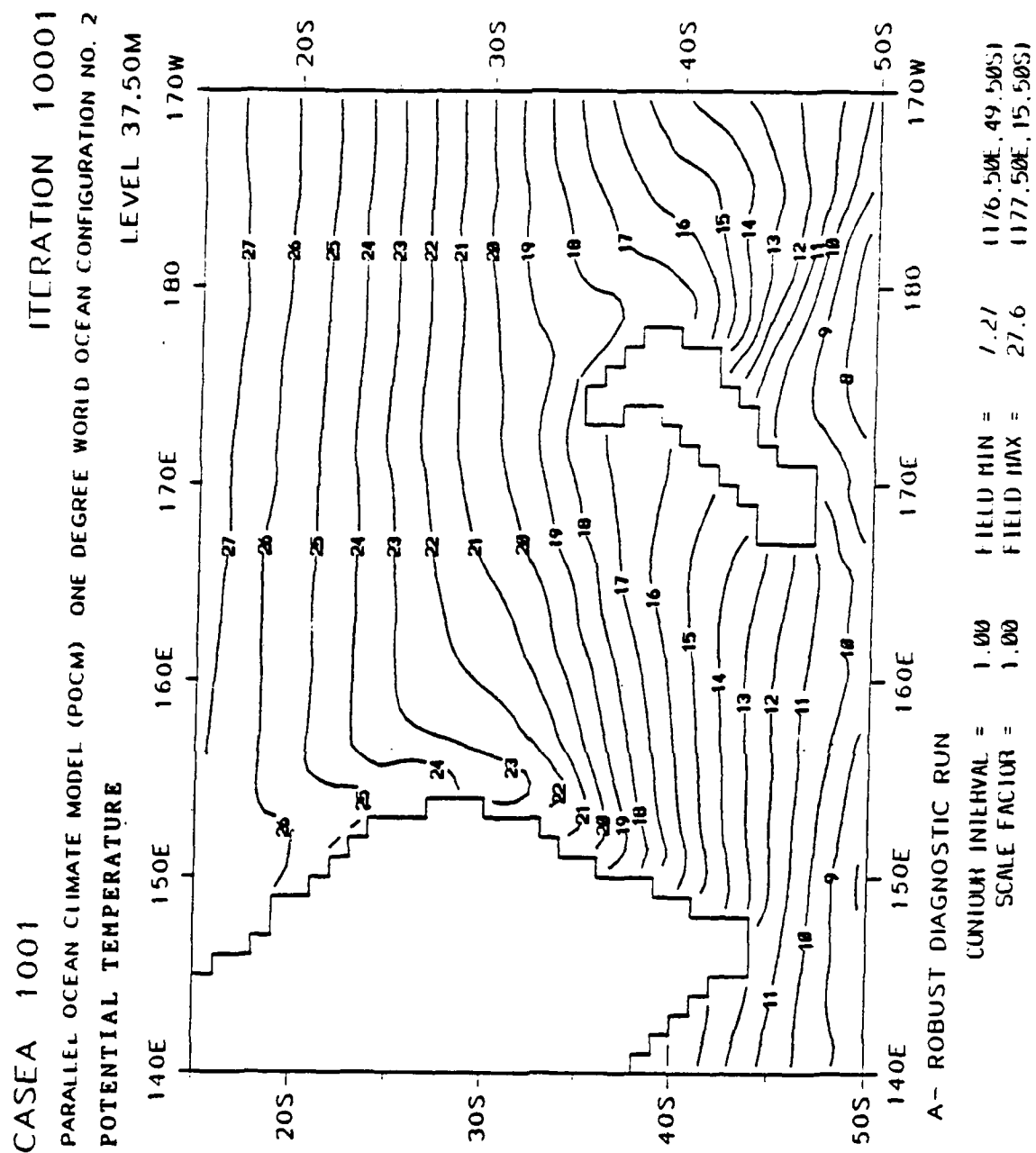


Figure 3.18 Potential temperature in $^{\circ}\text{C}$ at 37.5 m depth in the East Australian Current region for experiment 1.

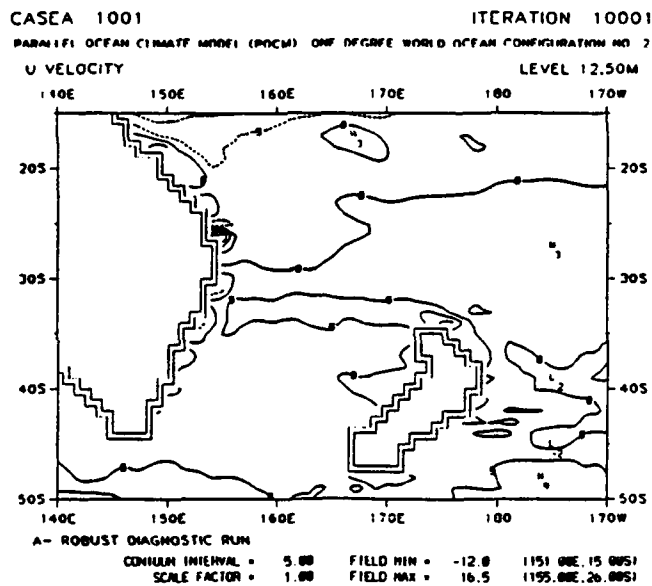
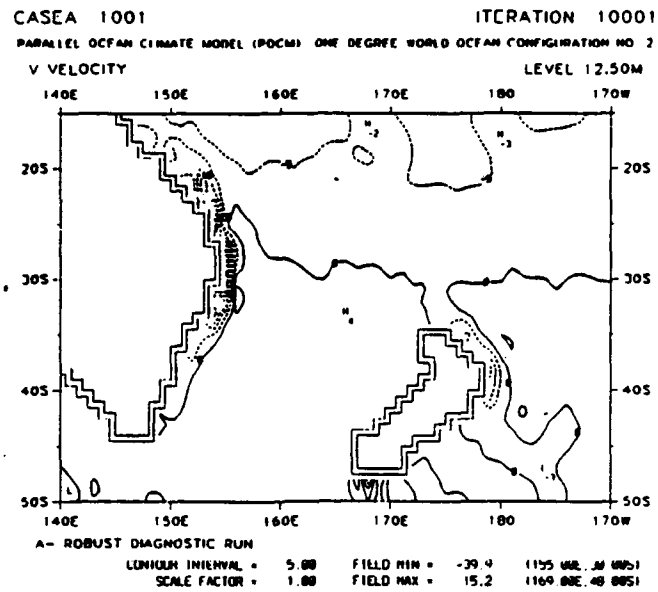


Figure 3.19 (a) Meridional and (b) zonal velocity in cm s^{-1} at 12.5 m depth in the East Australian Current region for experiment 1.

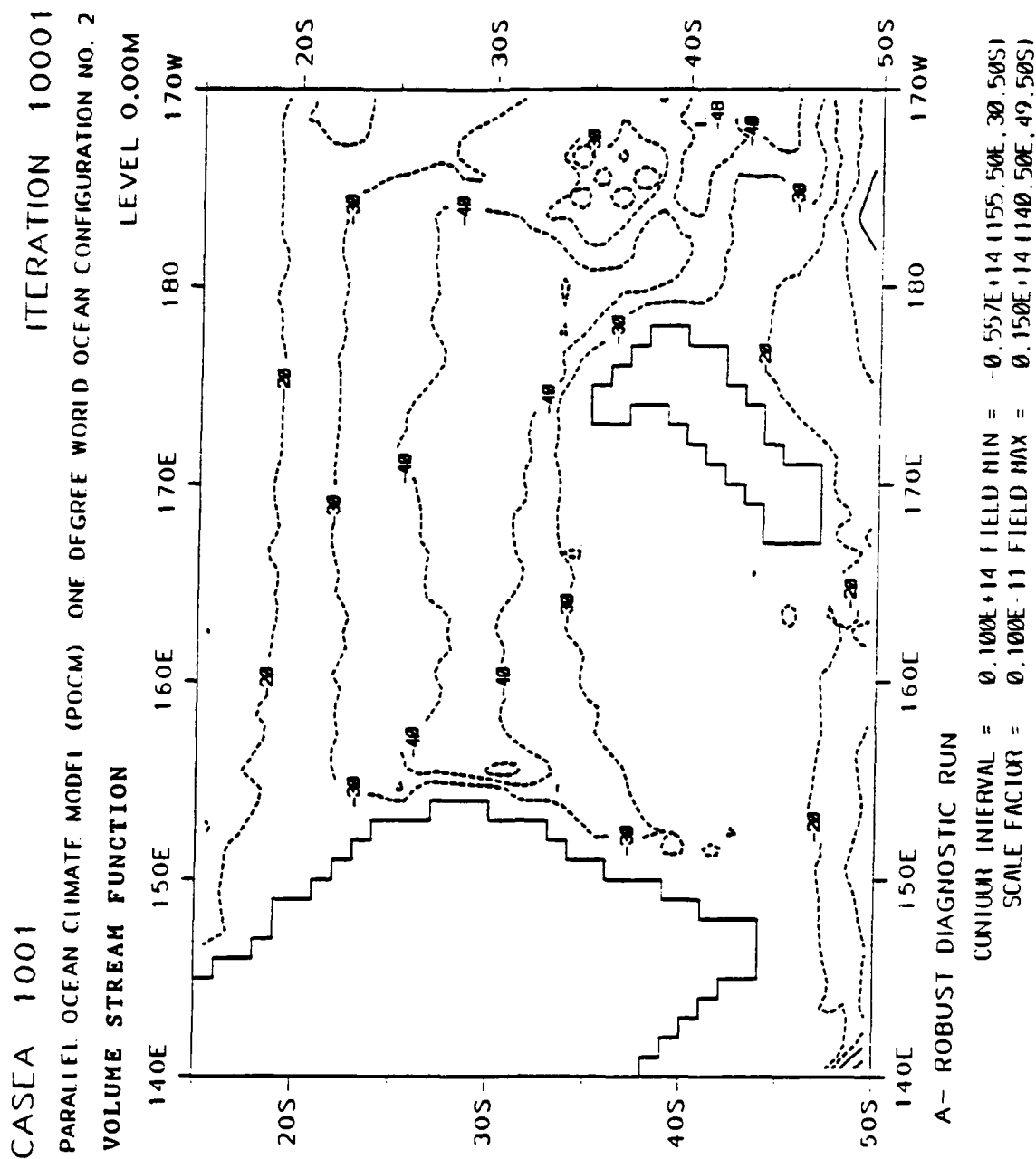


Figure 3.20 Horizontal volume transport in $\text{Sv} (=10^{12} \text{ cm}^3 \text{ s}^{-1})$ in the East Australian Current region for experiment 1.

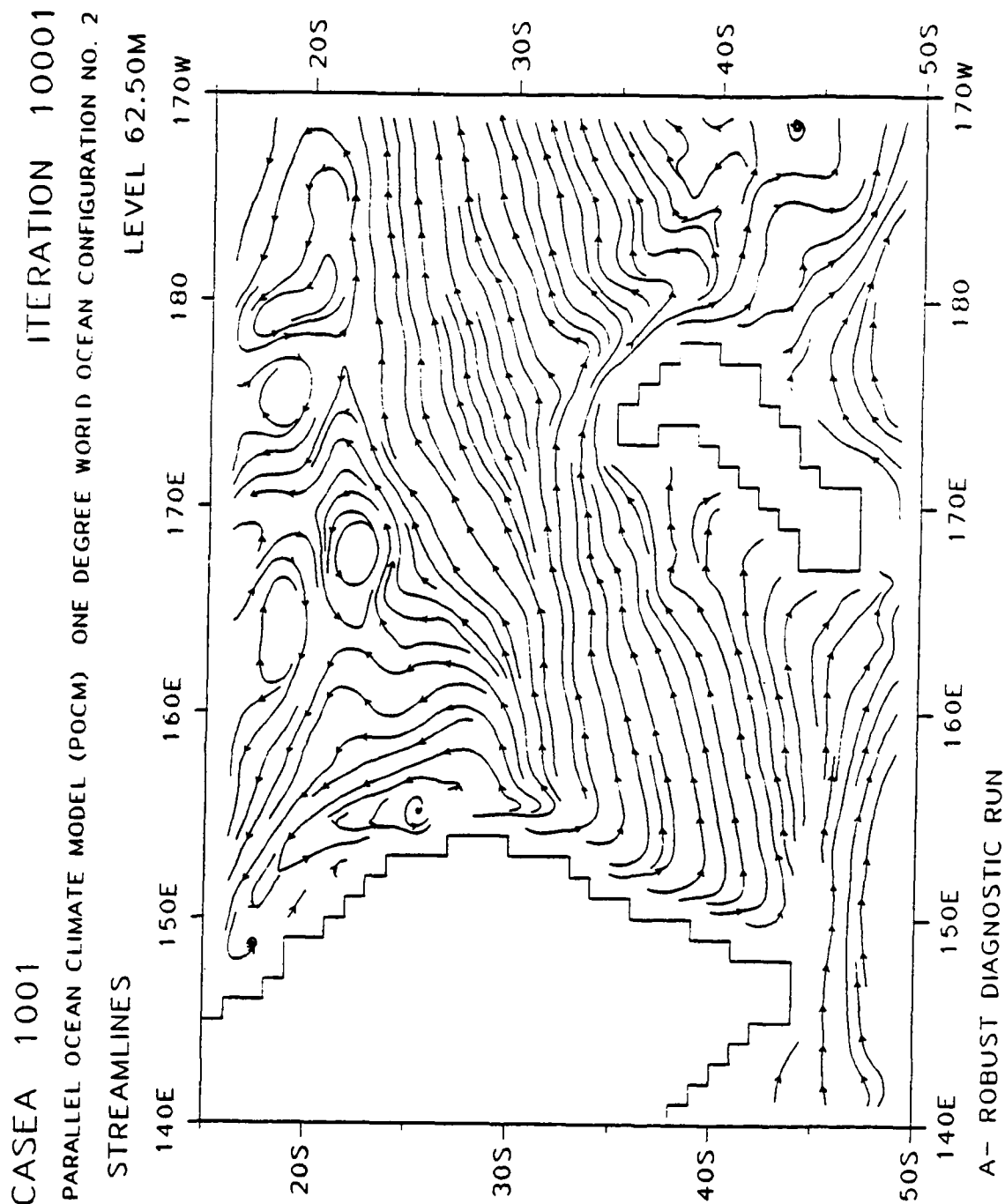


Figure 3.21 Streamlines at 62.5 m depth in the East Australian Current region for experiment 1. Streamlines are everywhere tangent to the current vectors and are selectively originated/discontinued to maintain near-uniform spacing.

CASEA 1001 ITERATION 10001
 PARALLEL OCEAN CLIMATE MODEL (POCM) ONE DEGREE WORLD OCEAN CONFIGURATION NO. 2
 POTENTIAL TEMPERATURE LEVEL 37.50M

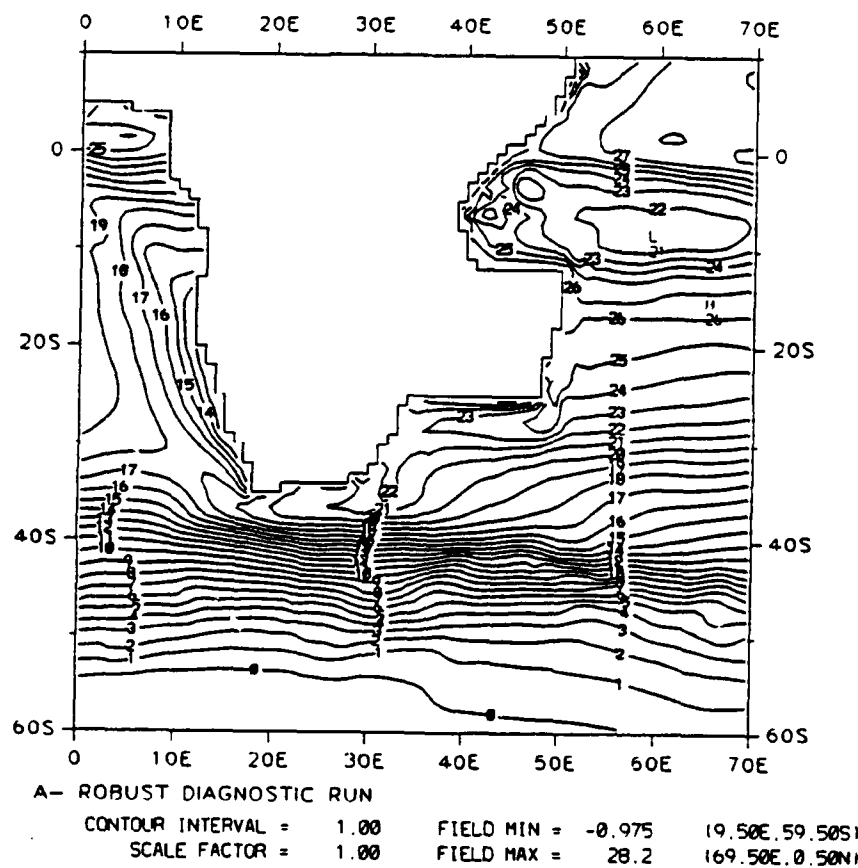


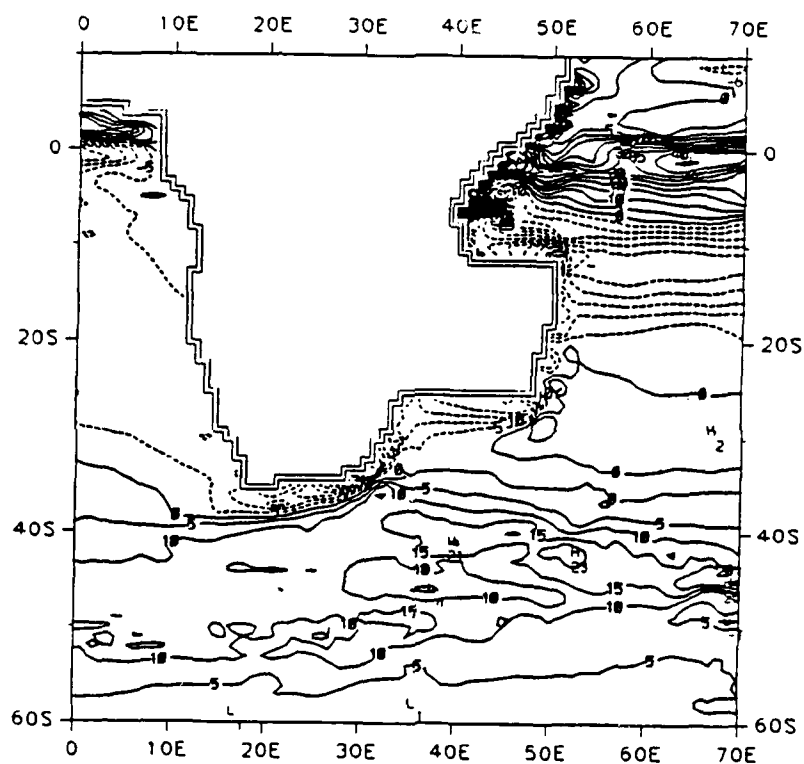
Figure 3.22 Potential temperature in °C at 37.5 m depth in the Agulhas Current region for experiment 1.

CASEA 1001
 PARALLEL OCEAN CLIMATE MODEL (POCM) ONE DEGREE WORLD OCEAN CONFIGURATION NO. 2

ITERATION 10001

U VELOCITY

LEVEL 12.50M



A- ROBUST DIAGNOSTIC RUN

CONTOUR INTERVAL = 5.00

SCALE FACTOR = 1.00

FIELD MIN = -83.6 (41.00E, 7.00S)

FIELD MAX = 103. (41.00E, 6.00S)

Figure 3.23 Zonal velocity in cm s^{-1} at 12.5 m depth in the Agulhas Current region for experiment 1.

CASEA 1001 ITERATION 10001
 PARALLEL OCEAN CLIMATE MODEL (POCM) ONE DEGREE WORLD OCEAN CONFIGURATION NO. 2

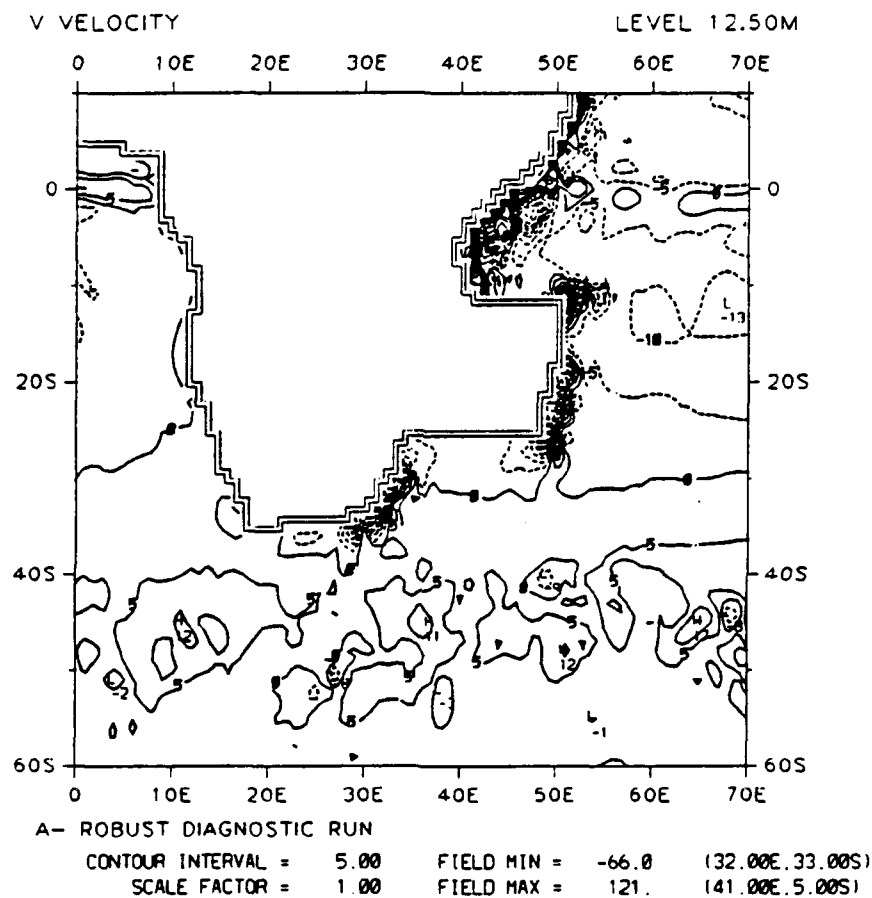


Figure 3.24 Meridional velocity in cm s^{-1} at 12.5 depth in the Agulhas Current region for experiment 1.

CONTOUR INTERVAL = 0.100E+14 FIELD MIN = -0.835E+14 (32.50E, 33.50S)
SCALE FACTOR = 0.100E-11 FIELD MAX = 0.206E+15 (9.50E, 57.50S)

69

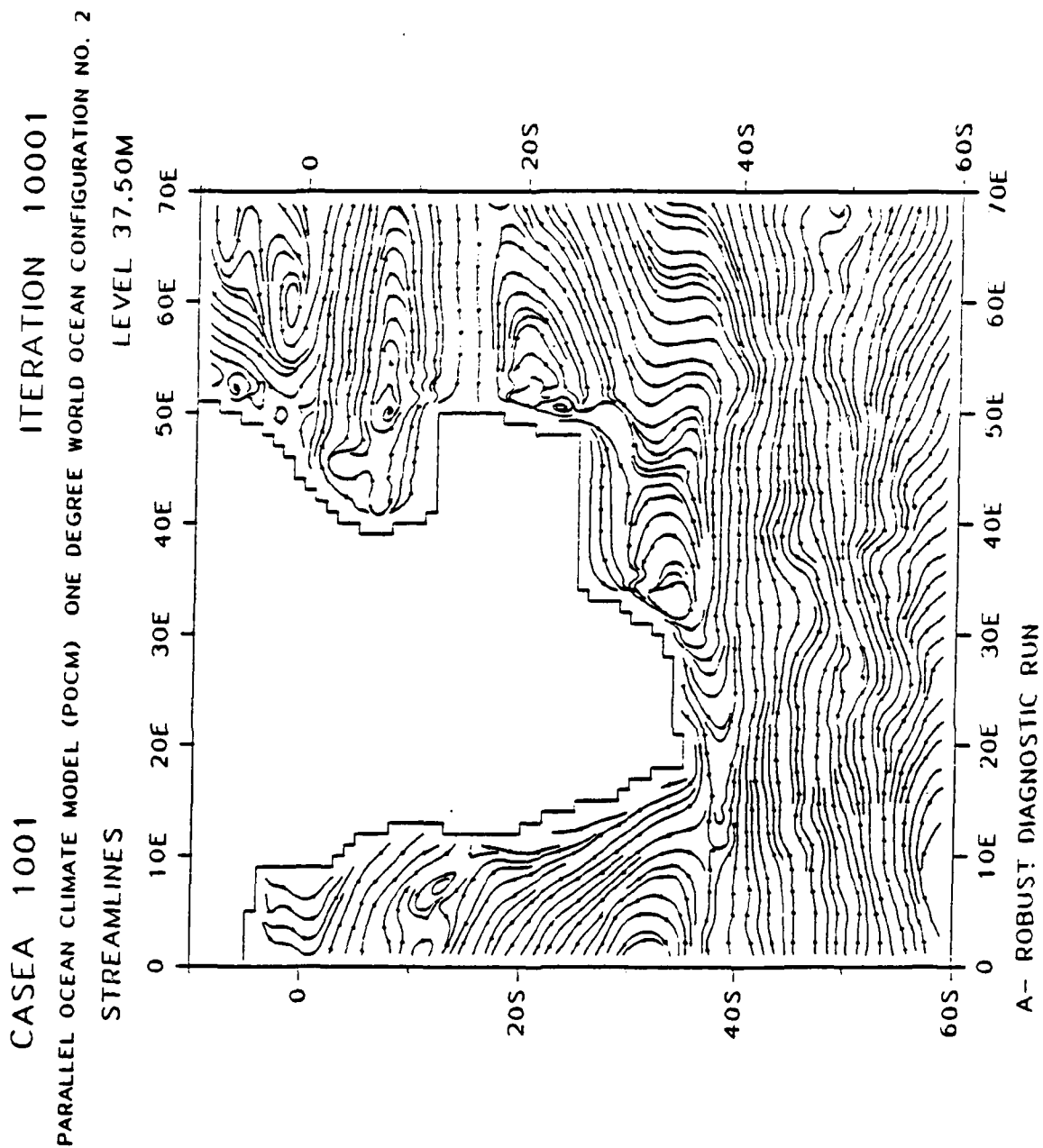


Figure 3.26

Streamlines at 37.5 m depth in the Agulhas Current region for experiment 1. Streamlines are everywhere tangent to the current vectors and are selectively originated/discontinued to maintain near-uniform spacing.

CASEA 1001 ITERATION 10001
 PARALLEL OCEAN CLIMATE MODEL (POCM) ONE DEGREE WORLD OCEAN CONFIGURATION NO. 2
 VOLUME STREAM FUNCTION LEVEL 0.00M

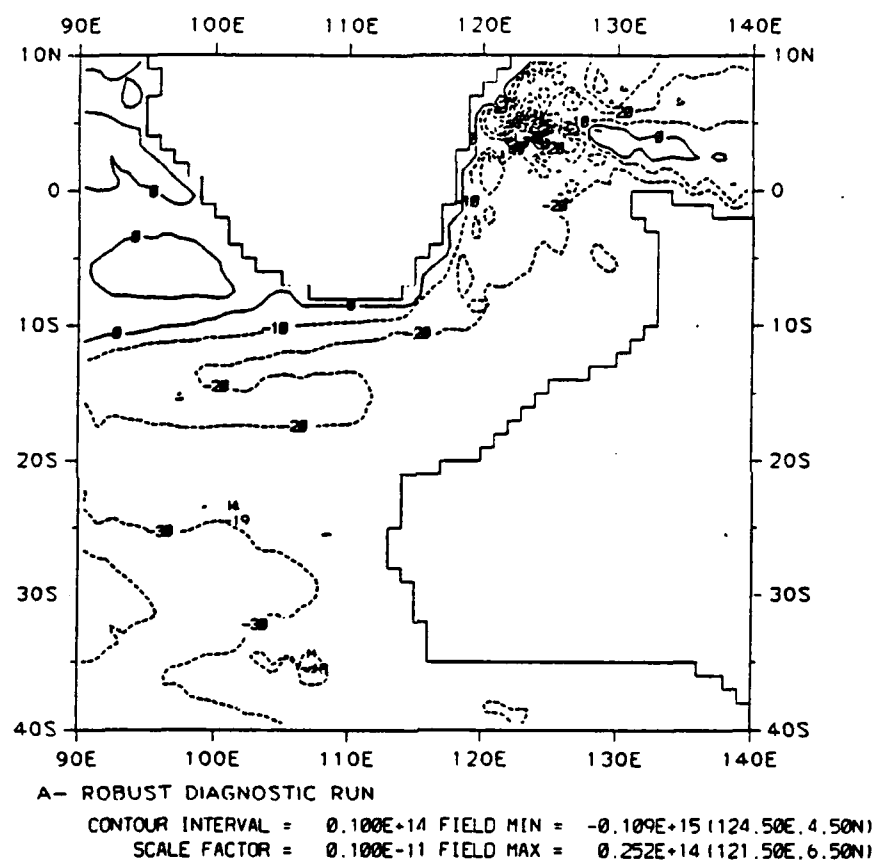


Figure 3.27 Horizontal volume transport in $\text{Sv}(-10^{12} \text{ cm}^3 \text{ s}^{-1})$ in the western Australia region for experiment 1.

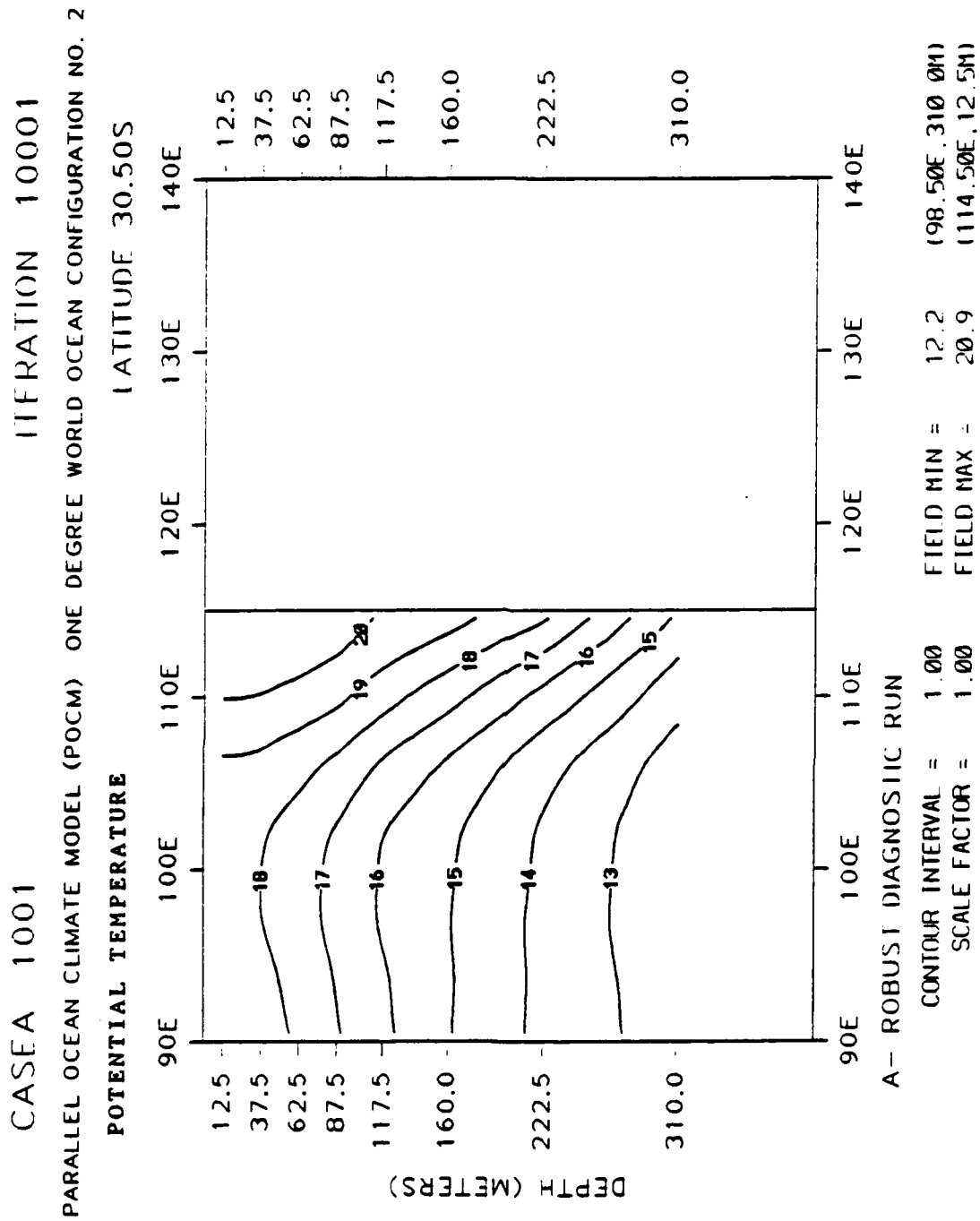


Figure 3.28 Zonal cross-section of potential temperature in °C at 30.5°S latitude off of western Australia for experiment 1.

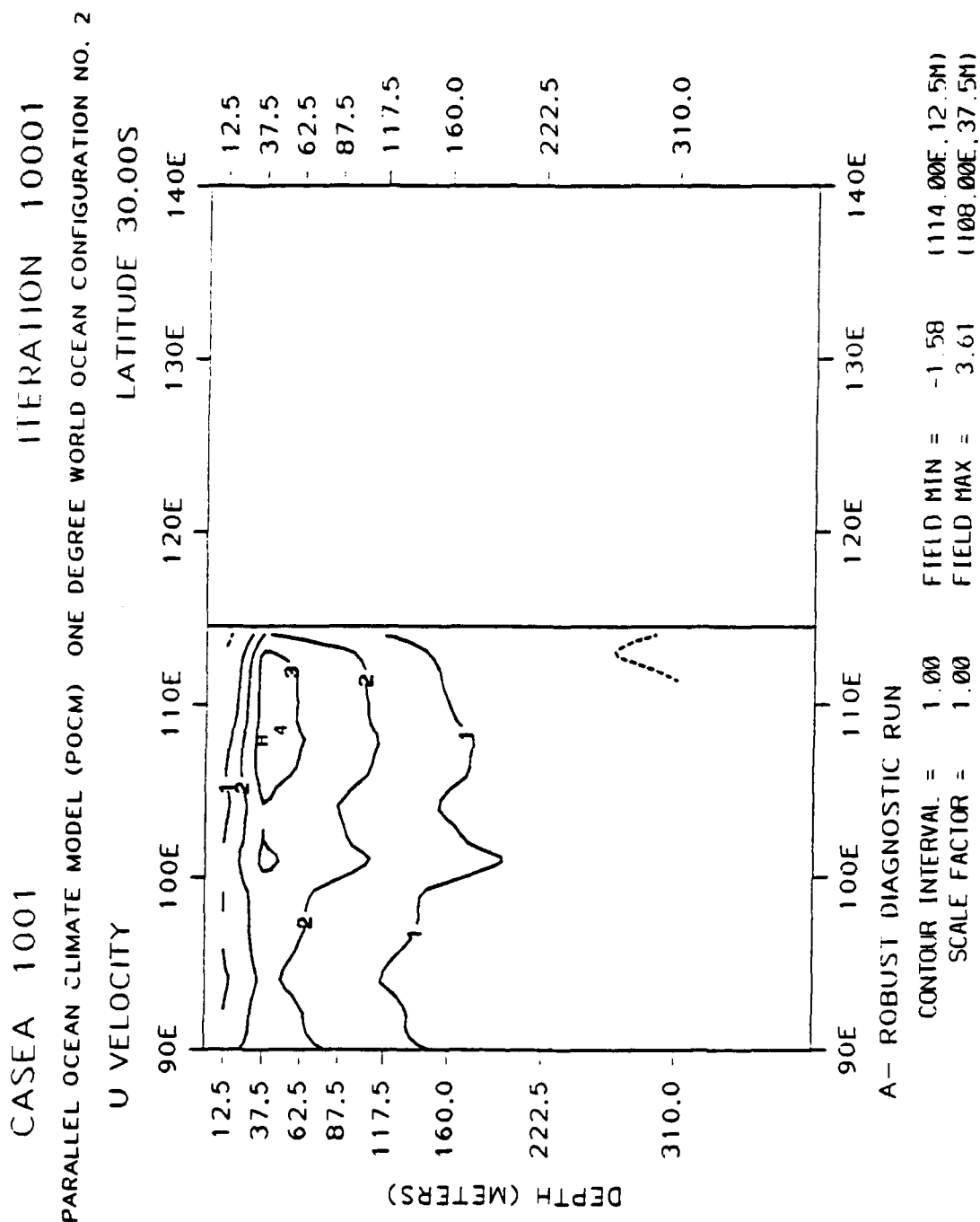


Figure 3.29 Zonal cross-section of zonal velocity in cm s^{-1} at 30.0°S latitude off of western Australia for experiment 1.

CASEA 1001 ITERATION 10001
 PARALLEL OCEAN CLIMATE MODEL (POCM) ONE DEGREE WORLD OCEAN CONFIGURATION NO. 2
 V VELOCITY LATITUDE 30.00S

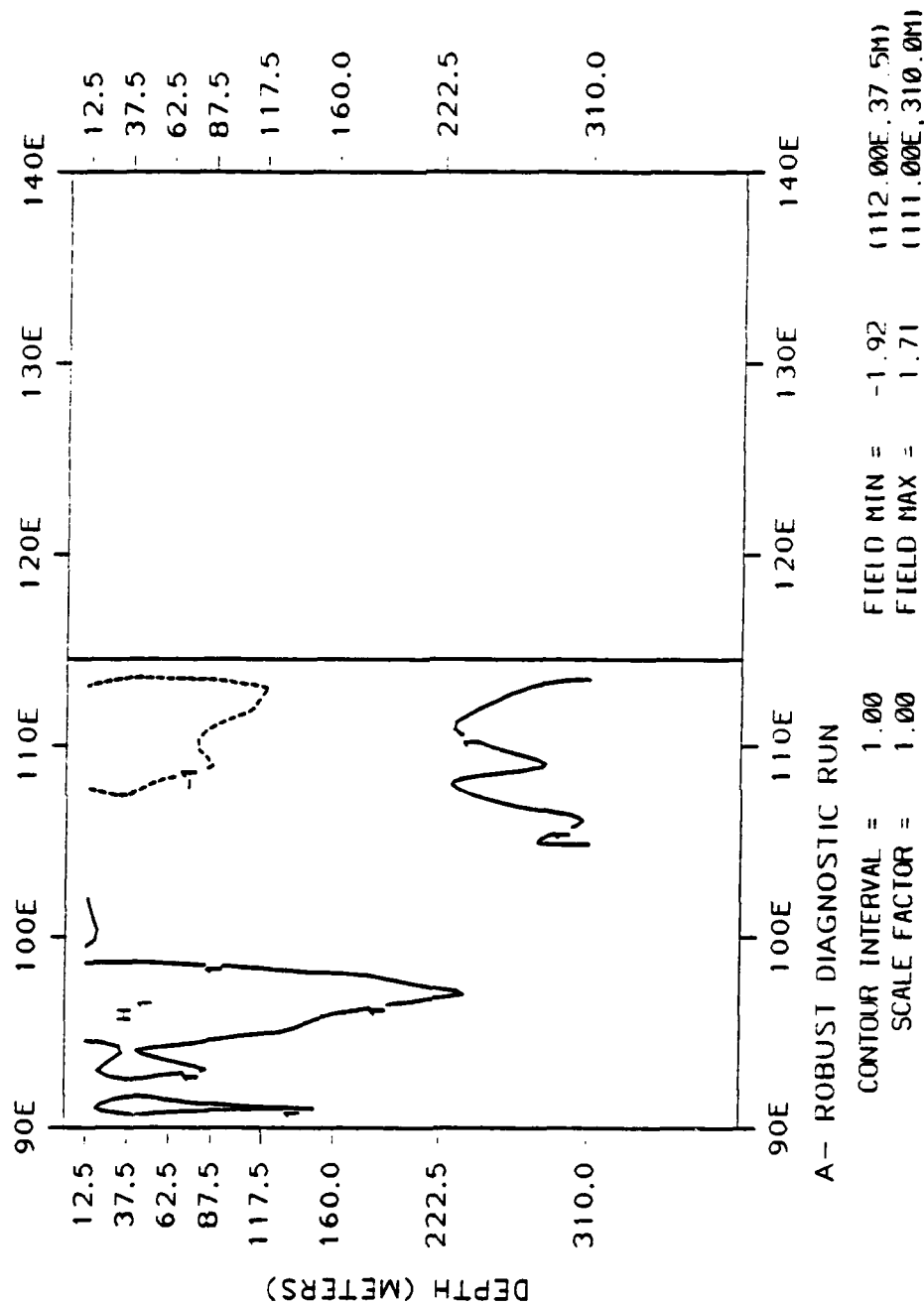


Figure 3.30 Zonal cross-section of meridional velocity in cm s^{-1} at 30.0°S latitude off of western Australia for experiment 1.

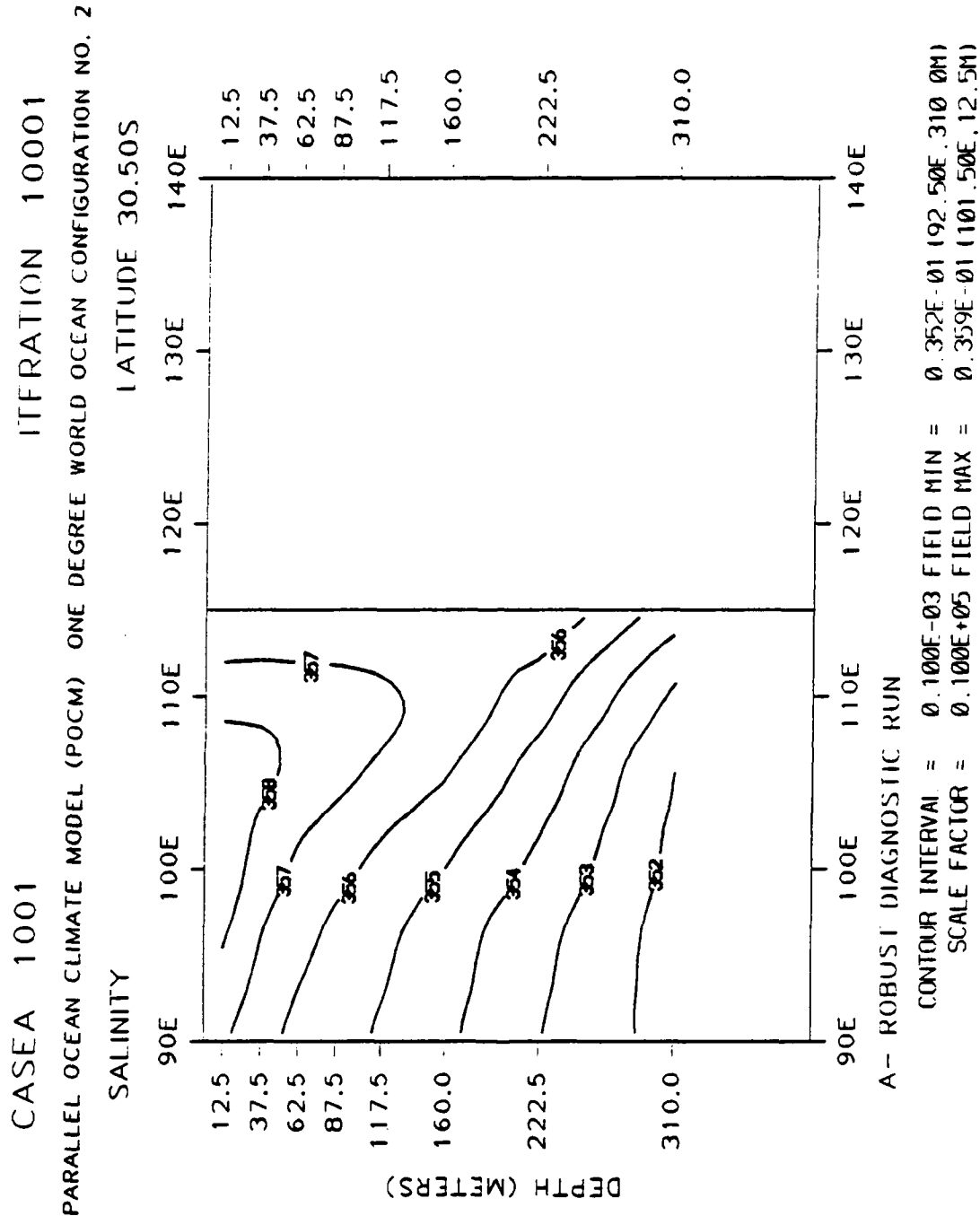
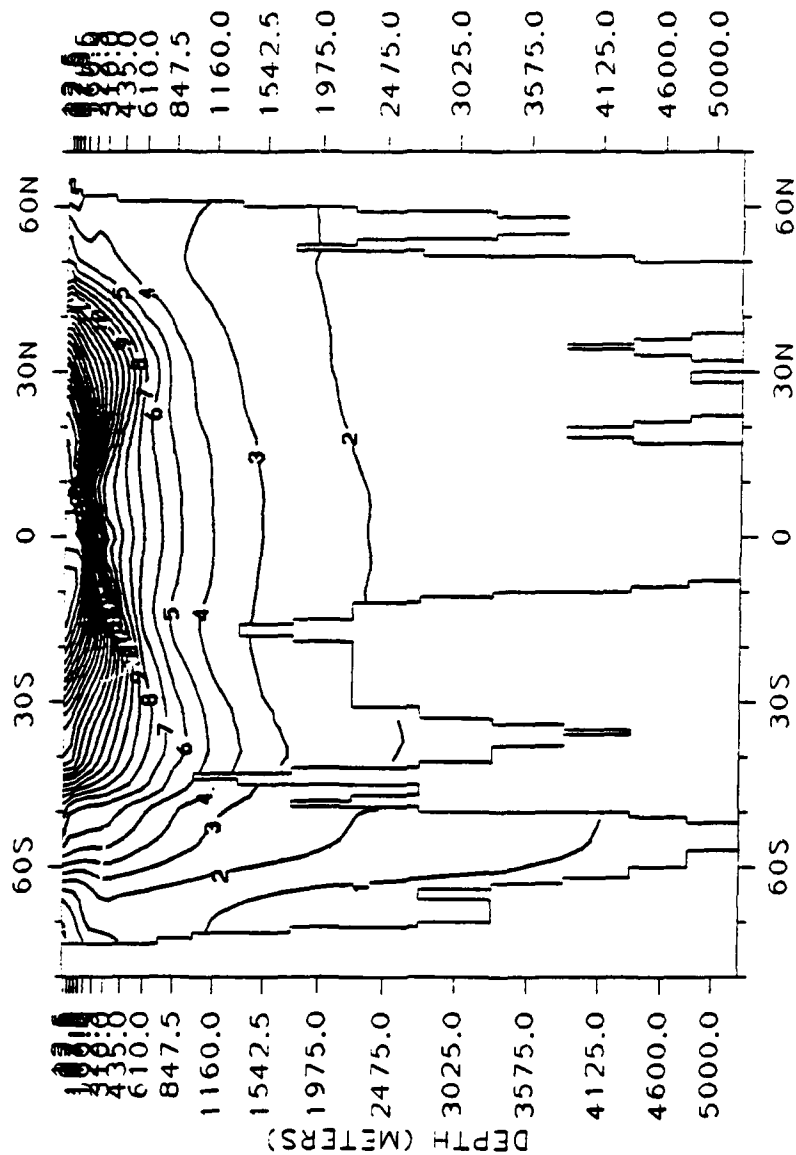


Figure 3.31 Zonal cross-section of salinity in units of 0.1 PPT at 30.5°S latitude off of western Australia for experiment 1.

CASFA 1001 ITERATION 10001

PARALLEL OCEAN CLIMATE MODEL (POCM) ONE DEGREE WORLD OCEAN CONFIGURATION NO. 2

POTENTIAL TEMPERATURE LONGITUDE 179.50W



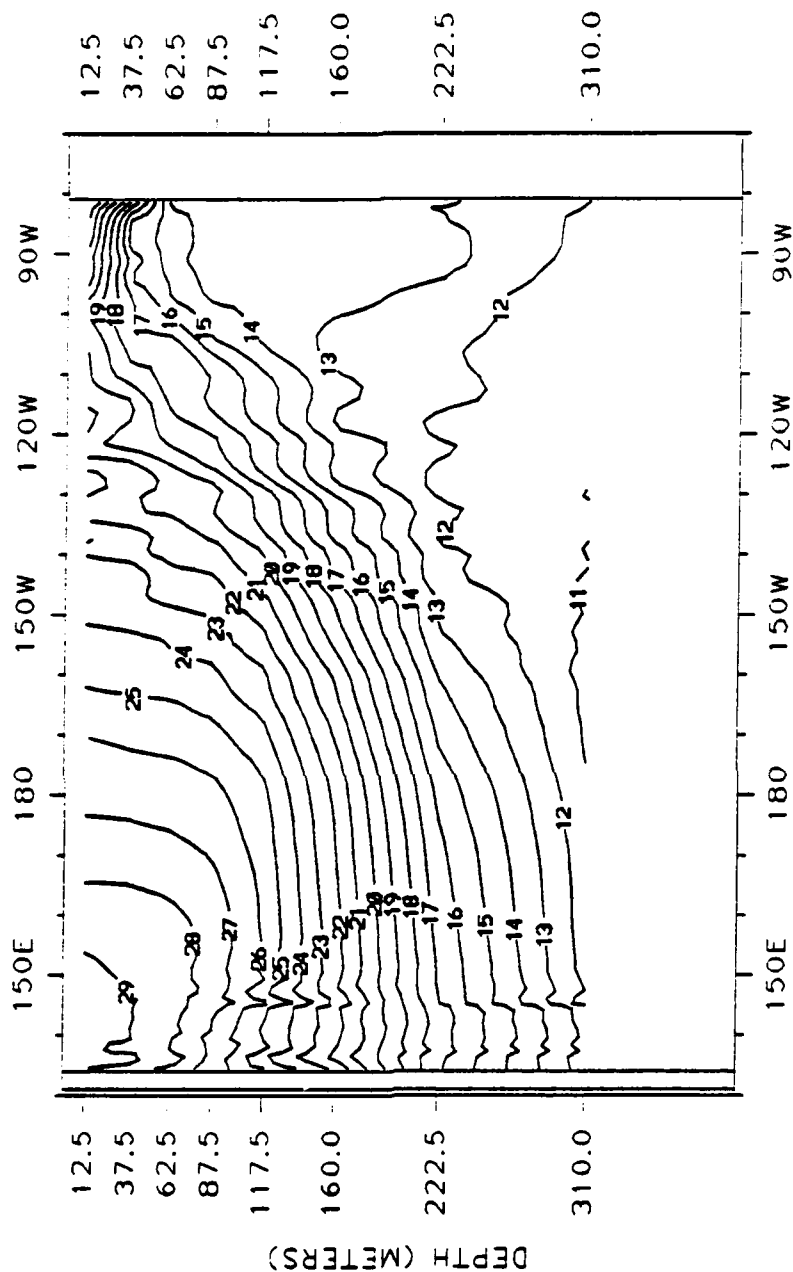
A- ROBUST DIAGNOSTIC RUN

CONTOUR INTERVAL = 1.00 FIELD MIN = -1.08 (73.50S, 12.5M)

SCALE FACTOR = 1.00 FIELD MAX = 29.0 (9.50S, 12.5M)

Figure 3.32 Meridional cross-section of potential temperature in °C at 179.5°W longitude for experiment 1.

CASEA 1001
 PARALLEL OCEAN CLIMATE MODEL (POCM) ONE DEGREE WORLD OCEAN CONFIGURATION NO. 2
 POTENTIAL TEMPERATURE
 LATITUDE 0.50S
 ITERATION 10001



A- ROBUST DIAGNOSTIC RUN
 CONTOUR INTERVAL = 1.00 FIELD MIN = 10.7 (159.50W, 310.0M)
 SCALE FACTOR = 1.00 FIELD MAX = 29.5 (146.50E, 12.5M)

Figure 3.33 Zonal cross-section of potential temperature in °C at 0.5°S latitude in the Pacific Ocean for experiment 1.

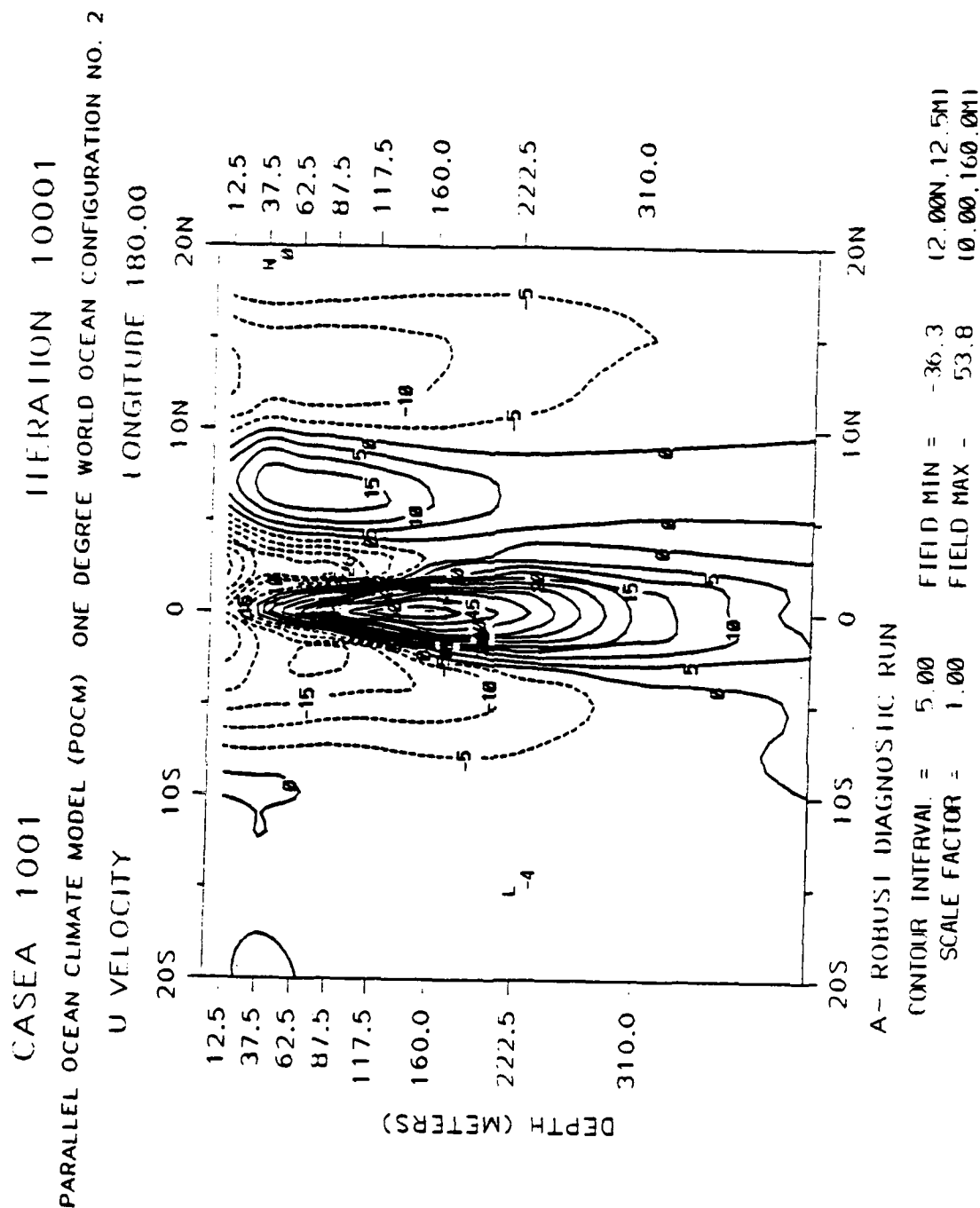


Figure 3.34 Meridional cross-section of zonal velocity in cm s^{-1} at 180.0° longitude in the equatorial Pacific region for experiment 1.

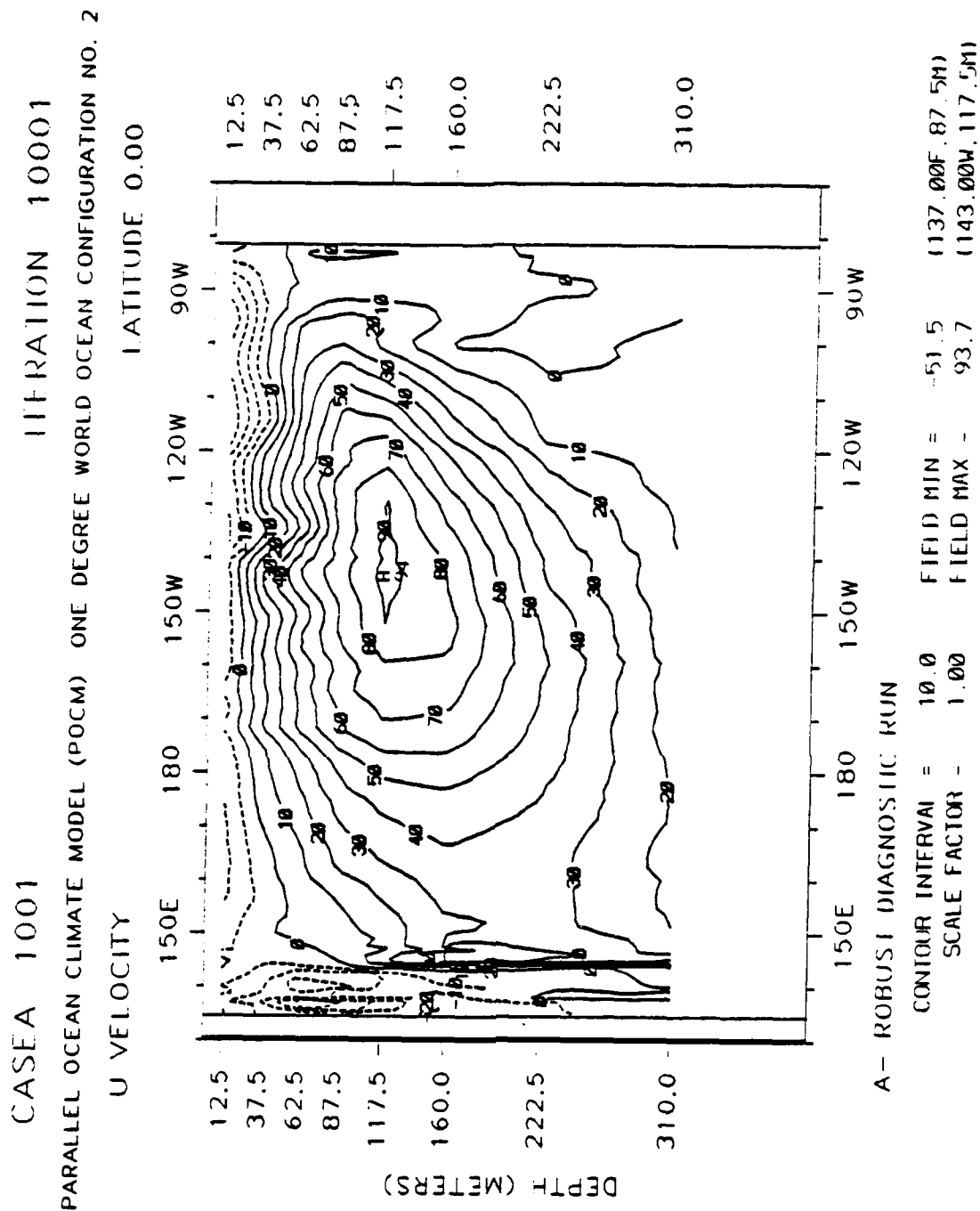


Figure 3.35 Zonal cross-section of zonal velocity in cm s^{-1} at 0.0° latitude in the Pacific Ocean for experiment 1.

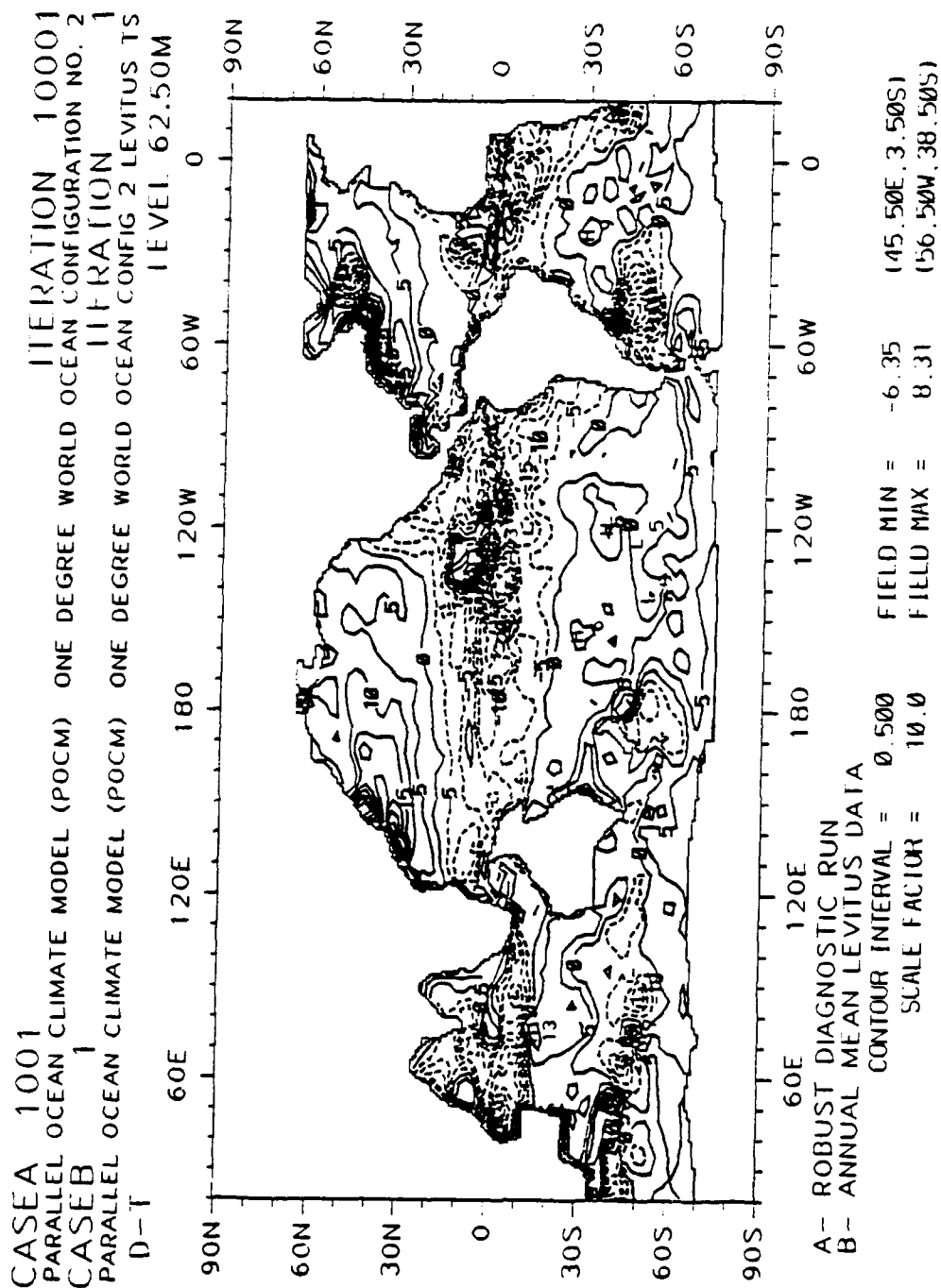


Figure 3.36

Global overview of potential temperature difference (experiment 1 results minus annual mean Levitus data) in units of 0.1°C at 62.5 m depth.

AD-A195 760

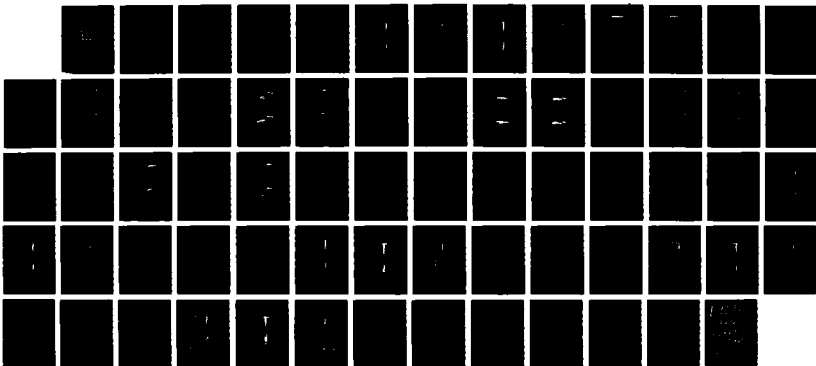
AN ANALYSIS OF RESULTS OF A HIGH-RESOLUTION WORLD OCEAN
CIRCULATION MODEL(U) NAVAL POSTGRADUATE SCHOOL MONTEREY
CA W A BARTON MAR 89

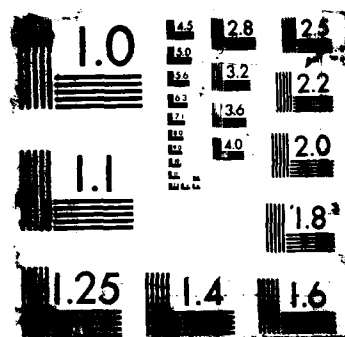
2/2

UNCLASSIFIED

F/G 8/3

NL





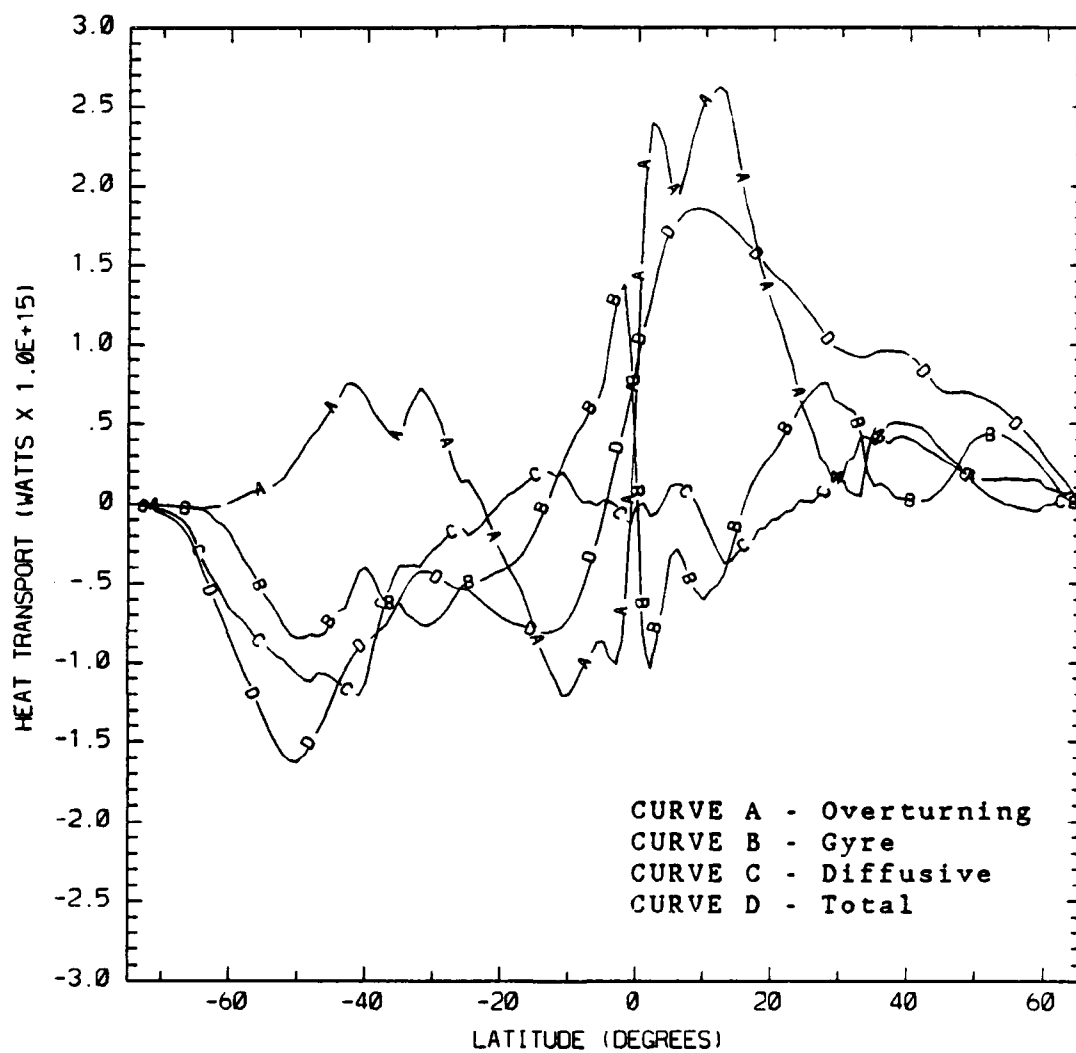


Figure 3.37 Global meridional heat transport for experiment 1 (positive values northward; negative values southward).

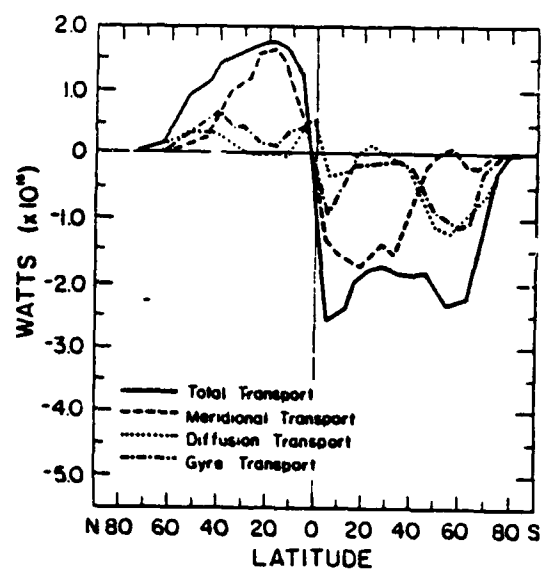
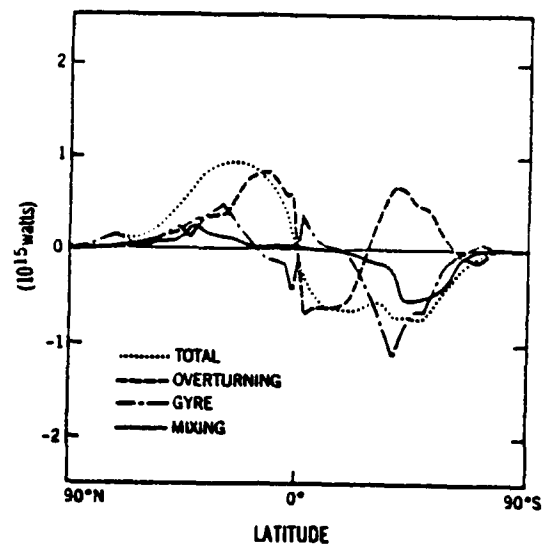


Figure 3.38 Same as Figure 3.37 only from (a) Bryan and Lewis (1979) and (b) Meehl *et al.* (1982).

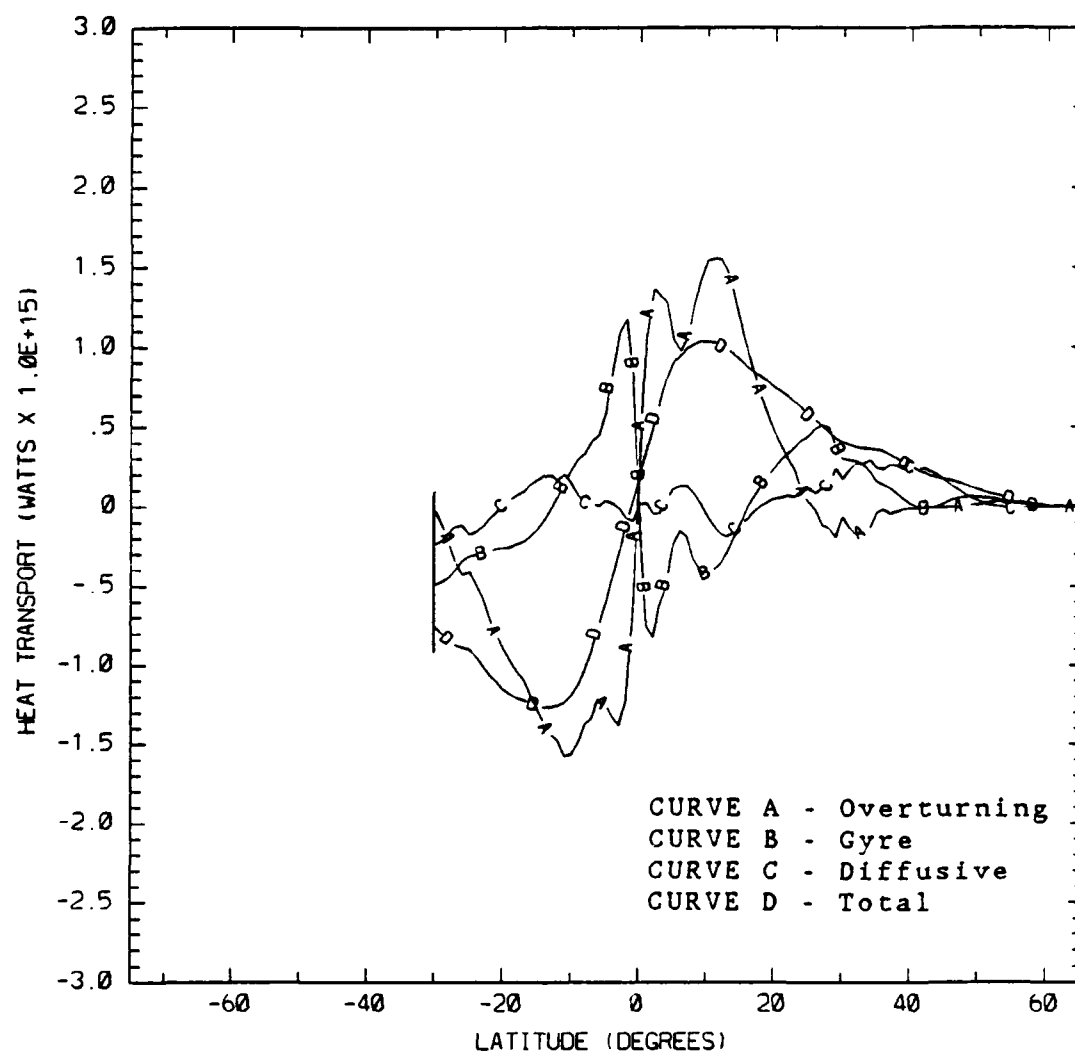


Figure 3.39 Indian-Pacific meridional heat transport for experiment 1 (positive values northward; negative values southward).

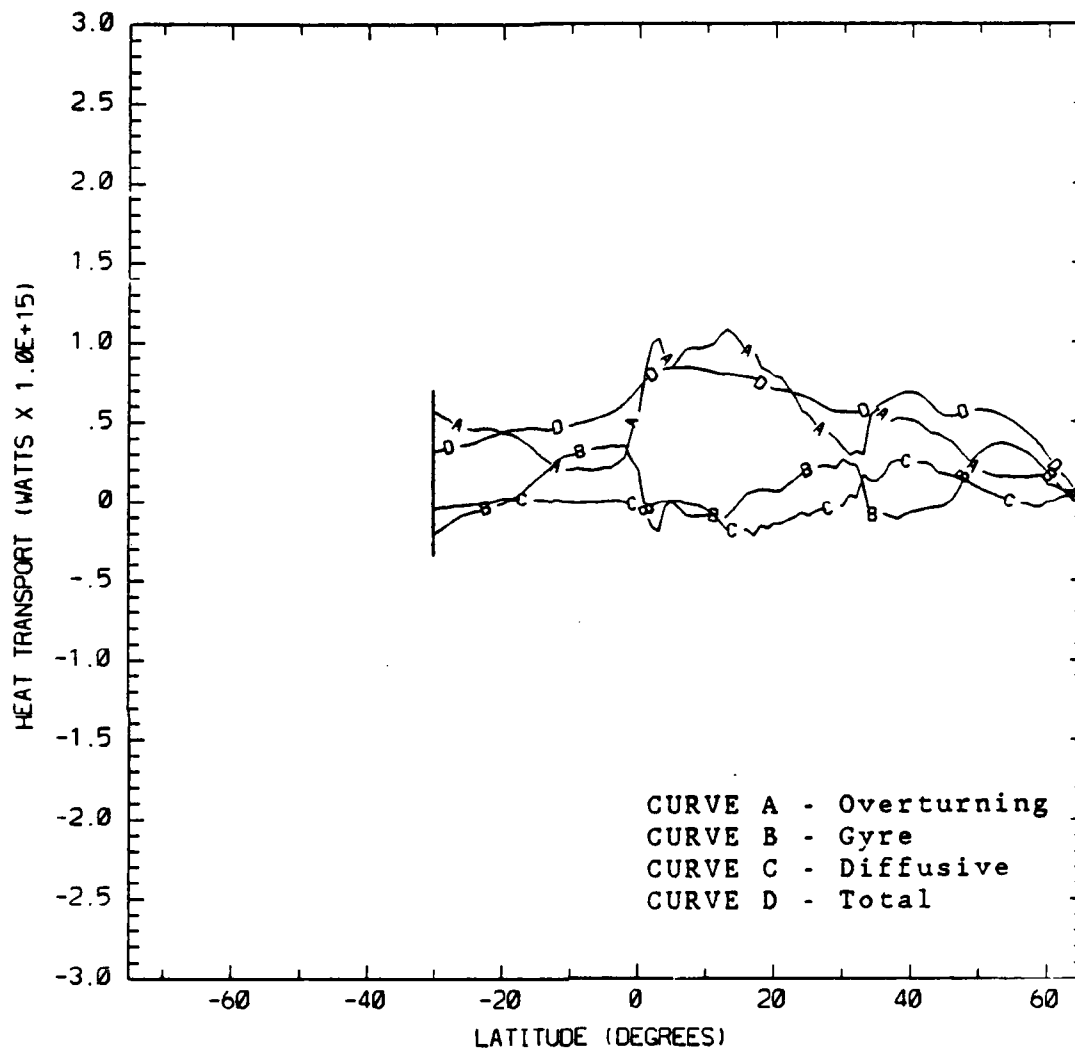


Figure 3.40 Atlantic meridional heat transport for experiment 1 (positive values northward; negative values southward).

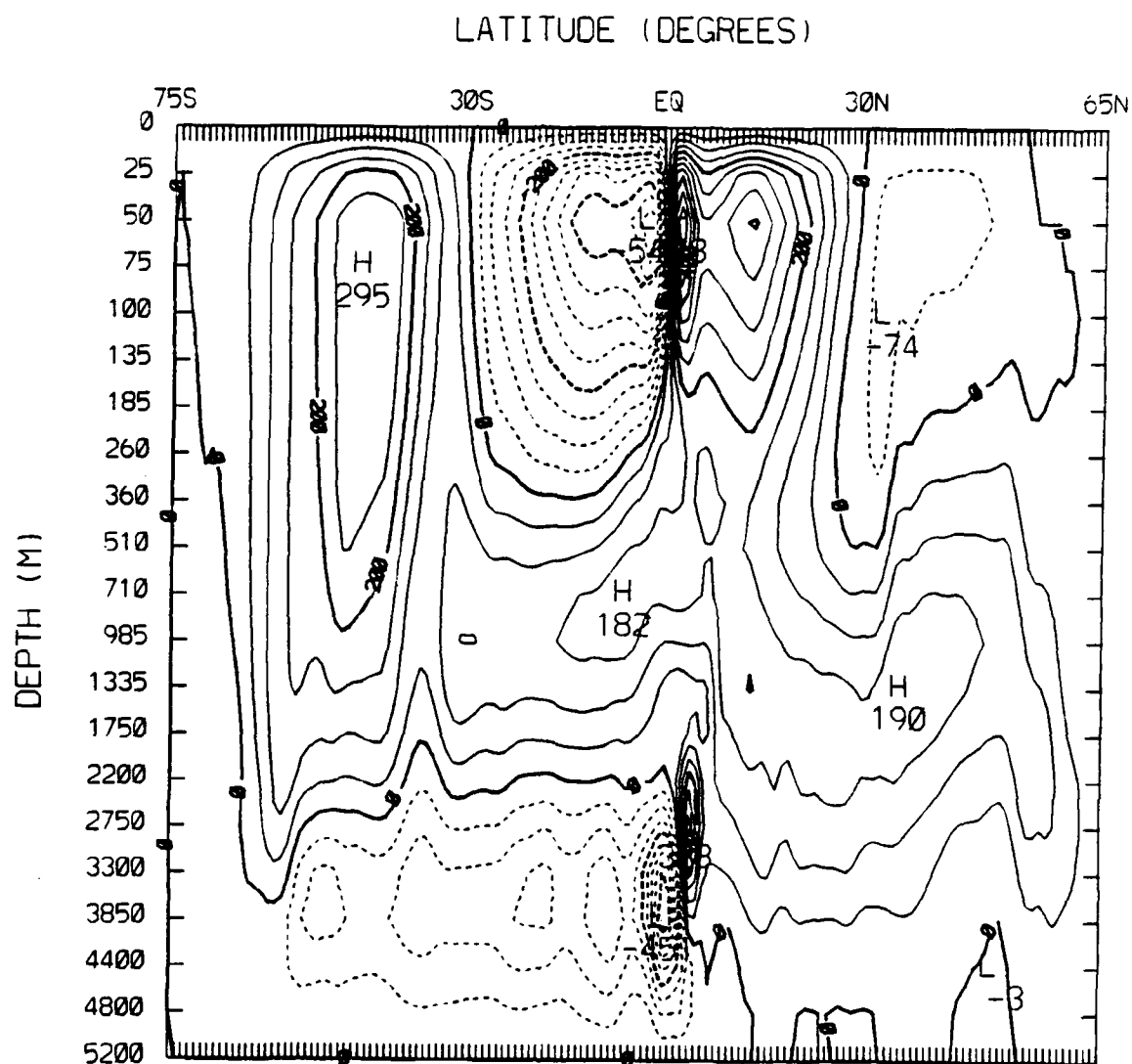


Figure 3.41 Global meridional volume transport in units of $10^{11} \text{ cm}^3 \text{ s}^{-1}$ for experiment 1 (positive values clockwise; negative values counterclockwise).

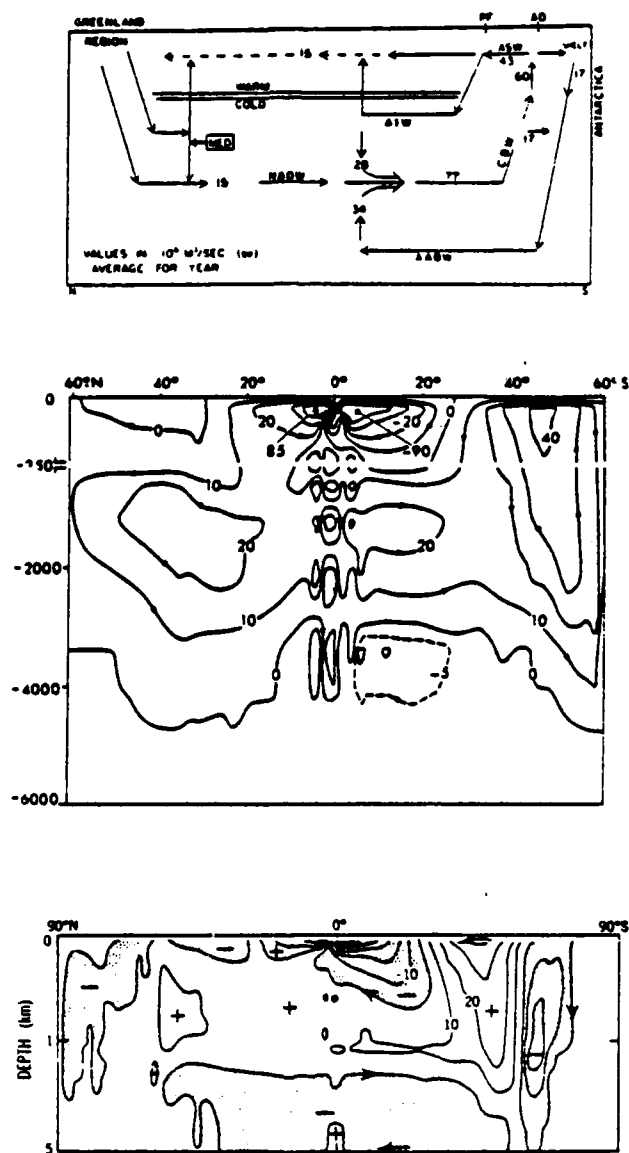


Figure 3.42 Same as Figure 3.41 only in units of $10^{12} \text{ cm}^3 \text{ s}^{-1}$ for (a) observed values of Gordon (1971), (b) modeled values of Cox (1975), and (c) modeled values of Bryan and Lewis (1979).

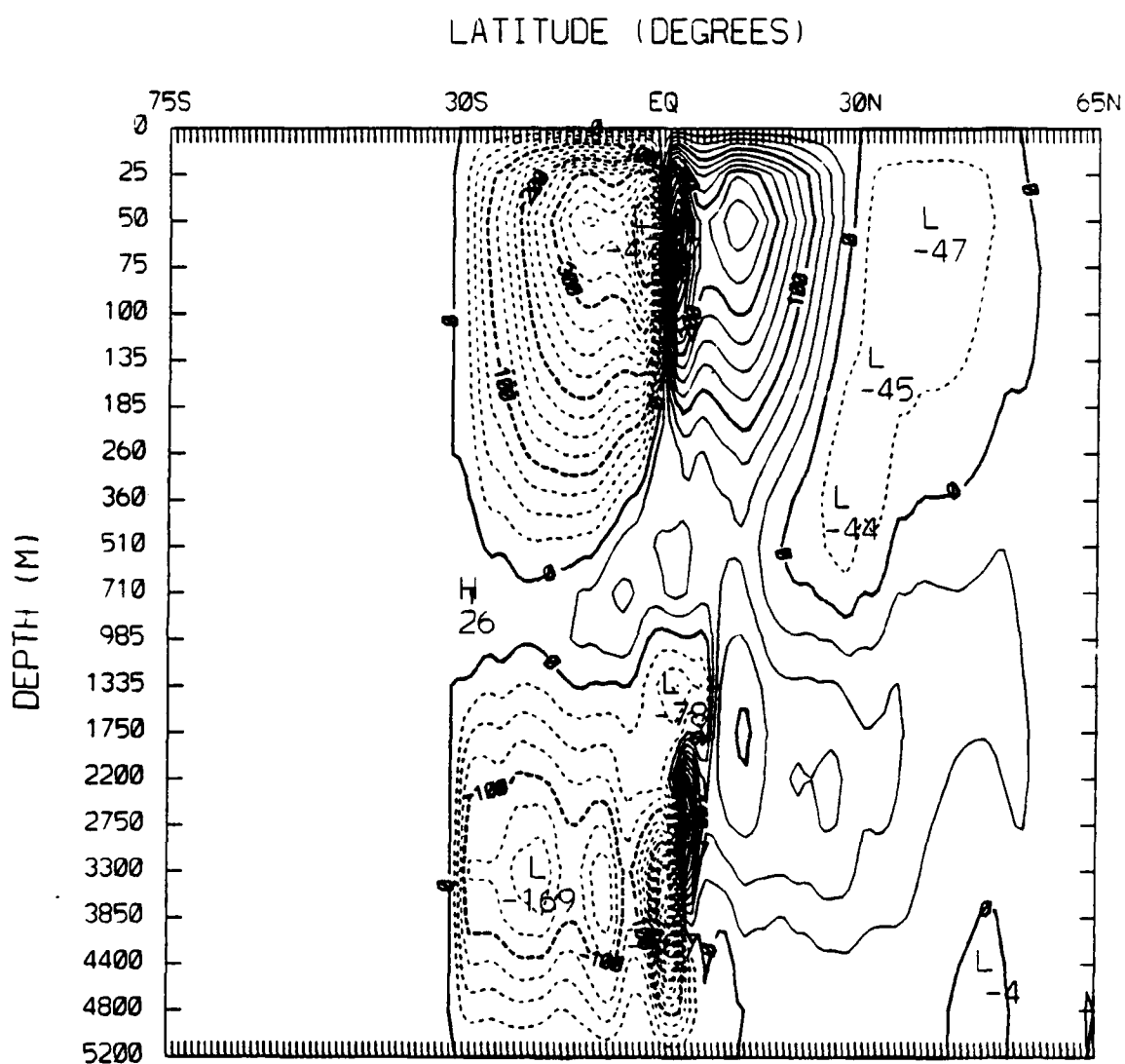


Figure 3.43 Indian-Pacific meridional volume transport in units of $10^{11} \text{ cm}^3 \text{ s}^{-1}$ for experiment 1 (positive values clockwise; negative values counterclockwise).

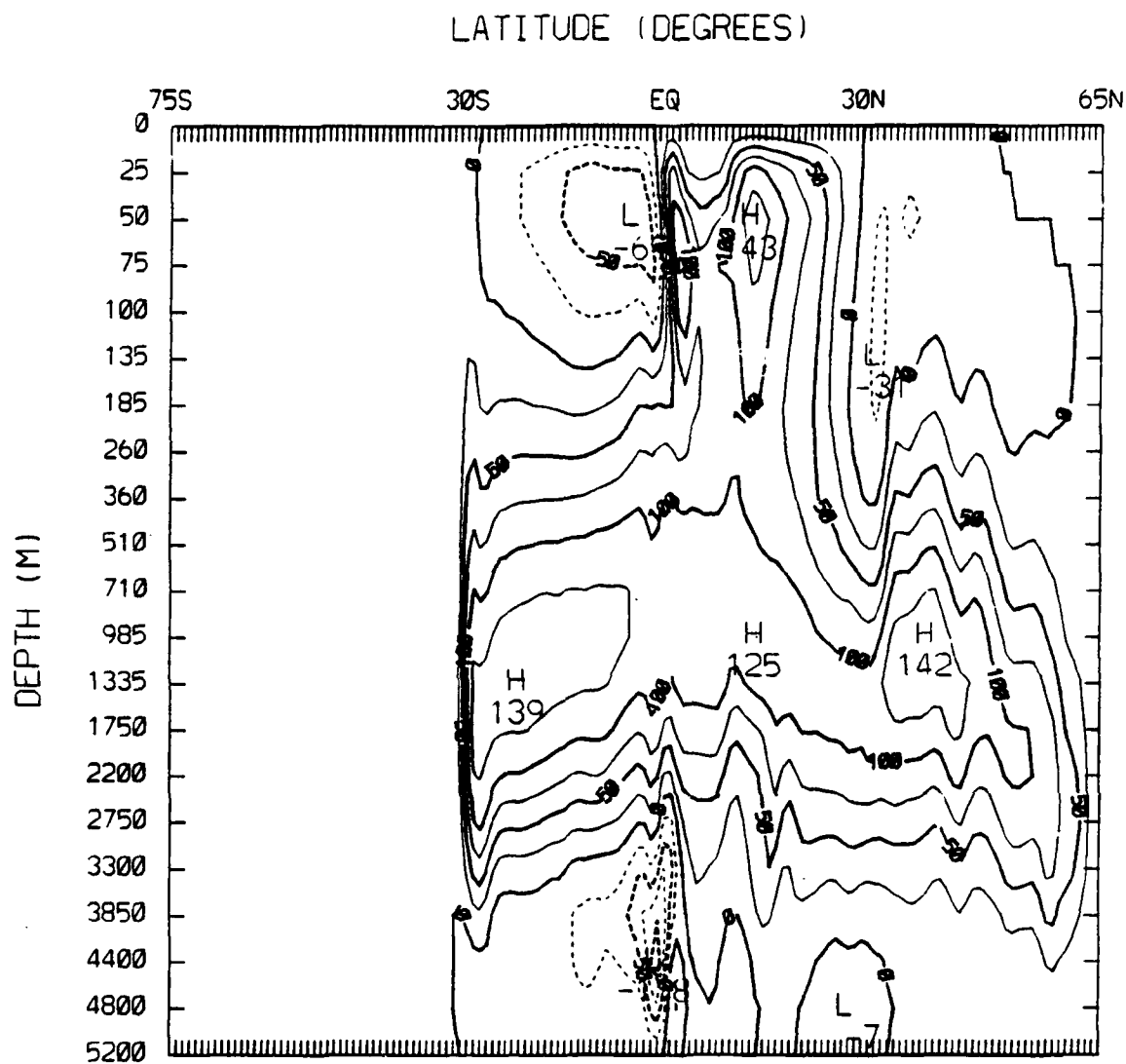


Figure 3.44 Atlantic meridional volume transport in units of $10^{11} \text{ cm}^3 \text{ s}^{-1}$ for experiment 1 (positive values clockwise; negative values counterclockwise).

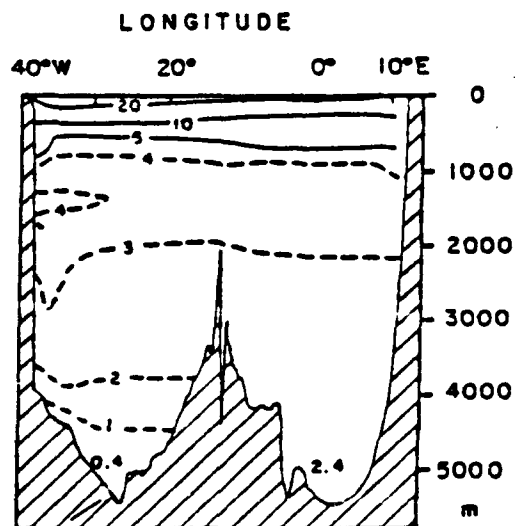
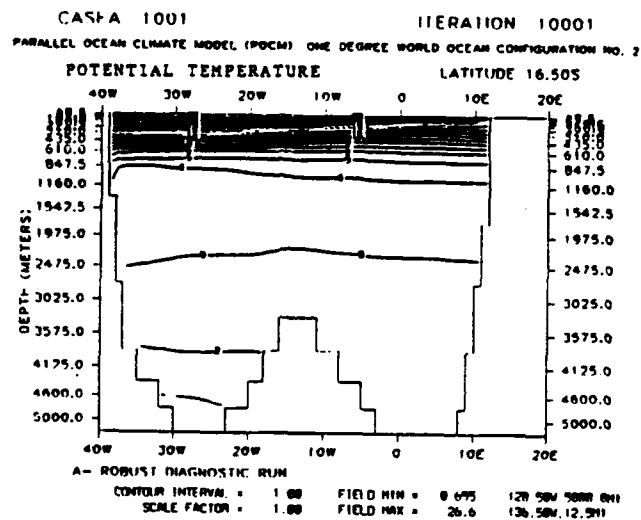


Figure 3.45 Zonal cross-section near 16°S latitude in the Atlantic Ocean of (a) potential temperature in °C for experiment 1 and (b) observed temperature in °C (from Pickard and Emery, 1982).

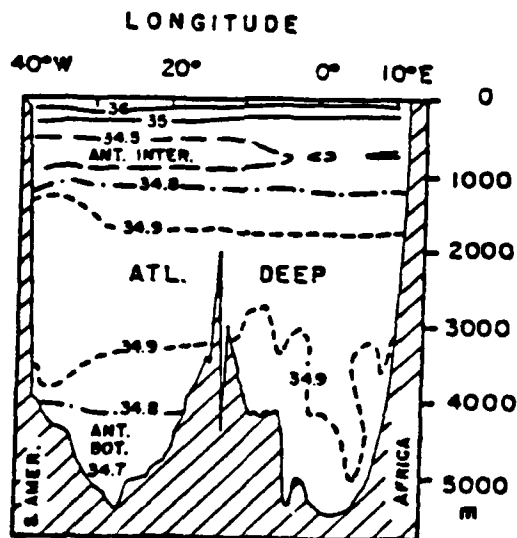
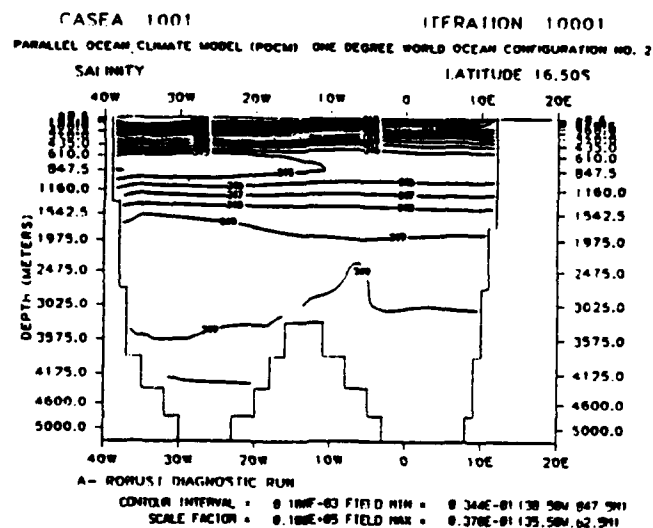


Figure 3.46

Zonal cross-section near 16°S latitude in the Atlantic Ocean of (a) salinity in units of 0.1 PPT for experiment 1 and (b) observed salinity in PPT (from Pickard and Emery, 1982).

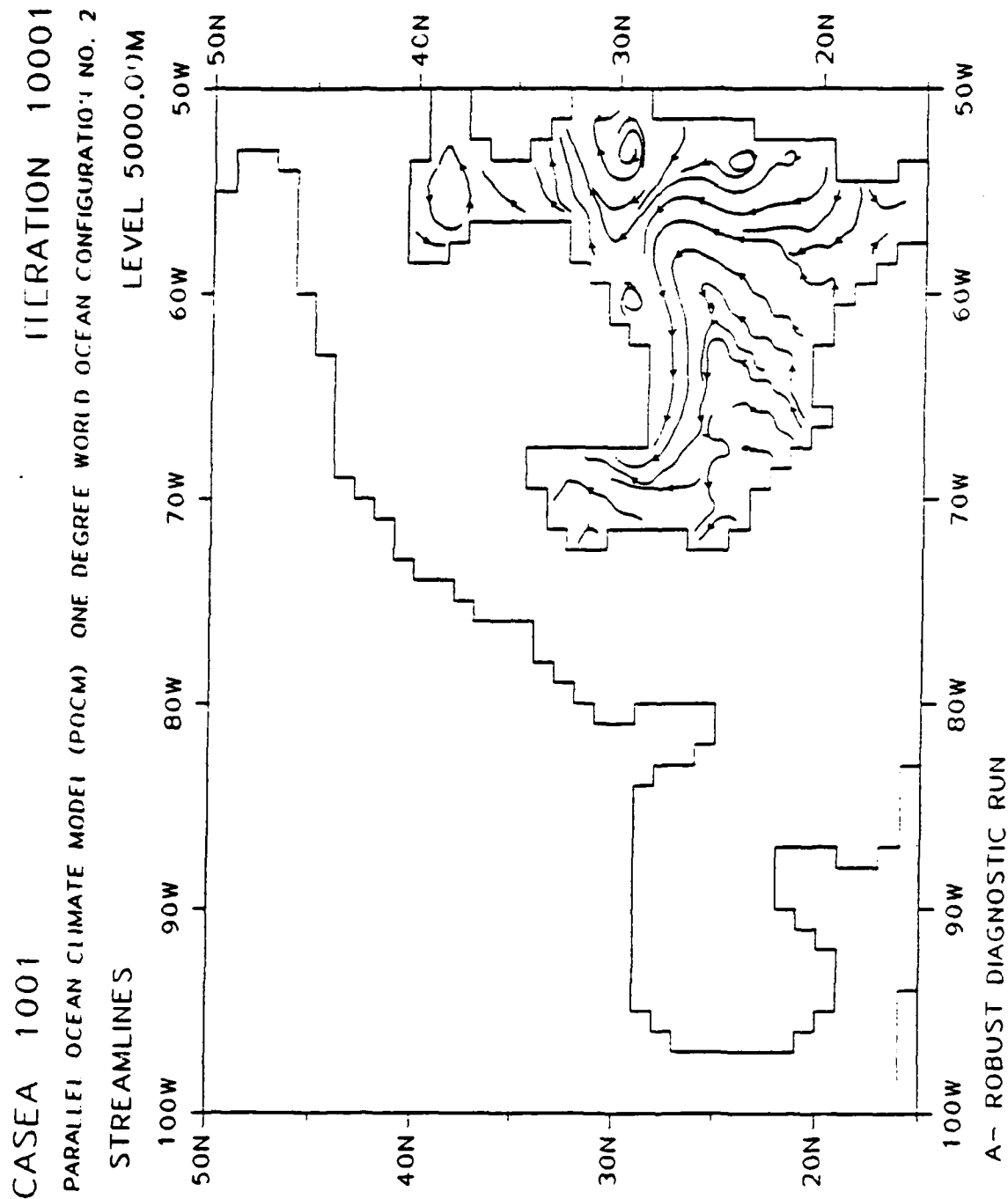


Figure 3.47

Streamlines at 5000.0 depth in the Gulf Stream region for experiment 1. Streamlines are everywhere tangent to the current vectors and are selectively originated/discontinued to maintain near-uniform spacing.

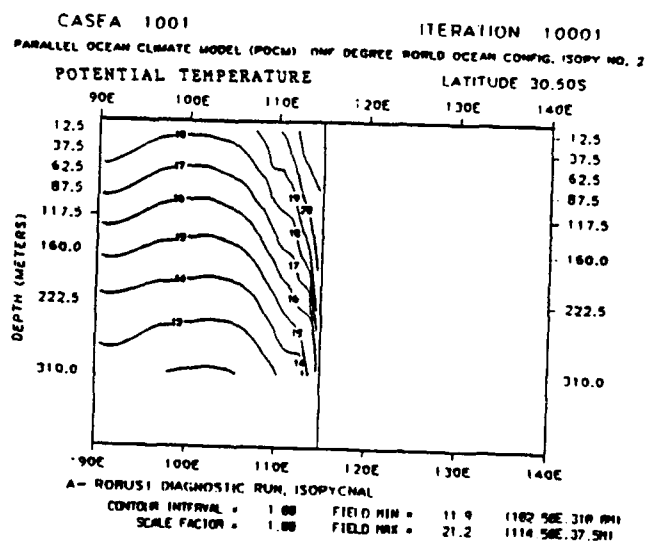
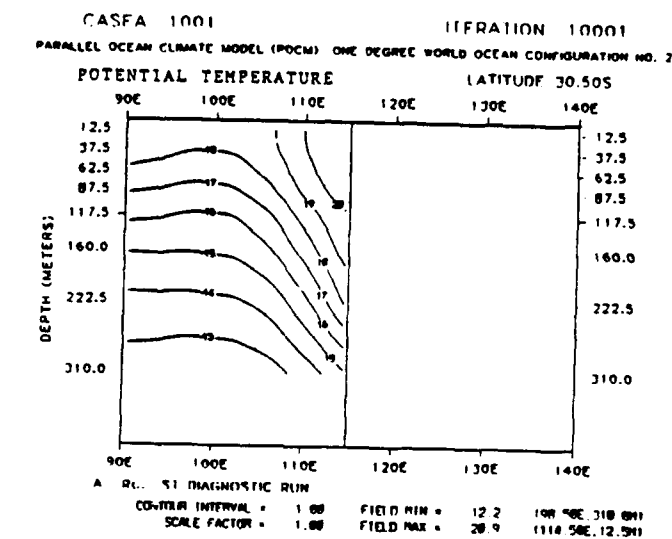


Figure 3.48 Zonal cross-section of potential temperature in °C at 30.5°S latitude off of western Australia (a) for experiment 1 and (b) for experiment 2.

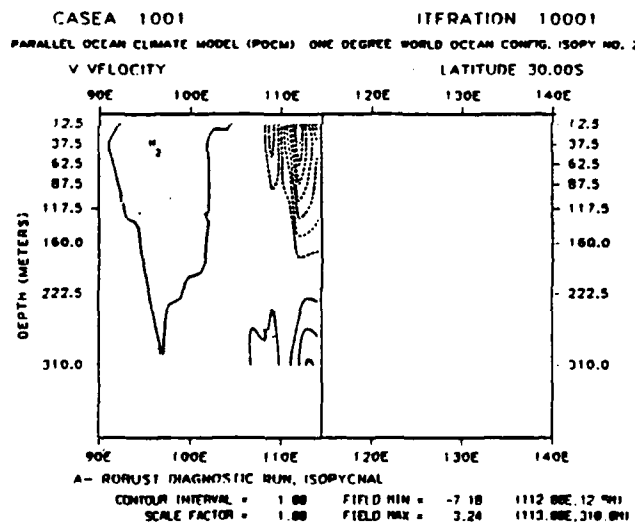
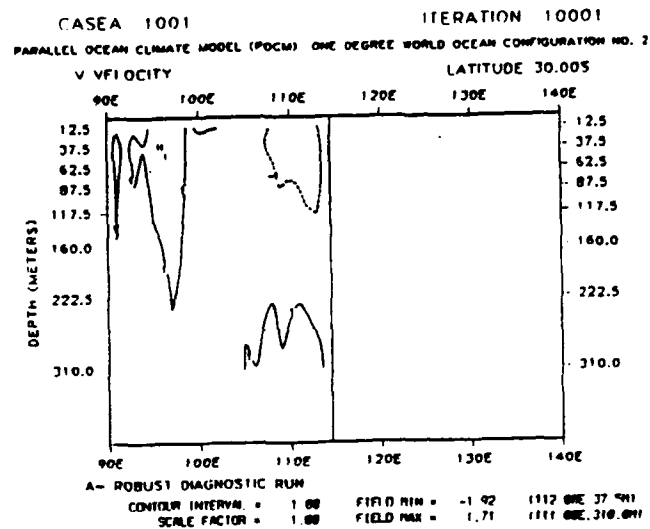


Figure 3.49 Zonal cross-section of meridional velocity in cm s^{-1} at 30.0°S latitude off of western Australia (a) for experiment 1 and (b) for experiment 2.

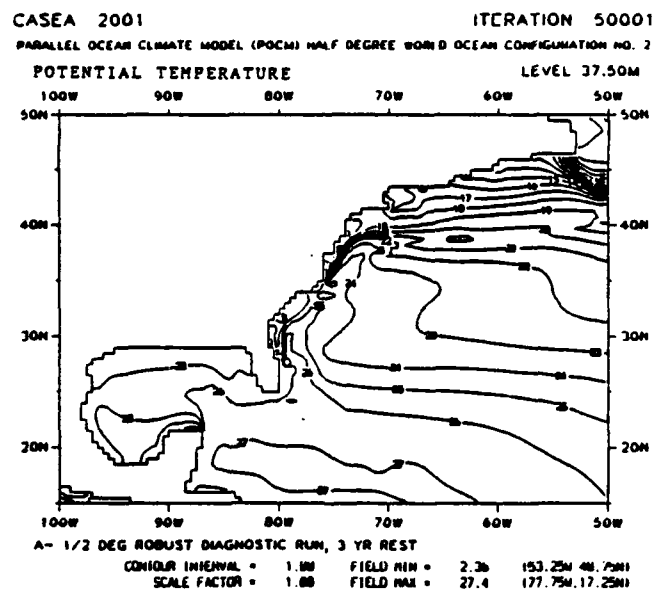
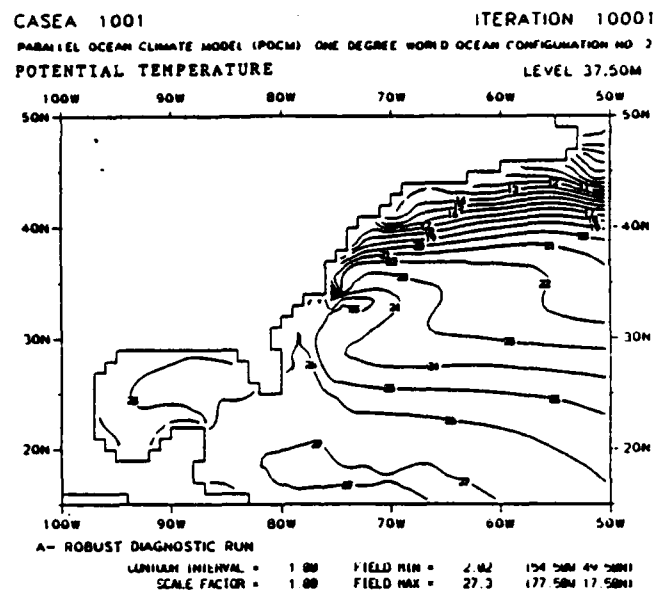


Figure 3.50 Potential temperature in $^{\circ}\text{C}$ at 37.5 m depth in the Gulf Stream region (a) for experiment 1 and (b) for experiment 3.

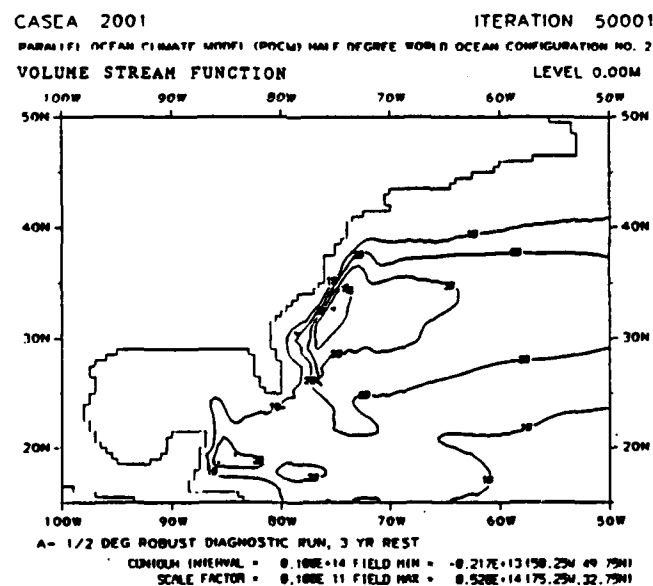
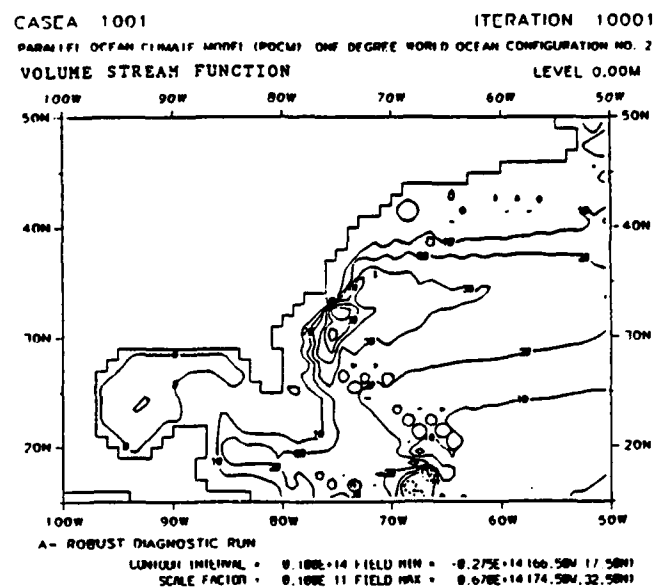


Figure 3.51 Horizontal volume transport in $Sv (=10^{12} \text{ cm}^3 \text{ s}^{-1})$ in the Gulf Stream region (a) for experiment 1 and (b) for experiment 3.

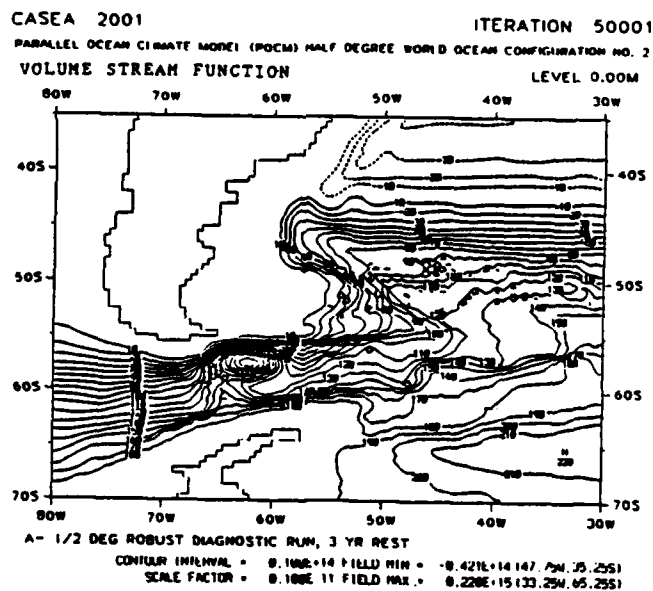
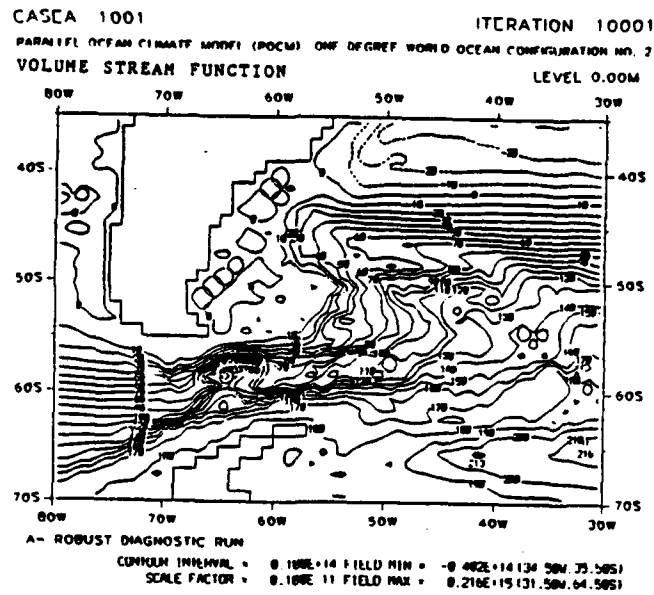


Figure 3.53 Horizontal volume transport in $\text{Sv} (=10^{12} \text{ cm}^3 \text{ s}^{-1})$ in the Drake Passage region (a) for experiment 1 and (b) for experiment 3.

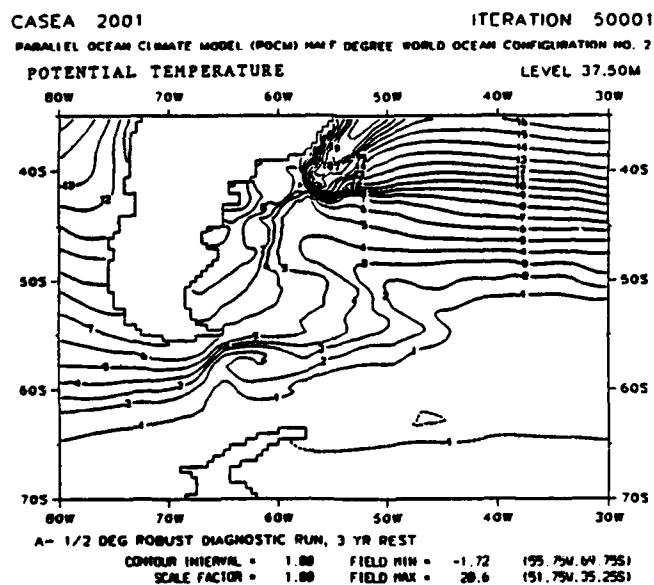
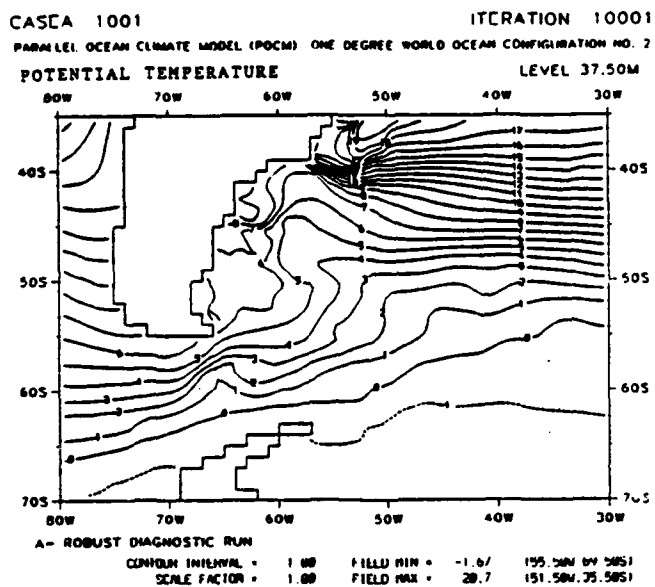


Figure 3.54 Potential temperature in $^{\circ}\text{C}$ at 37.5 m depth in the Drake Passage region (a) for experiment 1 and (b) for experiment 3.

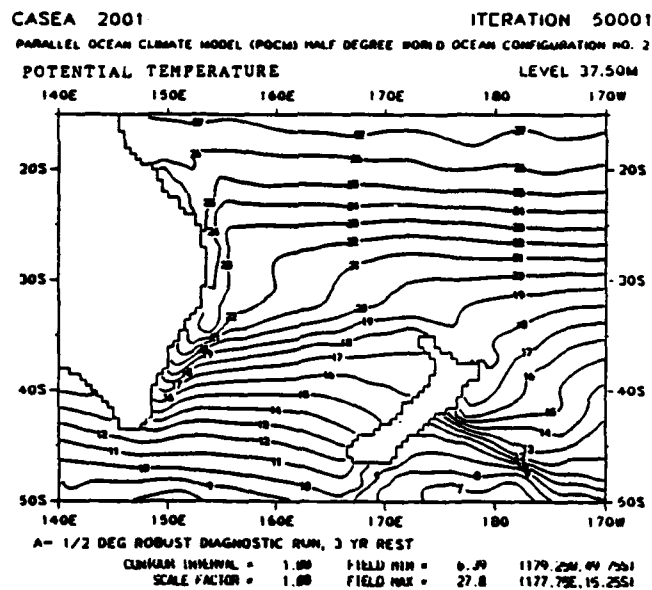
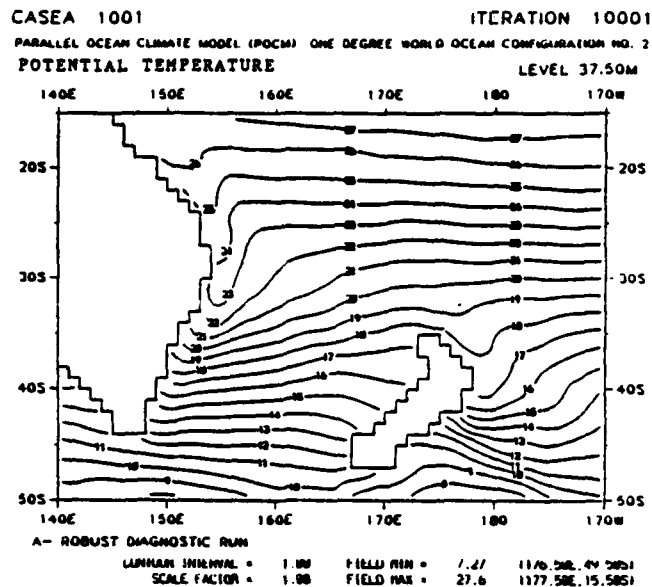


Figure 3.56 Potential temperature in °C at 37.5 m depth in the East Australian Current region (a) for experiment 1 and (b) for experiment 3.

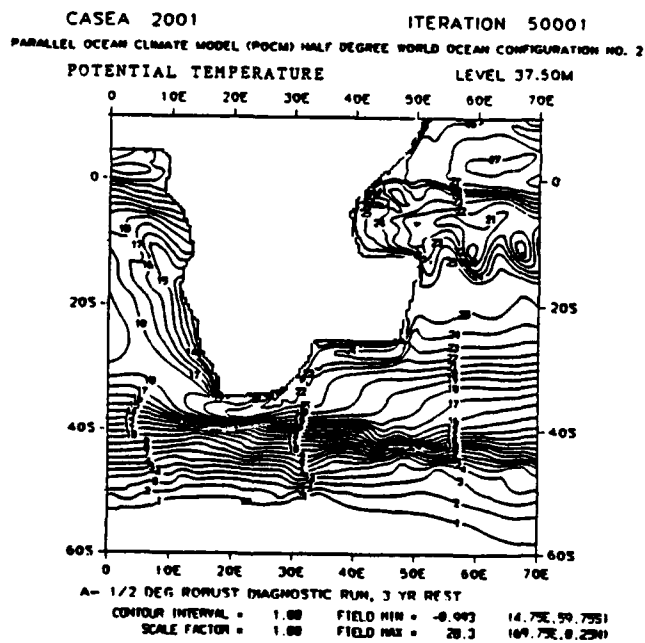
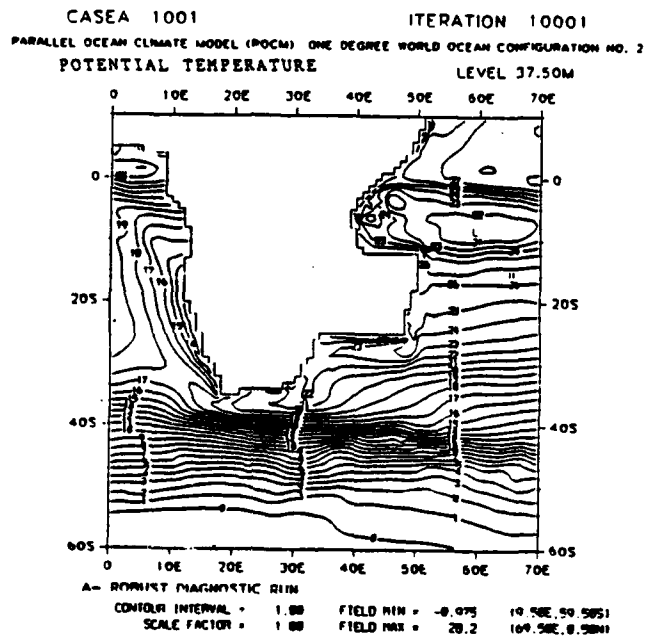


Figure 3.57 Potential temperature in °C at 37.5 m depth in the Agulhas Current region (a) for experiment 1 and (b) for experiment 3.

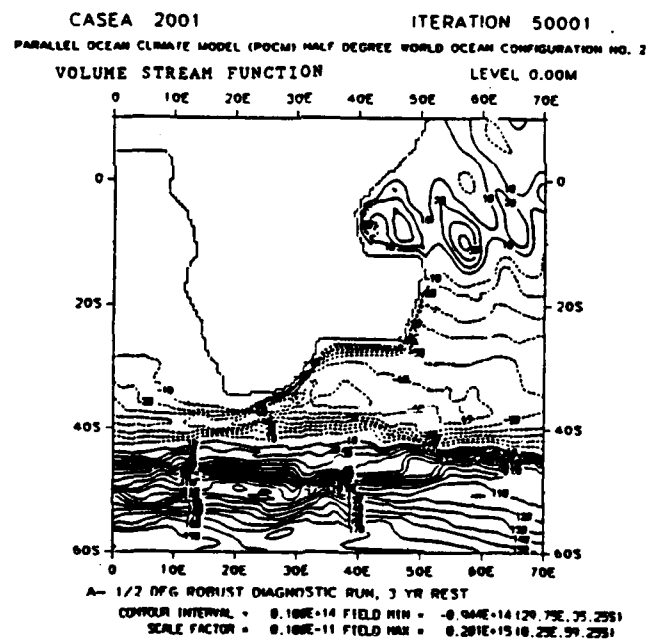
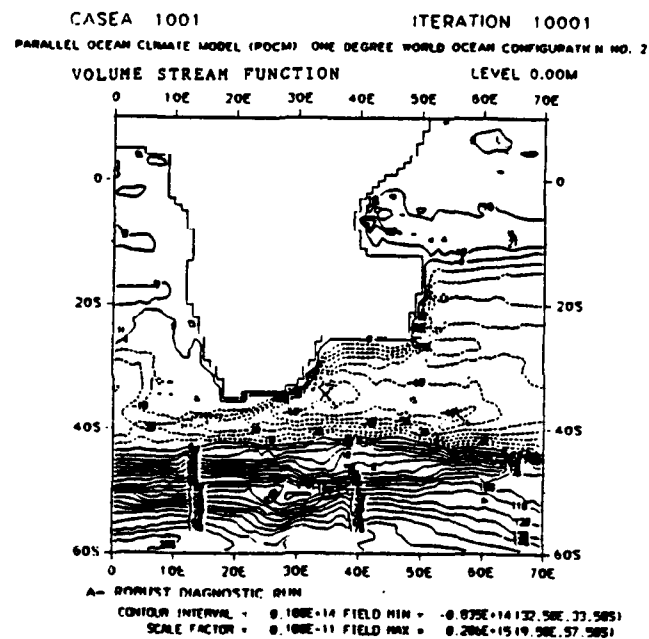


Figure 3.58 Horizontal volume transport in $Sv (=10^{12} \text{ cm}^3 \text{ s}^{-1})$ in the Agulhas Current region (a) for experiment 1 and (b) for experiment 3.

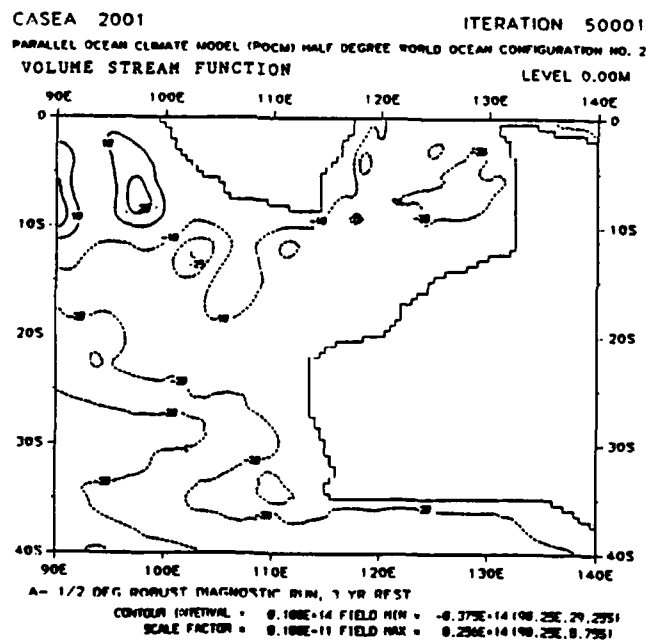
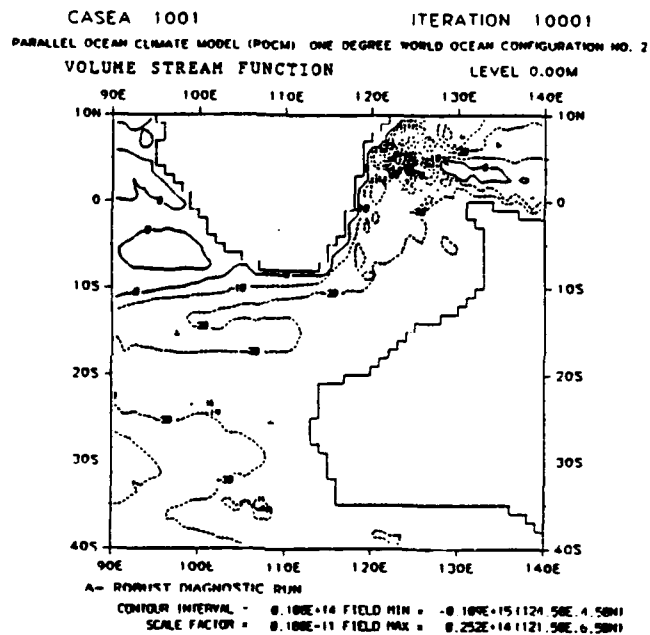


Figure 3.59 Horizontal volume transport in $\text{Sv} (=10^{12} \text{ cm}^3 \text{ s}^{-1})$ in the western Australia region (a) for experiment 1 and (b) for experiment 3.

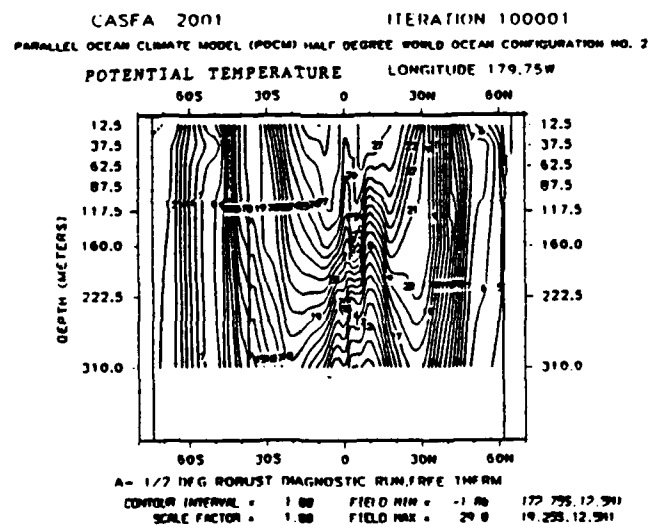
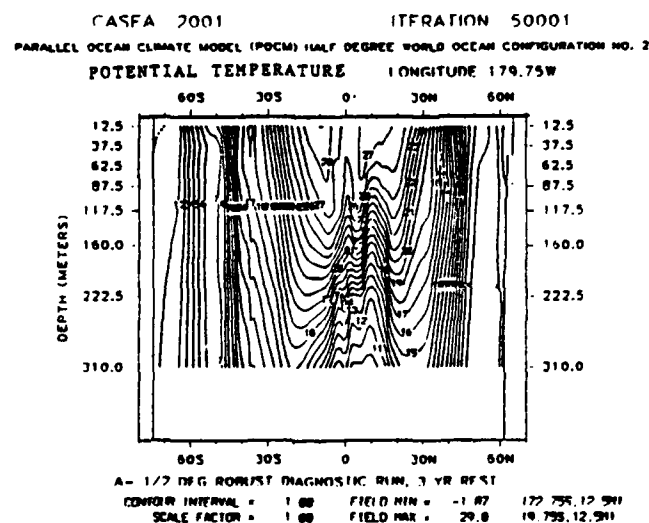


Figure 3.61 Meridional cross-section of potential temperature in $^{\circ}\text{C}$ at 179.75°W longitude (a) for experiment 3 and (b) for experiment 4.

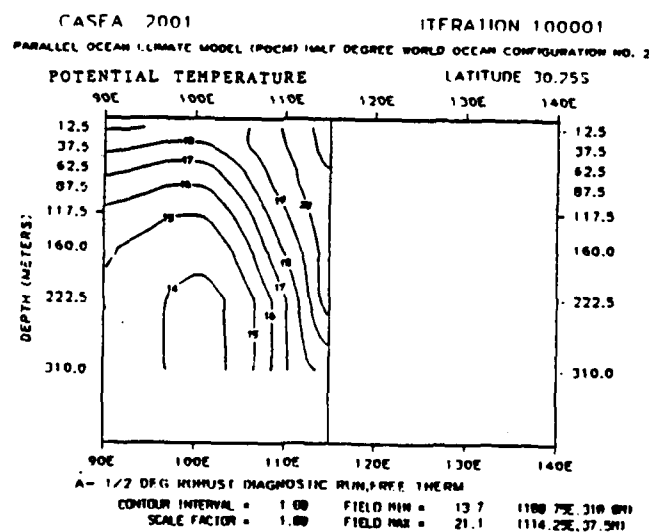
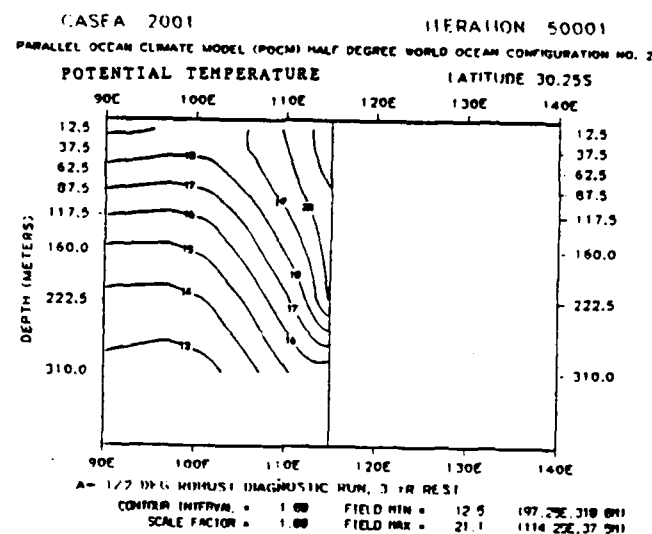


Figure 3.62 Zonal cross-section of potential temperature at 30.25°S latitude off of western Australia in °C (a) for experiment 3 and (b) for experiment 4.

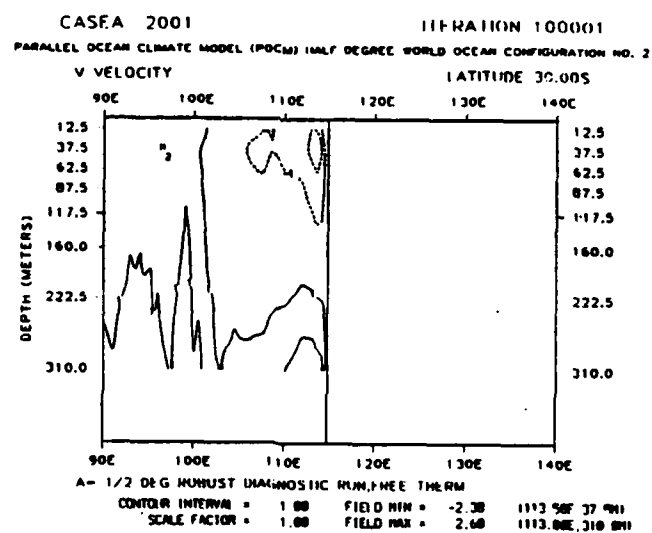
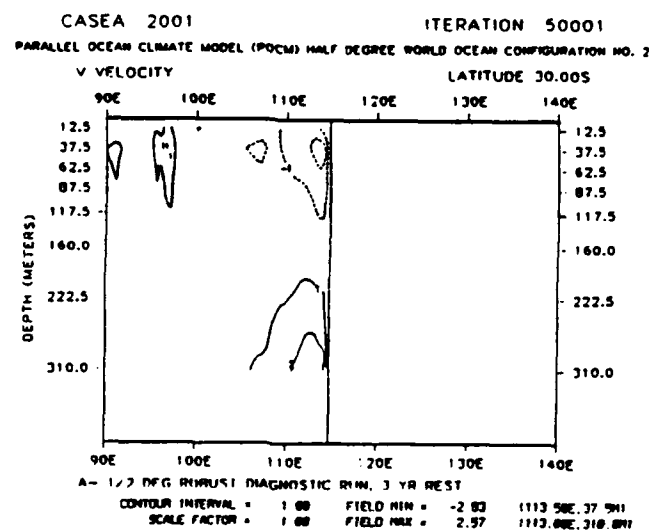


Figure 3.64 Zonal cross-section of meridional velocity in cm s^{-1} at 30.00°S latitude off of western Australia (a) for experiment 3 and (b) for experiment 4.

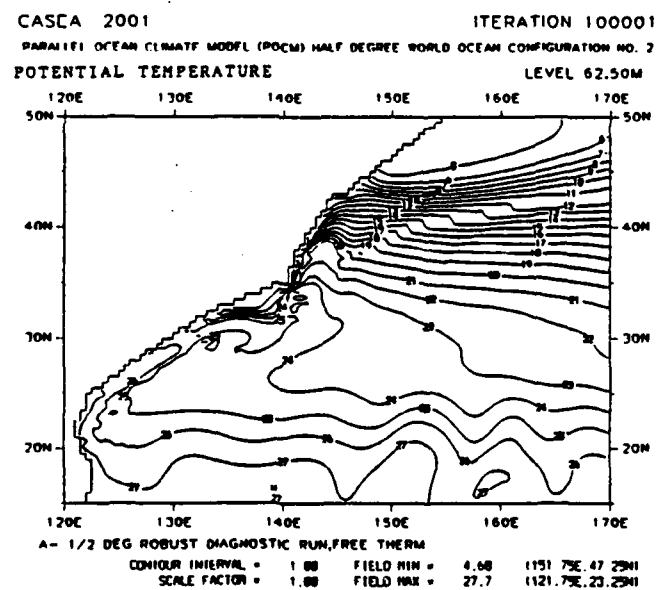
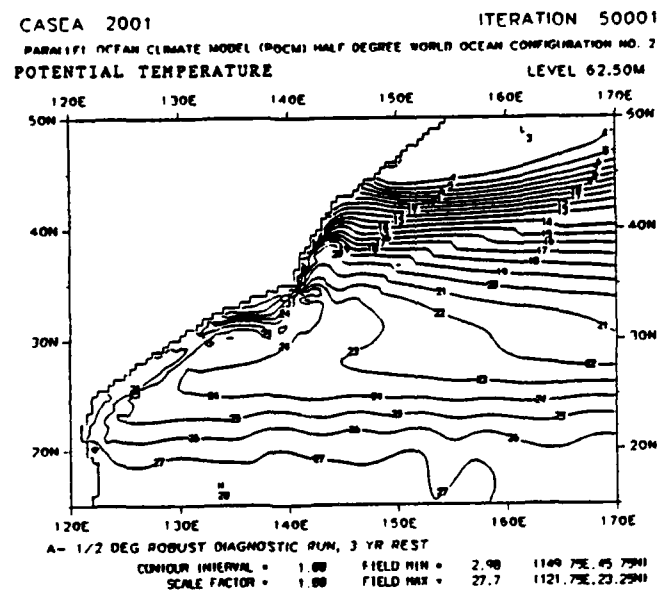


Figure 3.65 Potential temperature in °C at 62.5 m depth in the Kuroshio Current region (a) for experiment 3 and (b) for experiment 4.

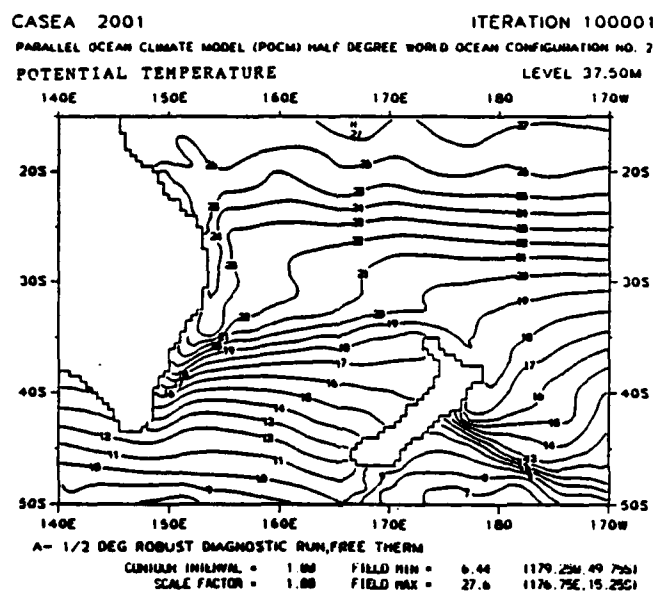
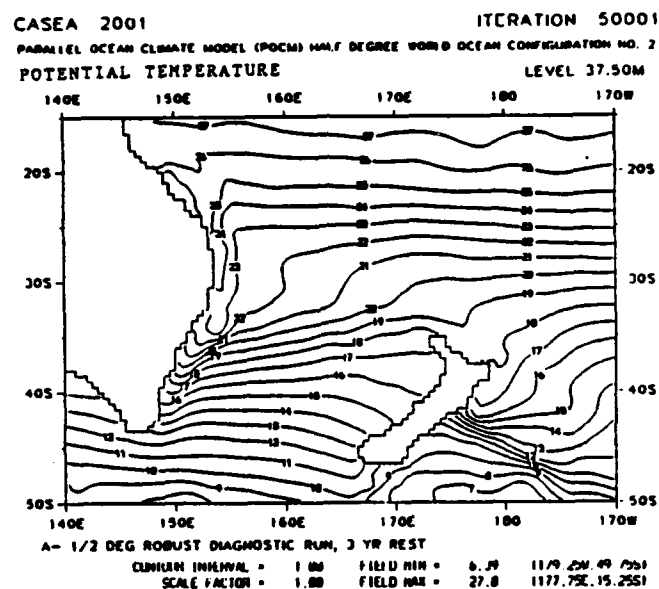


Figure 3.66 Potential temperature in °C at 37.5 m depth in the East Australian Current region (a) for experiment 3 and (b) for experiment 4.

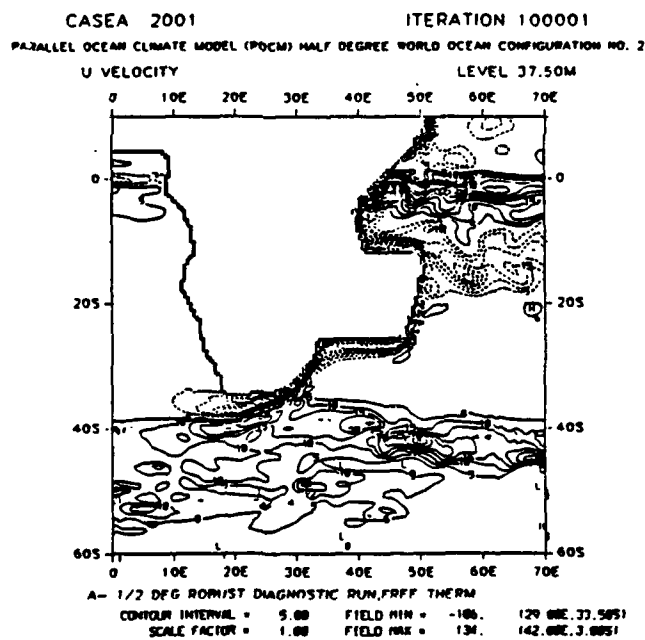
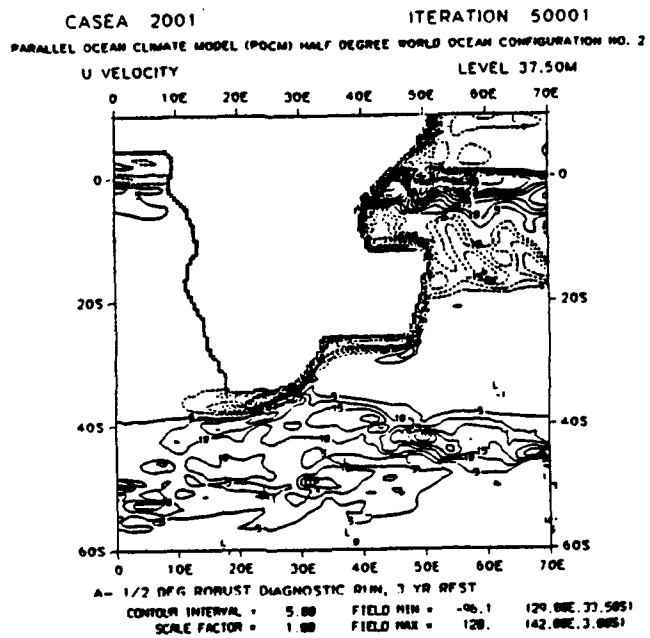


Figure 3

IV. SUMMARY AND CONCLUSIONS

An ocean modeling system now exists that can handle large ocean problems on anticipated supercomputers of the 1990's. Using one degree horizontal resolution; 20 levels of vertical resolution; realistic geometry, forcing, and physics; and a robust-diagnostic strategy the world ocean model of Semtner and Chervin produced results after four years of integration that showed many realistic features of the global ocean circulation. Moreover, meridional heat and volume transports resulting from this model compared well with those of other studies. Some improvement in the modeling of boundary currents using one degree horizontal resolution was realized by a switch to diffusion along isopycnal (versus horizontal) surfaces. Using one-half degree horizontal resolution and a less robust climatological damping of the ocean interior, ten years of integration of the world ocean model of Semtner and Chervin produced an even more realistic representation of global ocean circulation. Frontal regions and subtropical instabilities that were not (or were only barely) evident in the one degree experiments became much stronger and much more clearly defined. Meridional heat transport results appeared to benefit from a reduced horizontal eddy diffusivity and from less climatological damping of the ocean interior. Experimentation with a "free thermocline" (after Sarmiento and Bryan, 1982) produced only minor changes in the results obtained using a three year damping time constant -- suggesting that the physics of the world ocean model are

largely unrestrained in the upper water column by the robust-diagnostic terms. The additional ten years of model integration afforded by this experiment also demonstrated the intensification of subtropical instabilities already identified in the earlier half-degree experiment. These realistic high-resolution integrations have been made possible by employing an ocean model code that is both fully vectorized and designed for "multitasking" on as many processors as the latest supercomputer technology can afford.

There are many potential applications of this ocean modeling system. Already demonstrated using the world ocean model are an anomalous northward heat transport in the South Atlantic, a possibly related westward flow around the southern tip of Africa, a westward flowing Gulf Stream undercurrent, an anticyclonic turn of the East Australian Current near the southern tip of Australia, and the suppression of upwelling by a southward flowing current along the western coast of Australia. An ongoing half-degree simulation employing biharmonic mixing is revealing meanders and pinched-off rings in the major western boundary currents. A future simulation using one-third degree horizontal resolution will be fully eddy-resolving. Without this additional resolution, however, the realistic meridional heat and volume transports produced by the world ocean model already nominate it for coupling to global atmospheric models in climate studies. Moreover, the ocean model system used in this world ocean analysis can also be used for high-resolution regional studies. Such a simulation employing an open boundary condition between the

world ocean and the tropical ocean has already been successfully tested.

The future of this ocean modeling system is bright. With the supercomputers likely to be available in the early 1990's, fully prognostic modeling with one-sixth degree horizontal resolution and 40 levels of vertical resolution should be achievable. From a Navy standpoint, three things must be accomplished before this ocean modeling system can be employed for deterministic forecasting of ocean currents, fronts, meanders, and eddies on a real-time basis. First, the model's simulation of the Gulf Stream must be improved. Experimentation conducted in this study suggest that mass exchange between the North Atlantic and Arctic Oceans may be important when modeling the Gulf Stream. Plans have already been made to map the Arctic Ocean grid into the unused data arrays of the primary continent and then to couple the Arctic grid to the North Atlantic at 65°N latitude. Second, the Navy must provide state-of-the-art supercomputers with multiple processors and fast vector startup times. Acquisition of such a supercomputer is already being considered for the Naval Oceanographic Office in Bay St. Louis, Mississippi and for the Fleet Numerical Oceanography Center in Monterey, California. Third, a data assimilation system is needed that can provide accurate real-time forcing of the ocean model for the region of interest. Such a data assimilation system is certainly within reach given the technology of 1988. It is the author's opinion that submarine and anti-submarine warfare of the 1990's will require forecasting of the

world ocean circulation as only this ocean modeling system can provide.

APPENDIX: MERIDIONAL HEAT AND VOLUME TRANSPORT PLOTS

Enclosed are plots of meridional heat transport and meridional volume transport for the global, Indian-Pacific, and Atlantic ocean basins for each of the four experiments analyzed in this study.

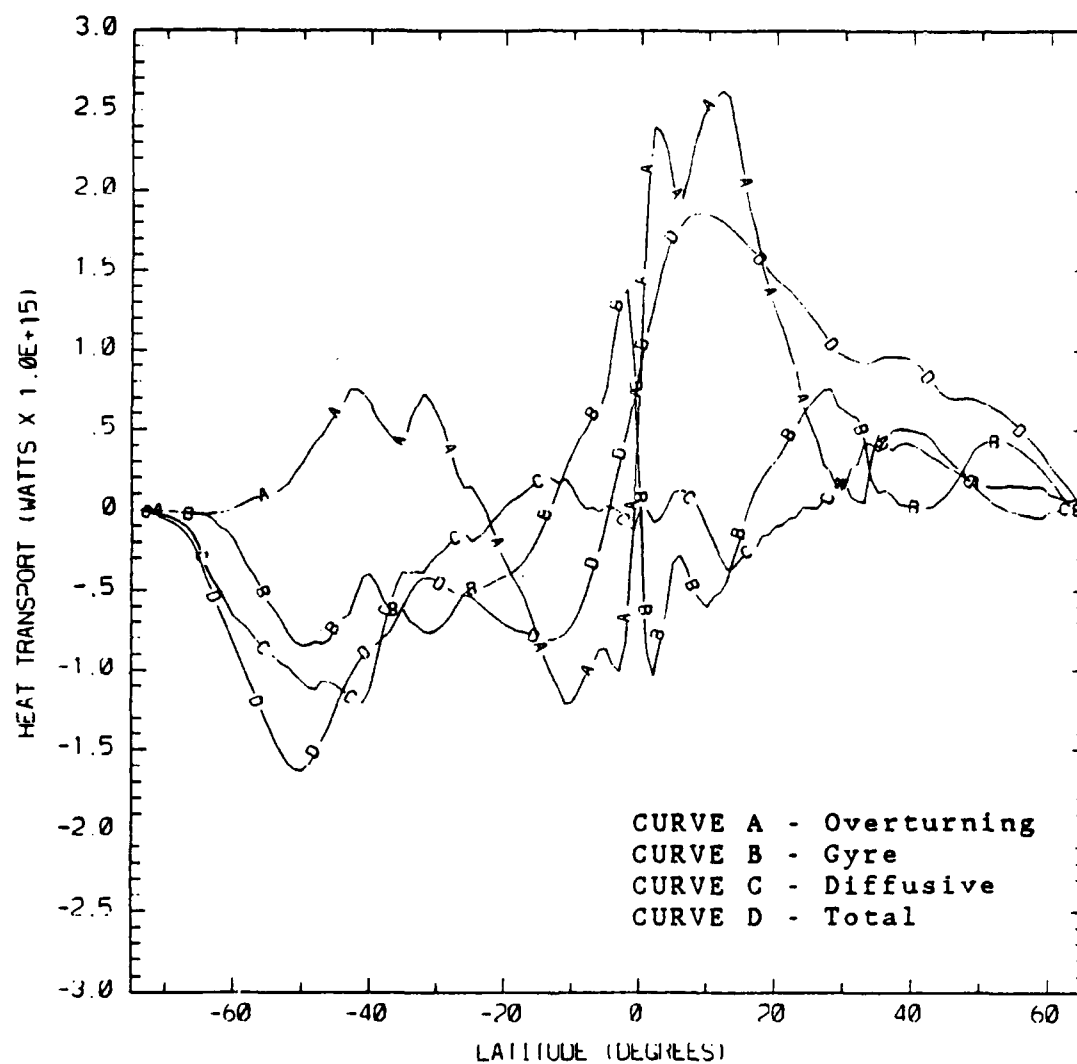


Figure A.1 Global meridional heat transport for experiment 1 (positive values northward; negative values southward).

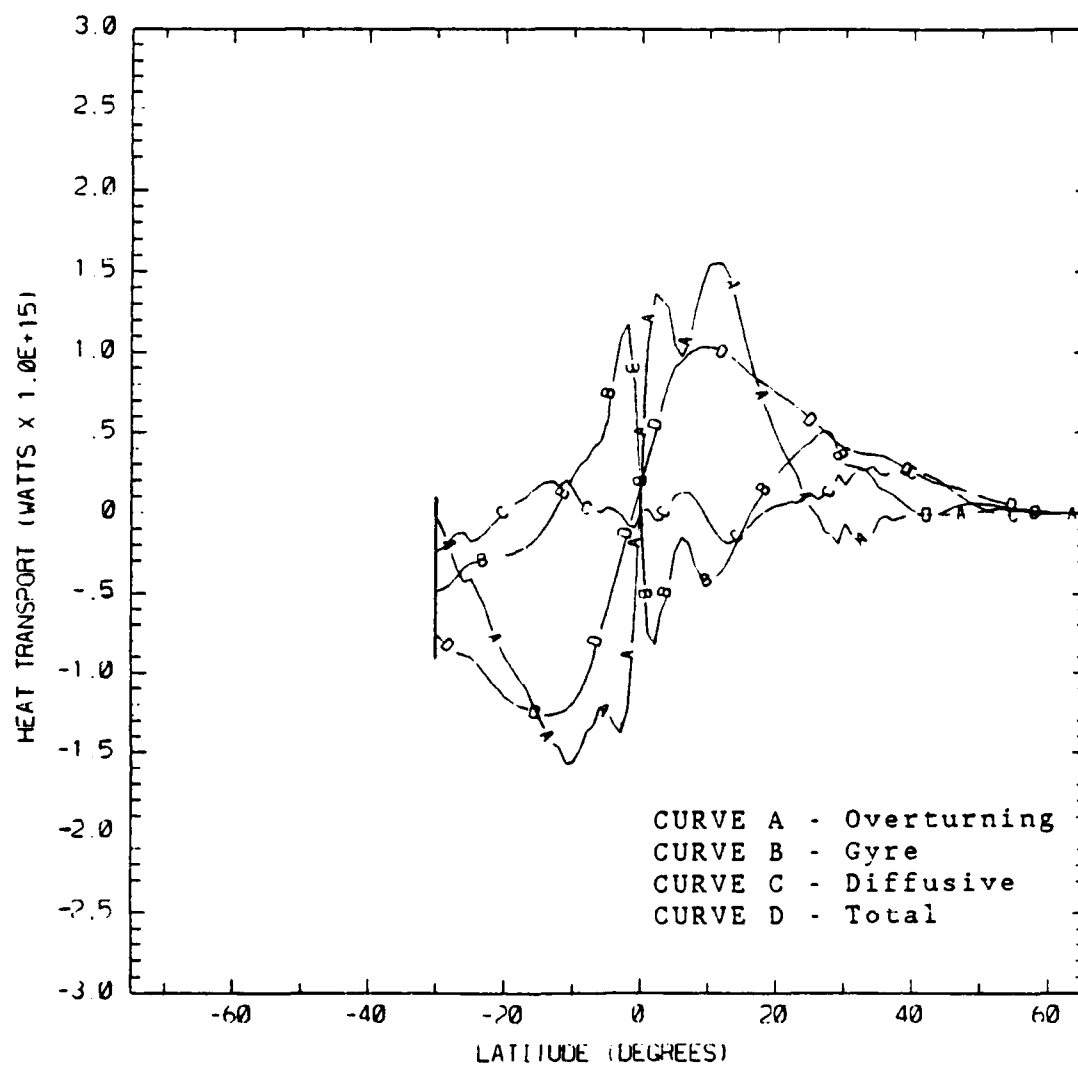


Figure A.2 Same as Figure A.1 but for Indian-Pacific ocean basin.

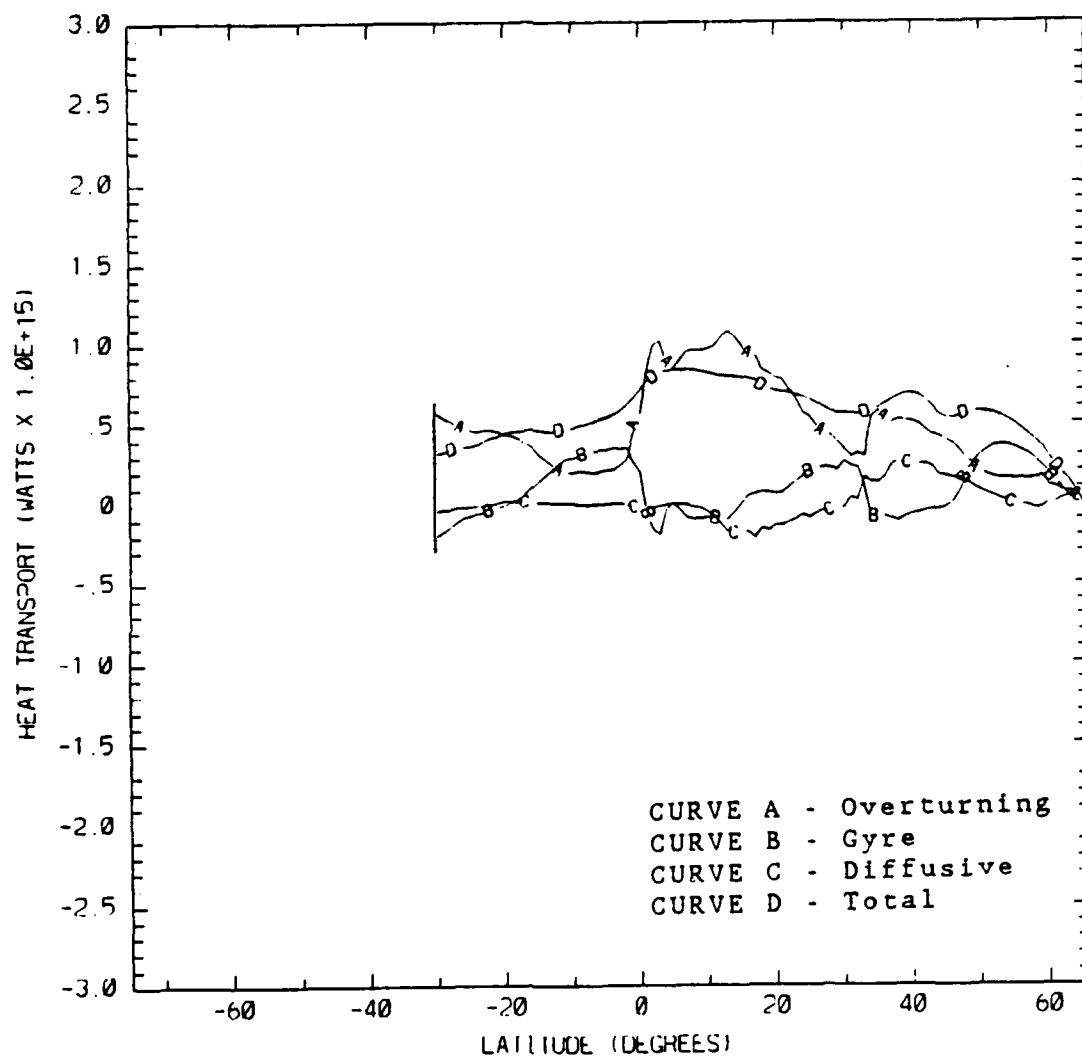


Figure A.3 Same as Figure A.1 but for Atlantic ocean basin.

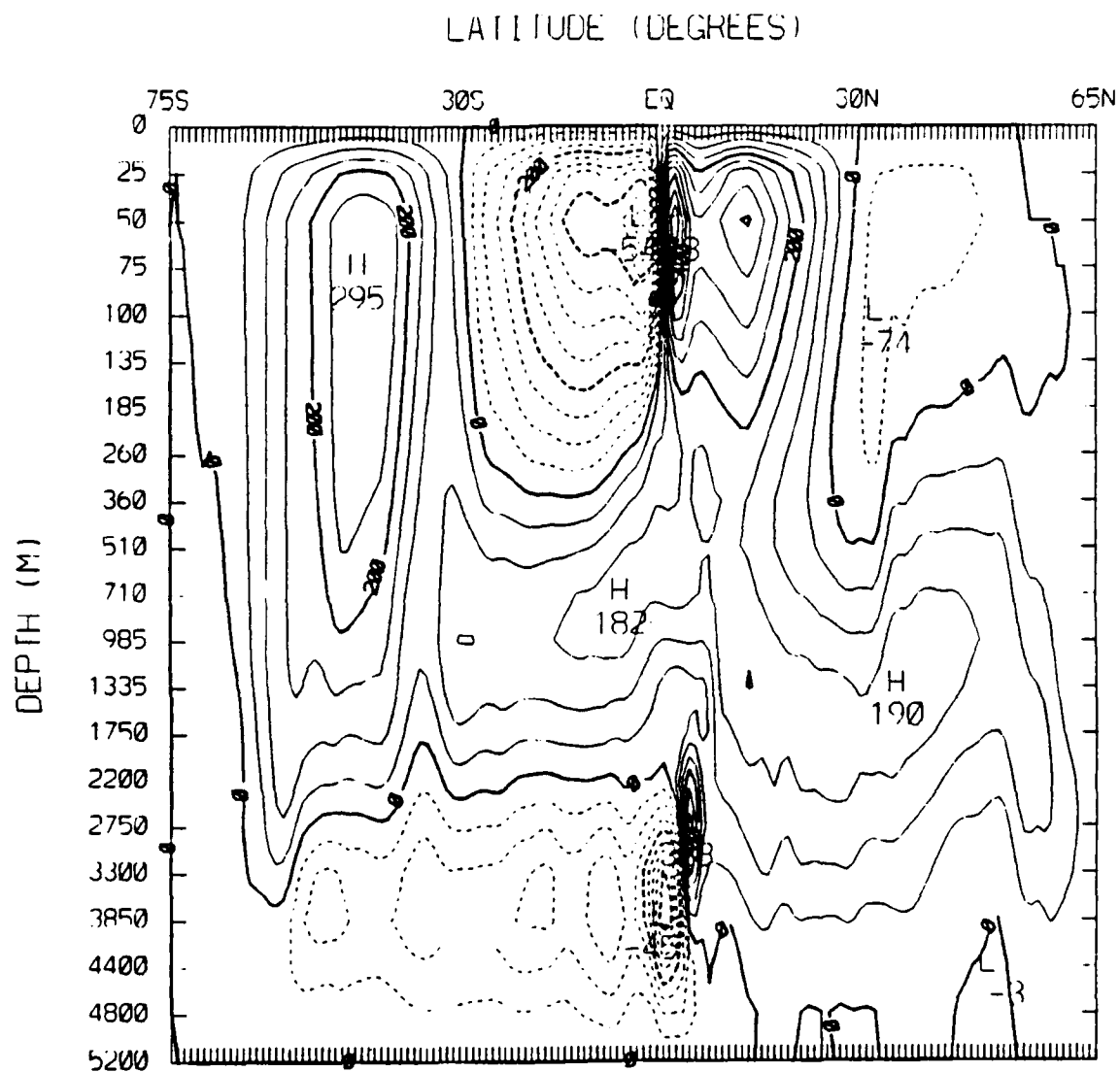


Figure A.4 Global meridional volume transport in units of $10^{11} \text{ cm}^3 \text{ s}^{-1}$ for experiment 1 (positive values clockwise; negative values counterclockwise).

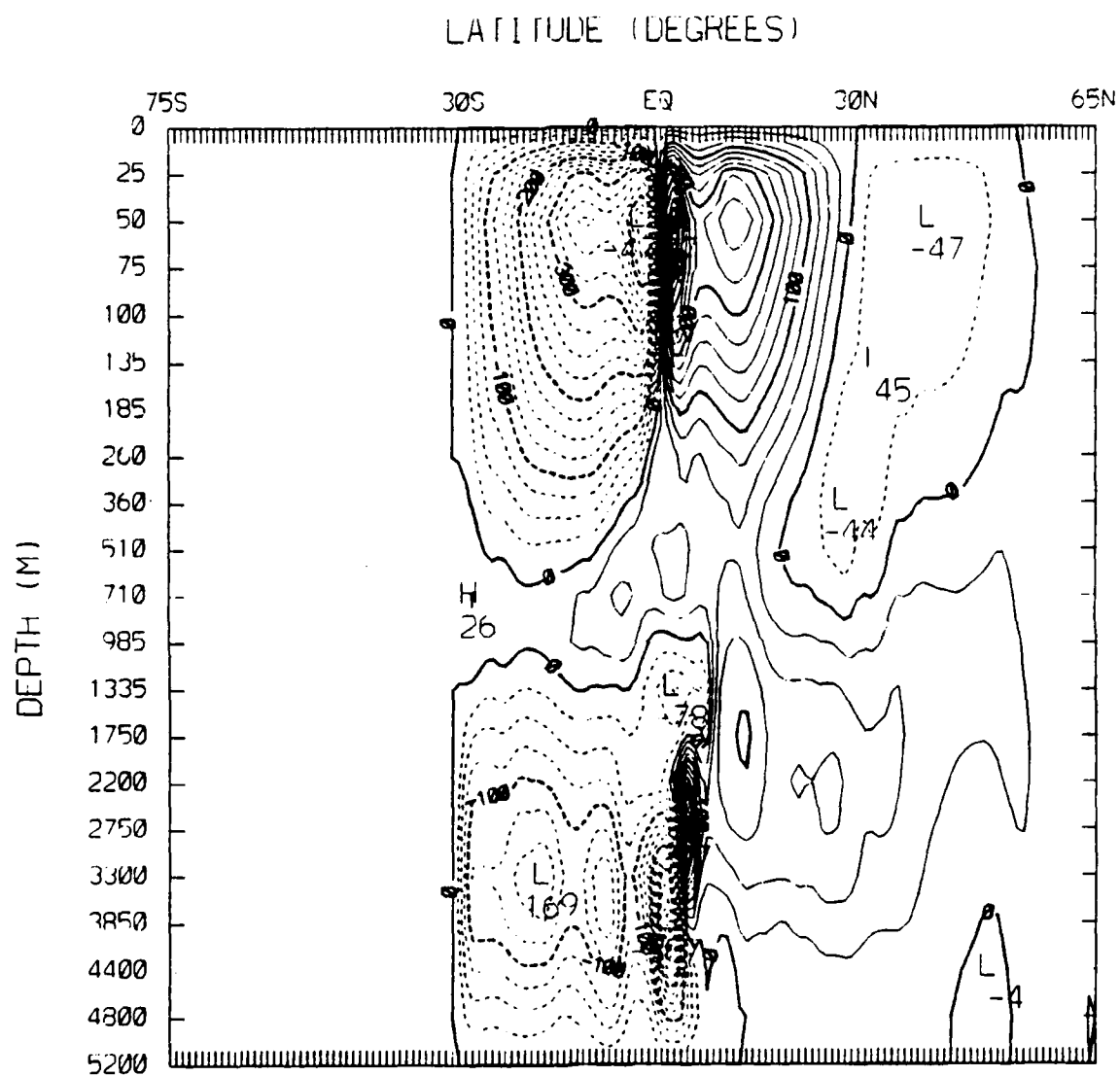


Figure A.5 Same as Figure A.4 but for Indian-Pacific ocean basin.

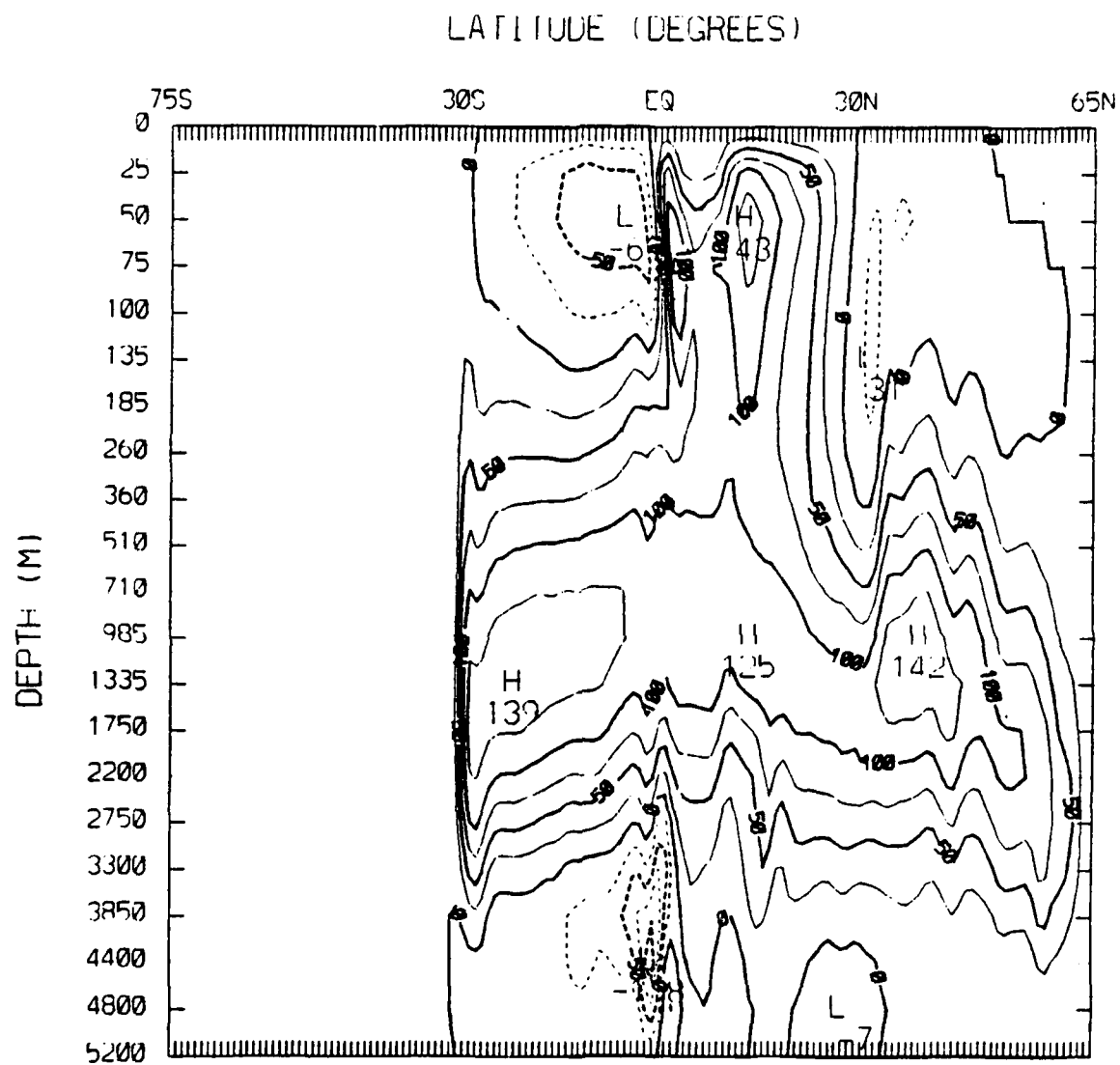


Figure A.6 Same as Figure A.4 but for Atlantic ocean basin.

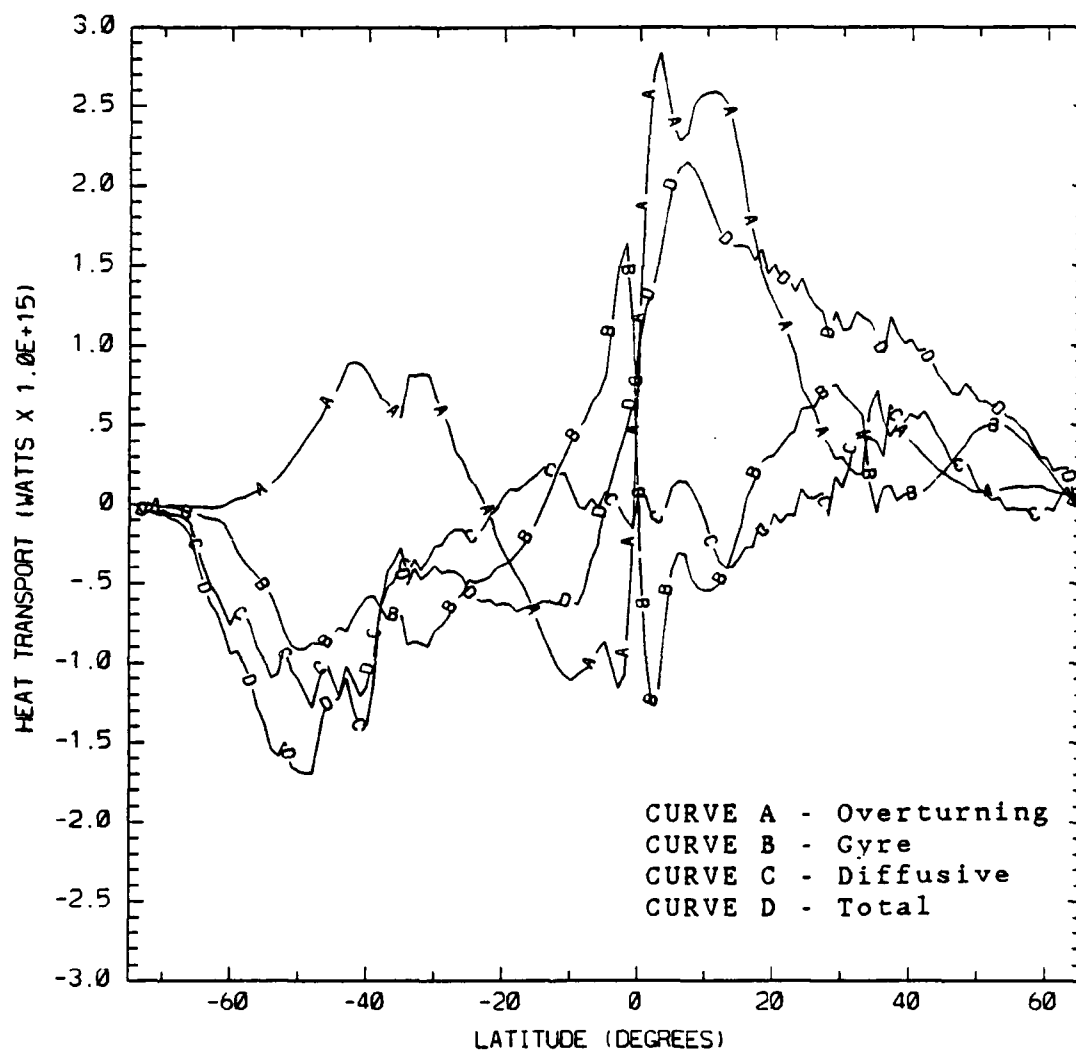


Figure A.7 Global meridional heat transport for experiment 2 (positive values northward; negative values southward).

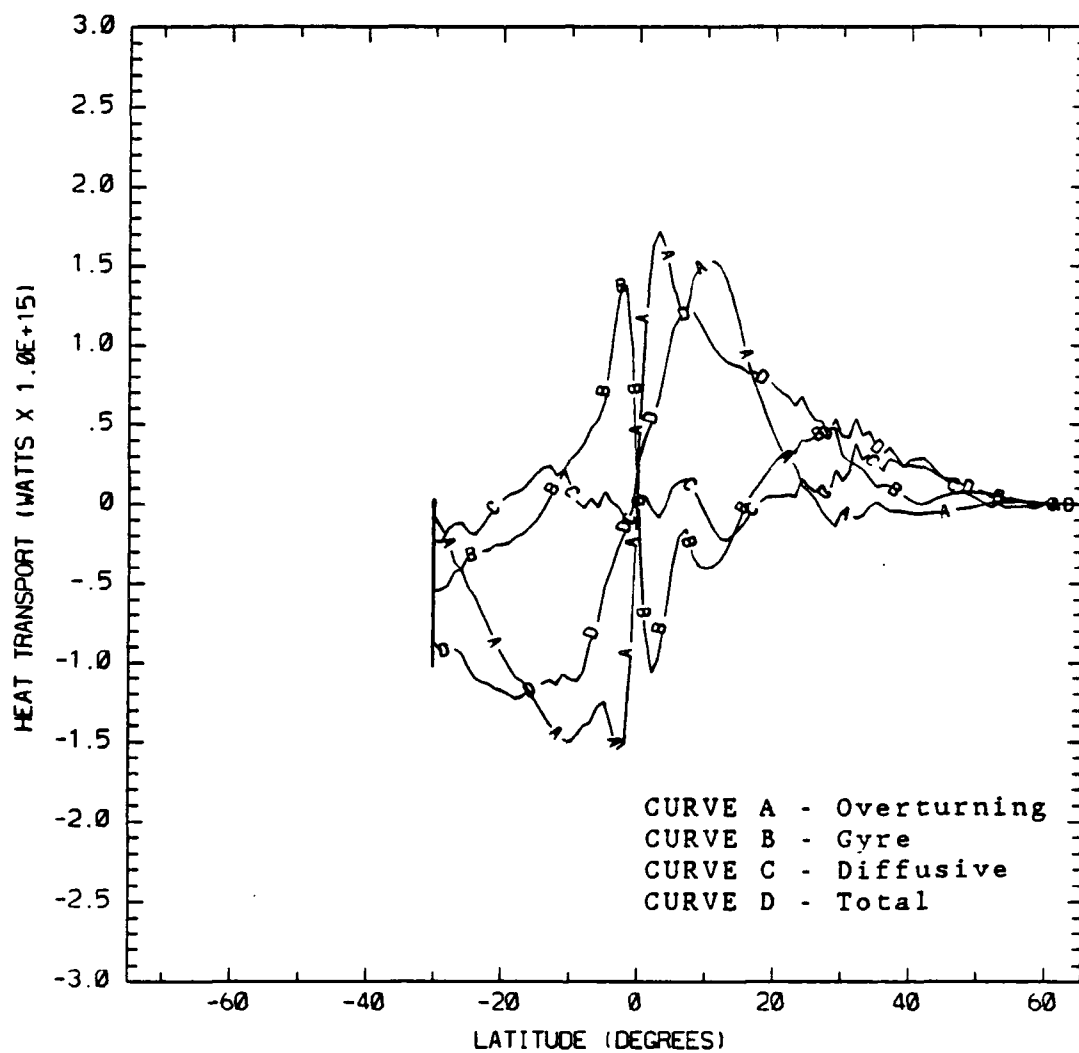


Figure A.8 Same as Figure A.7 but for Indian-Pacific ocean basin.

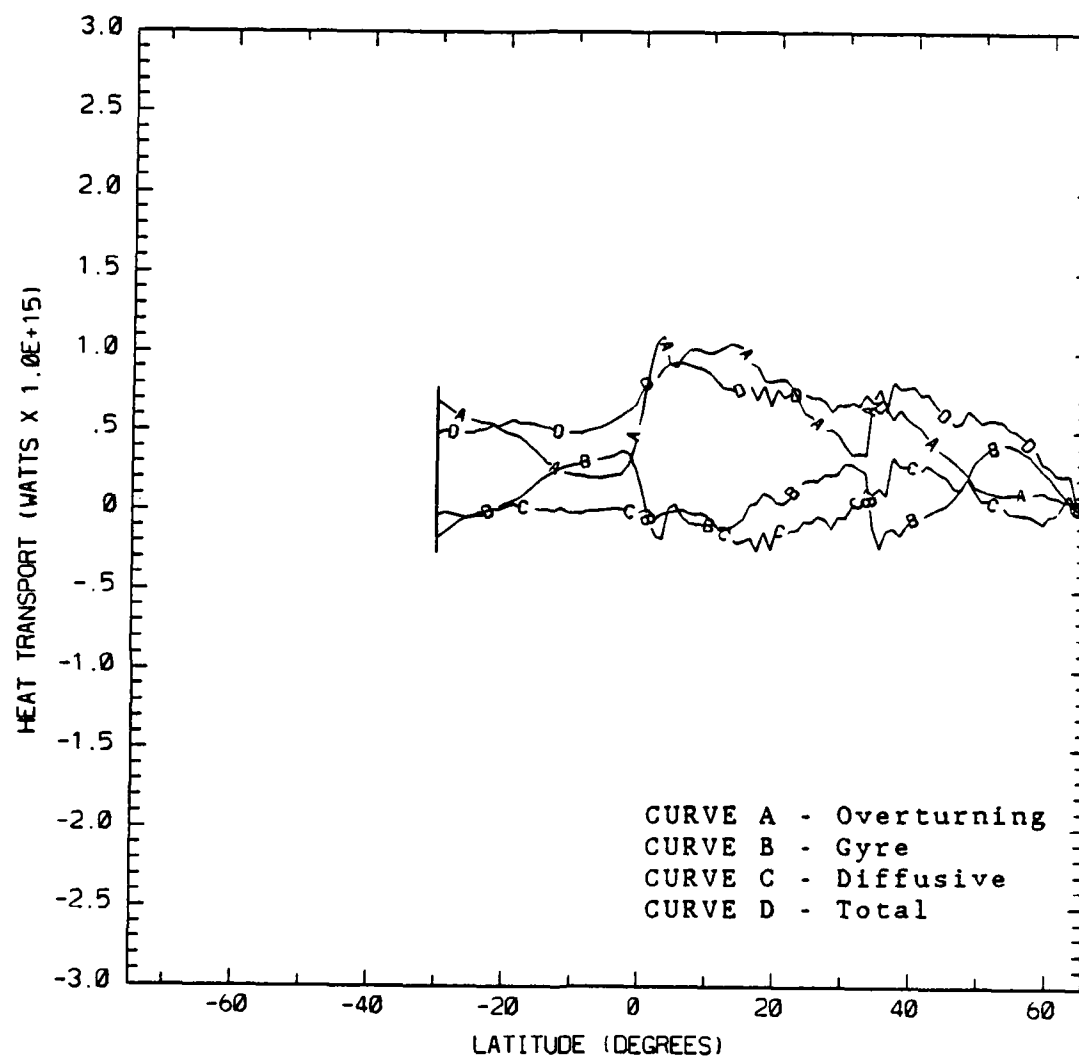


Figure A.9 Same as Figure A.7 but for Atlantic ocean basin.

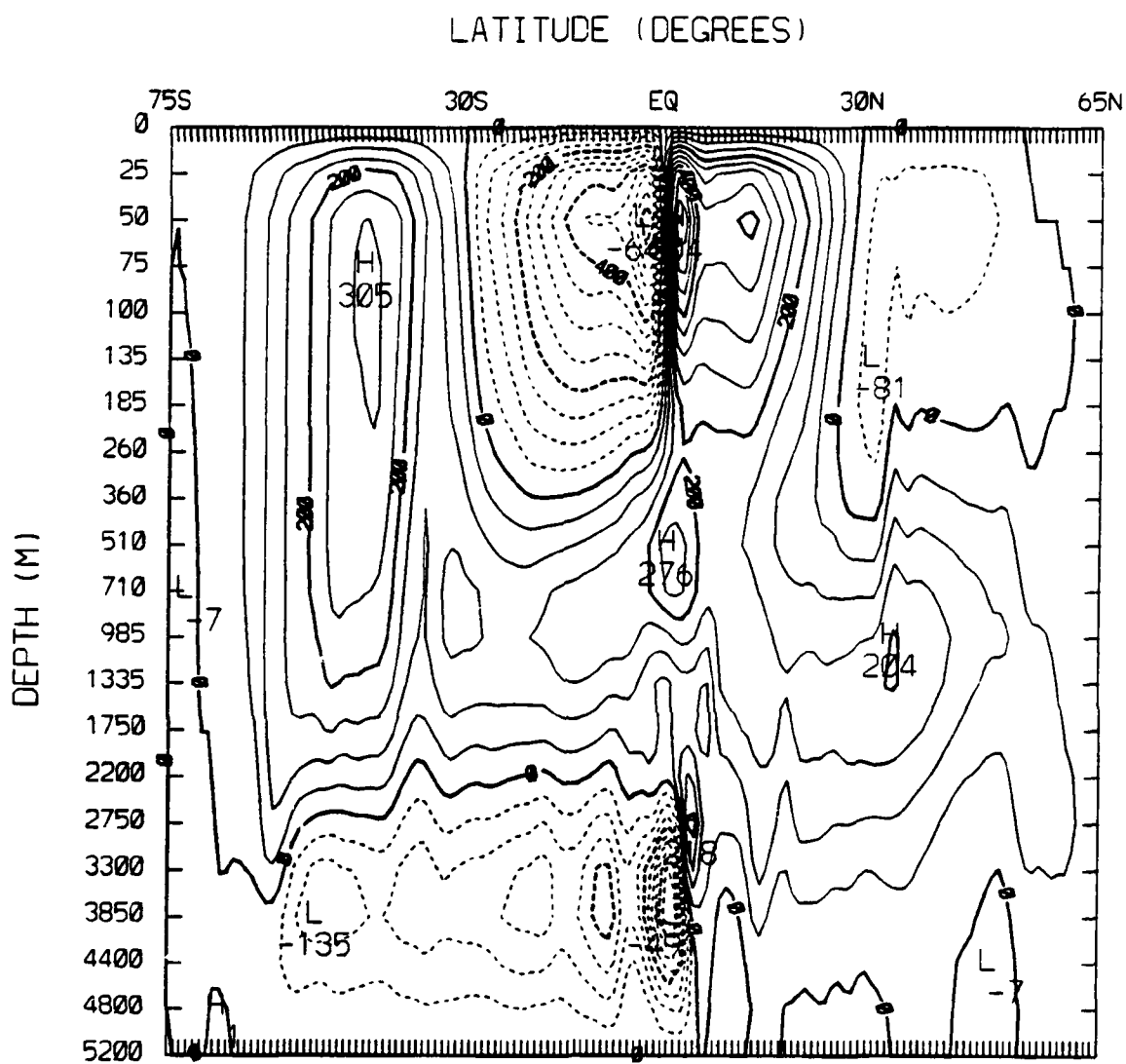


Figure A.10 Global meridional volume transport in units of $10^{11} \text{ cm}^3 \text{ s}^{-1}$ for experiment 2 (positive values clockwise; negative values counterclockwise).

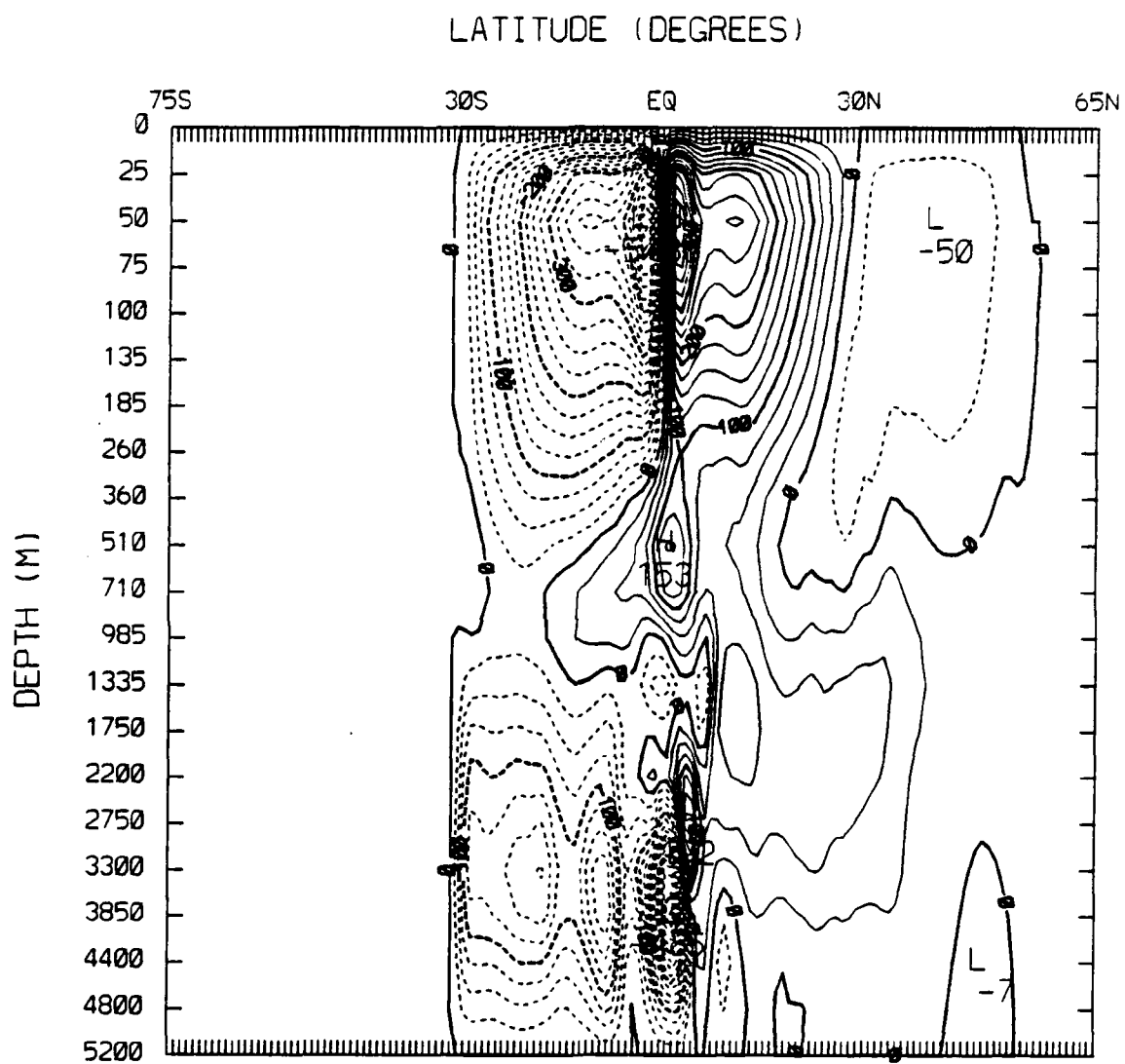


Figure A.11 Same as Figure A.10 but for Indian-Pacific ocean basin.

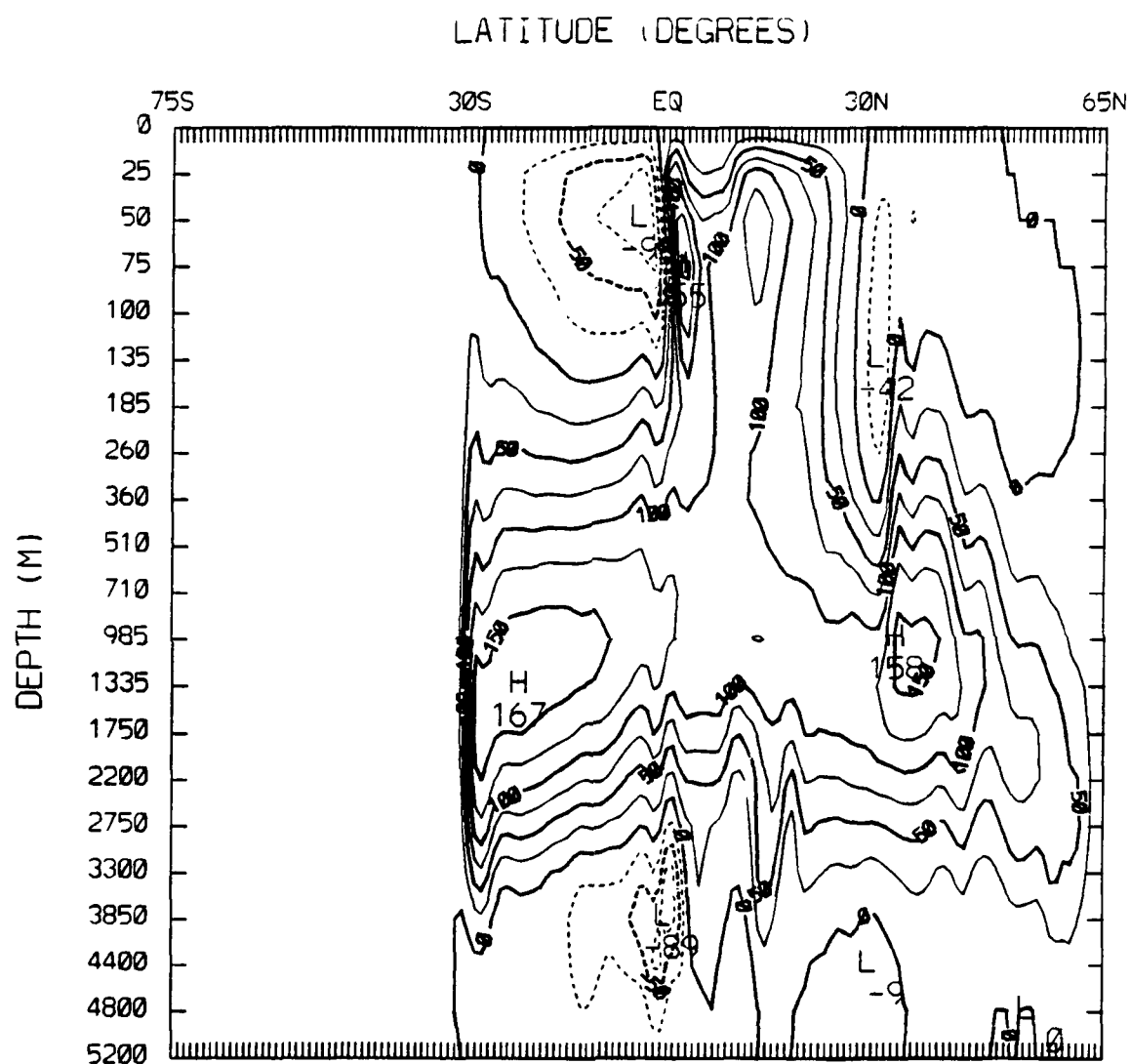


Figure A.12 Same as Figure A.10 but for Atlantic ocean basin.

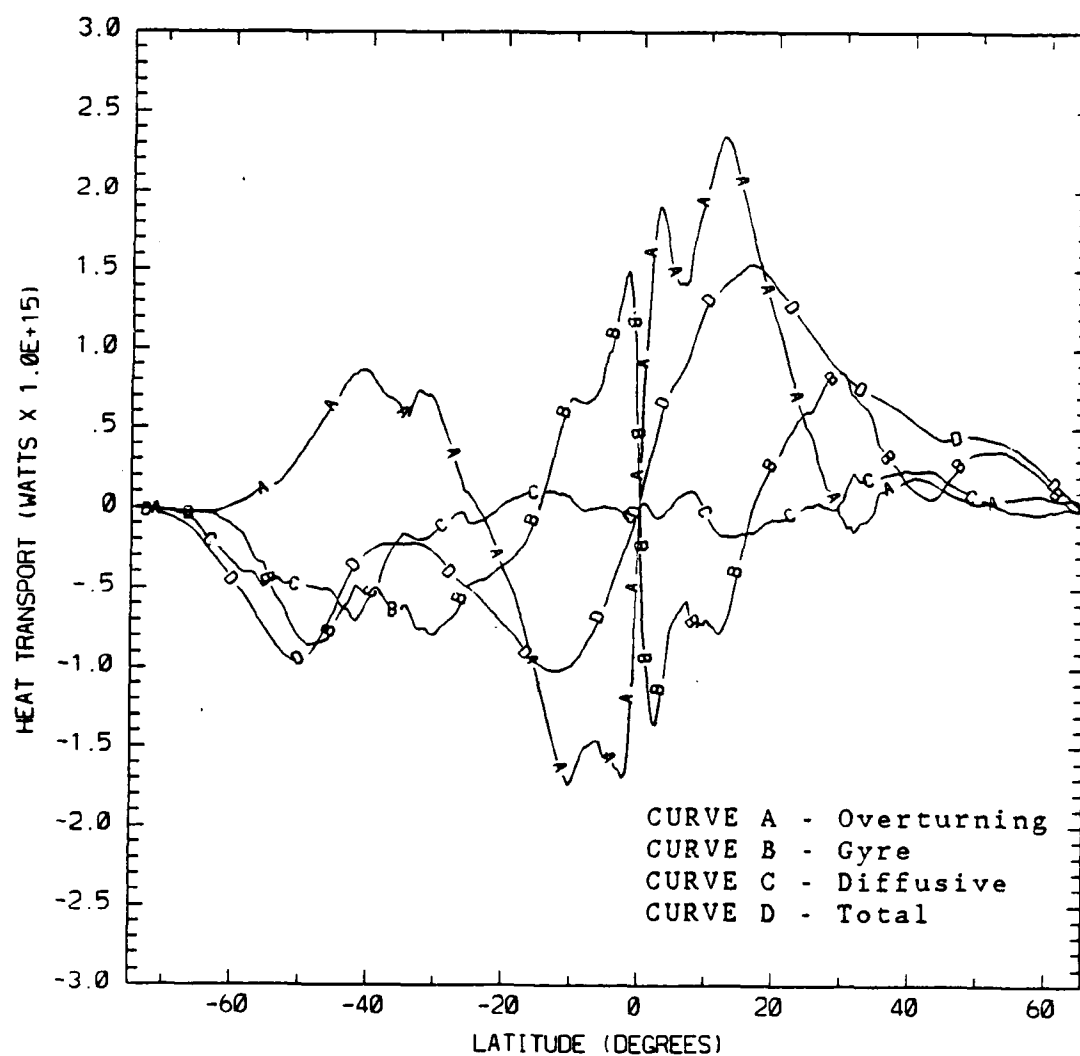


Figure A.13 Global meridional heat transport for experiment 3 (positive values northward; negative values southward).

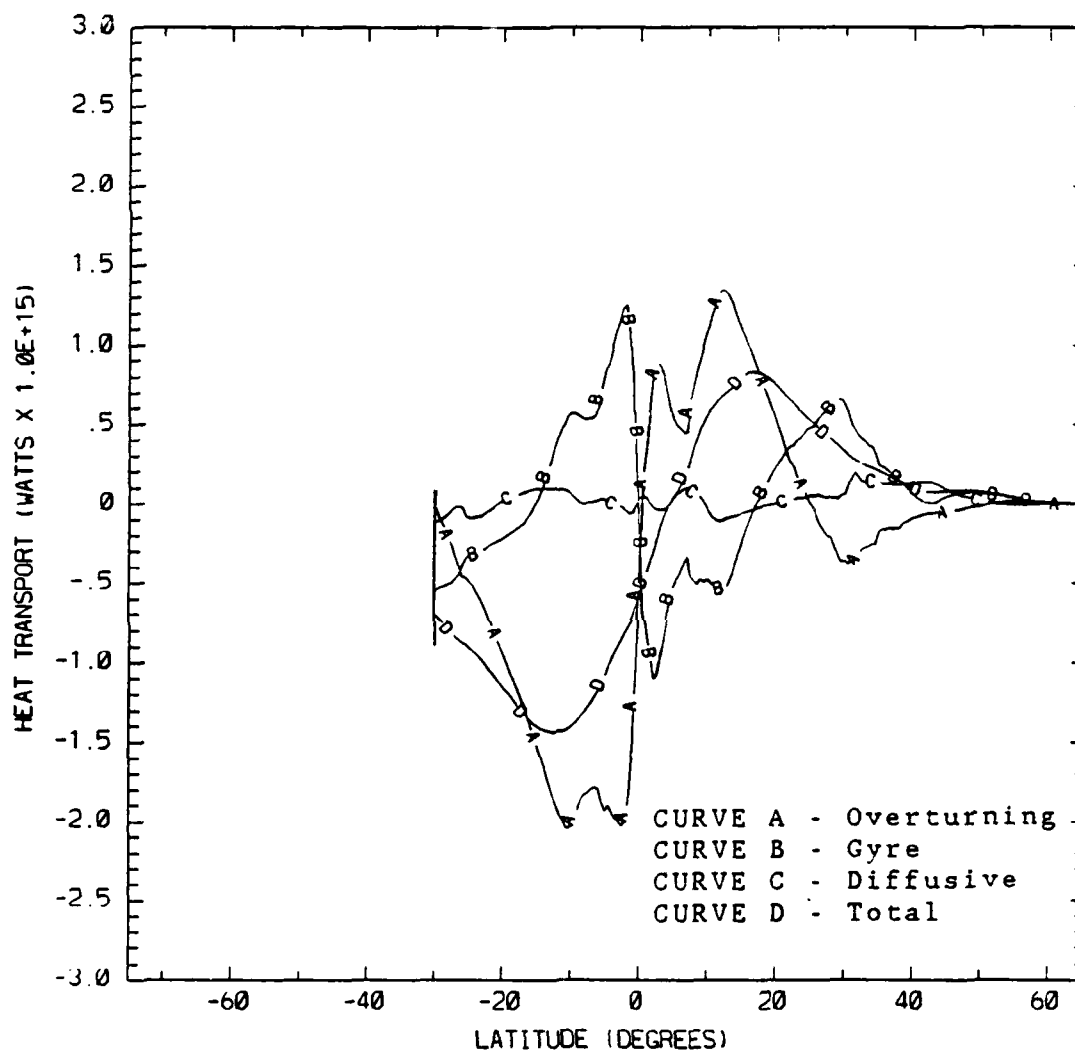


Figure A.14 Same as Figure A.13 but for Indian-Pacific ocean basin.

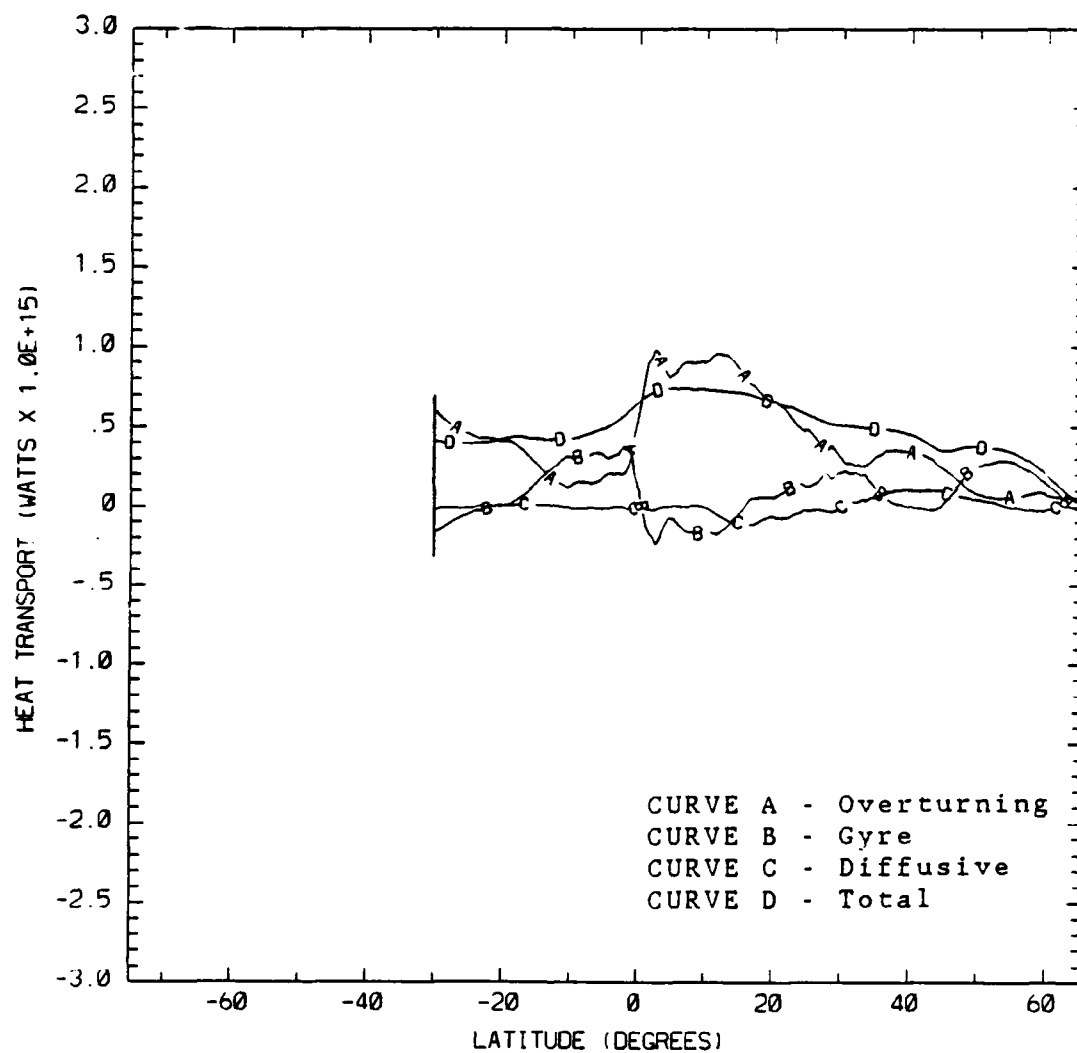


Figure A.15 Same as Figure A.13 but for Atlantic ocean basin.

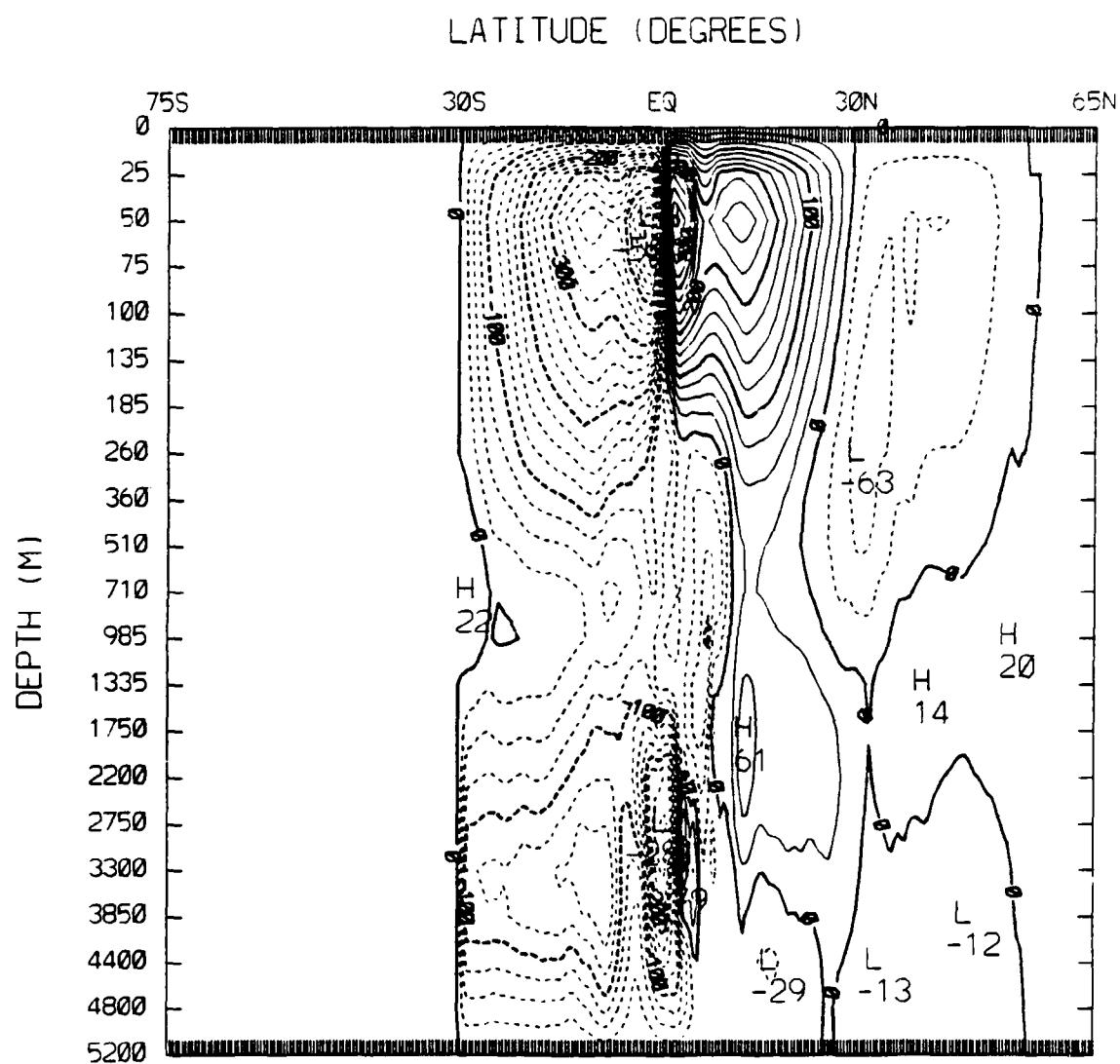


Figure A.17 Same as Figure A.16 but for Indian-Pacific ocean basin.

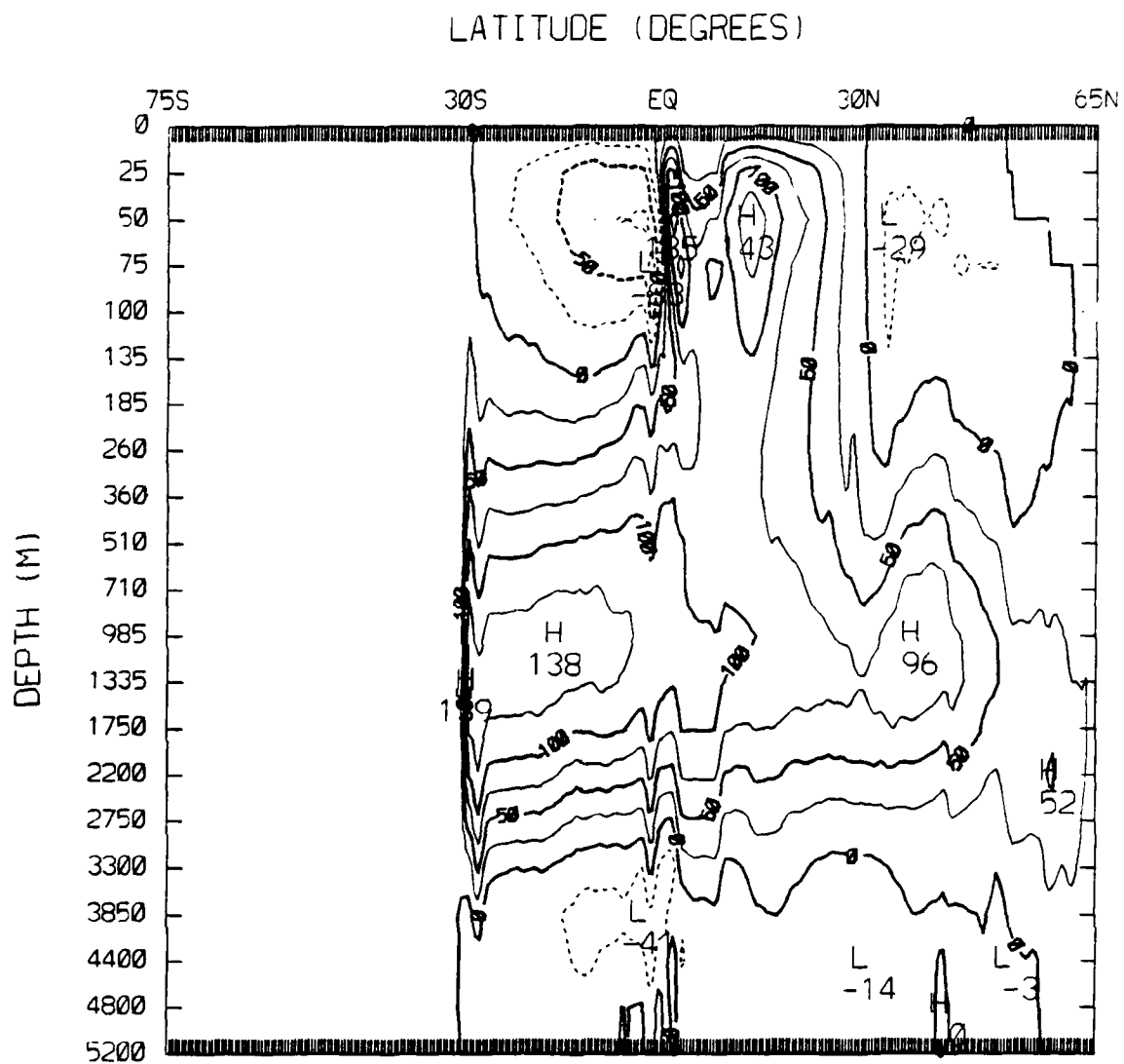


Figure A.18 Same as Figure A.16 but for Atlantic ocean basin.

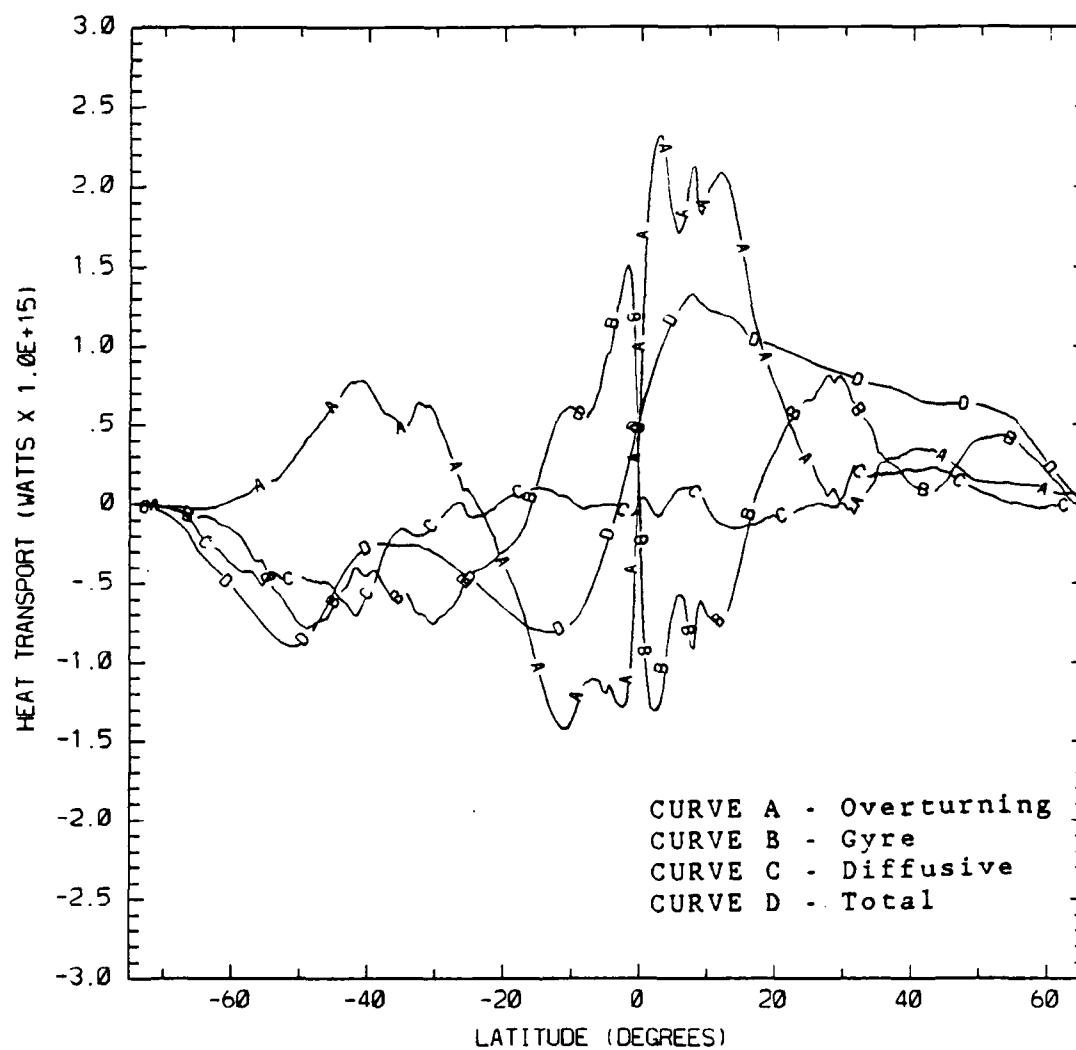


Figure A.19 Global meridional heat transport for experiment 4 (positive values northward; negative values southward).

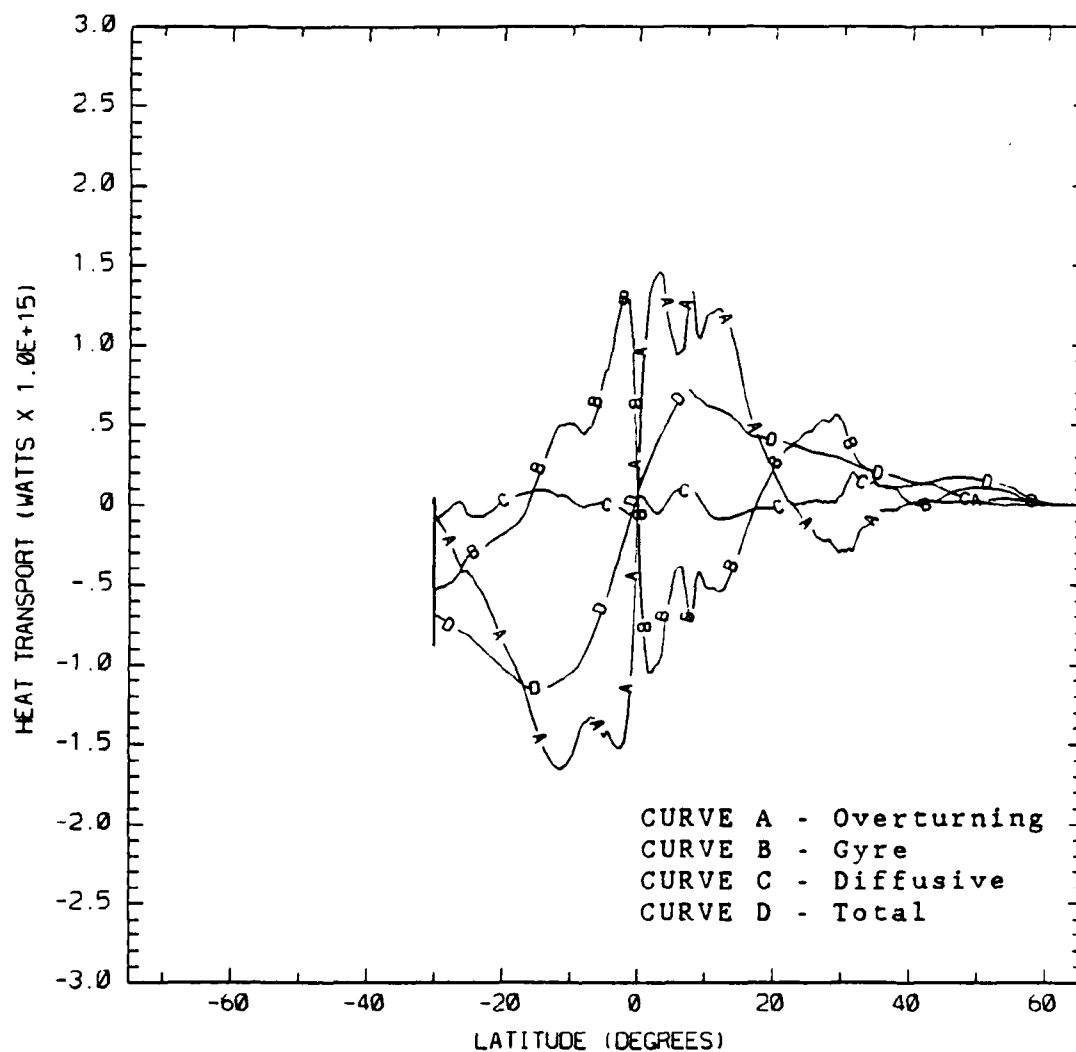


Figure A.20 Same as Figure A.19 but for Indian-Pacific ocean basin.

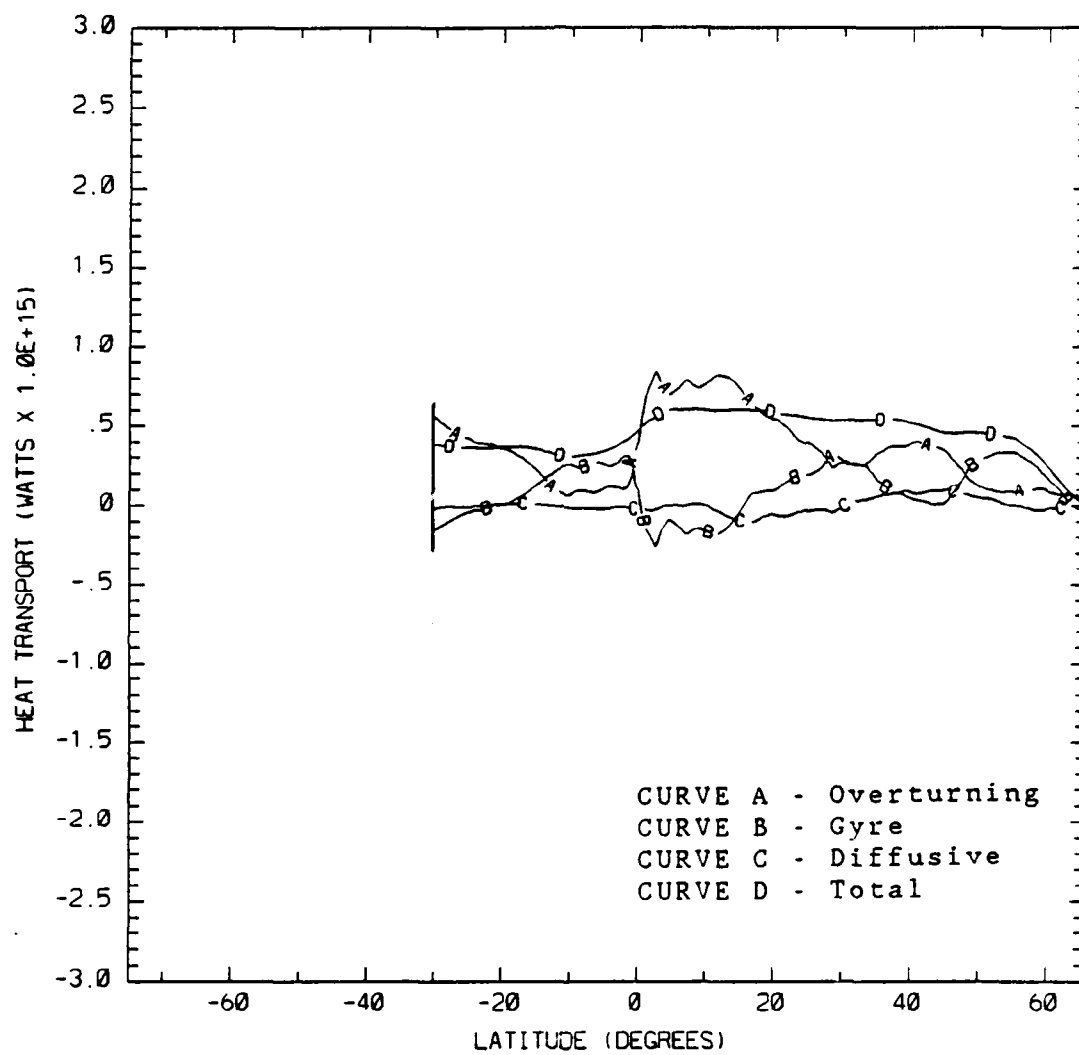


Figure A.21 Same as Figure A.19 but for Atlantic ocean basin.

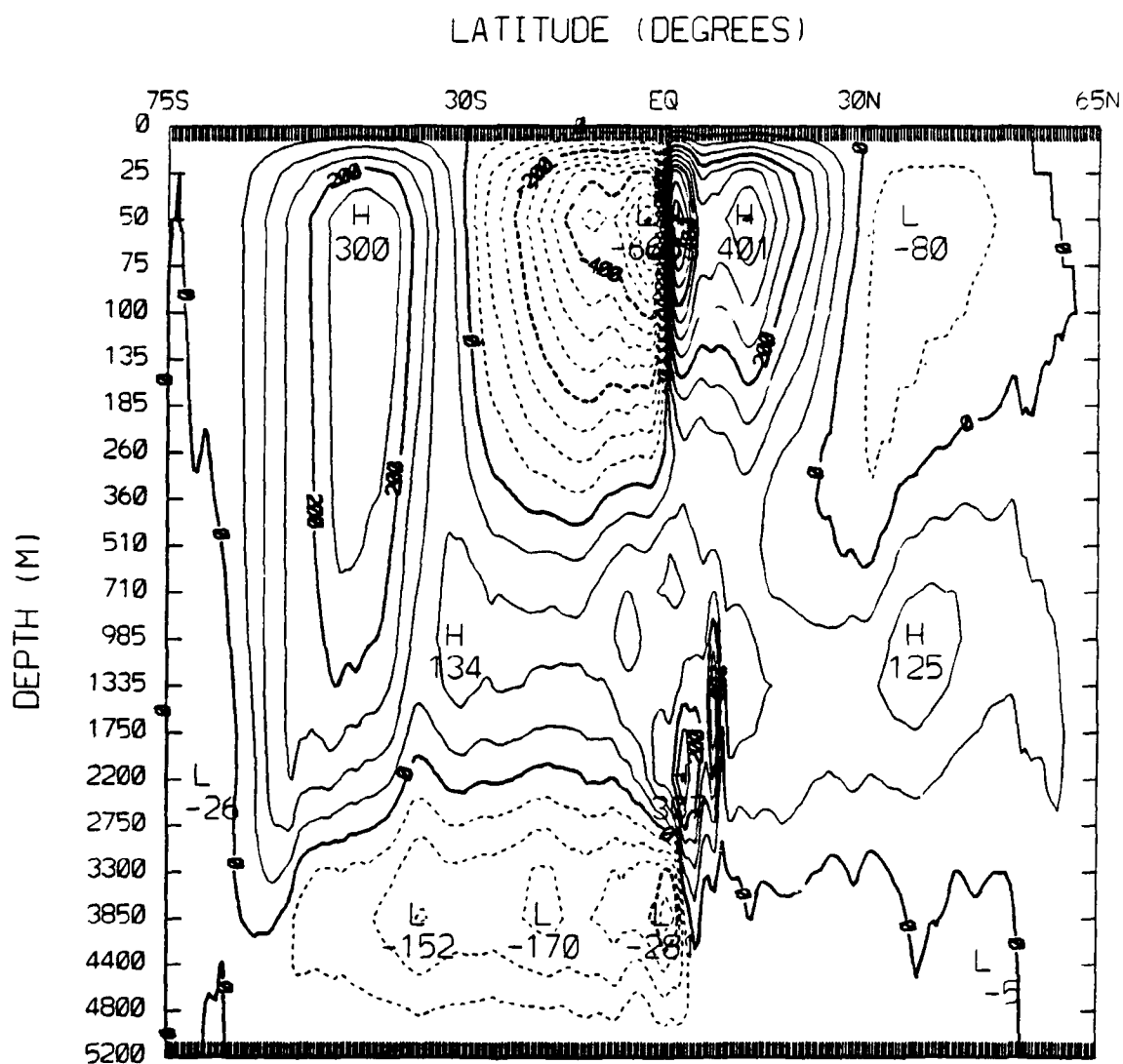


Figure A.22 Global meridional volume transport in units of $10^{11} \text{ cm}^3 \text{ s}^{-1}$ for experiment 4 (positive values clockwise; negative values counterclockwise).

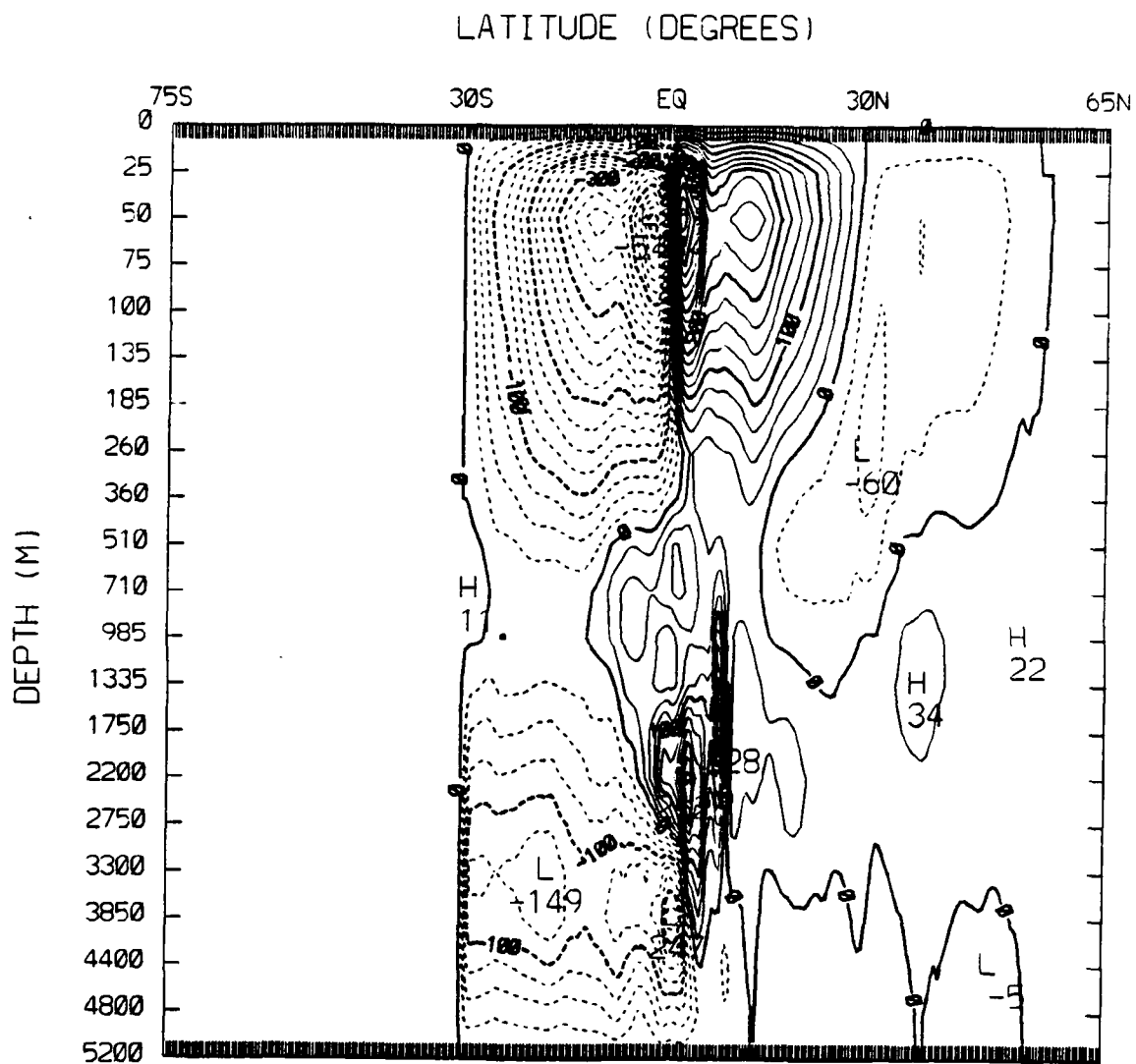


Figure A.23 Same as Figure A.22 but for Indian-Pacific ocean basin.

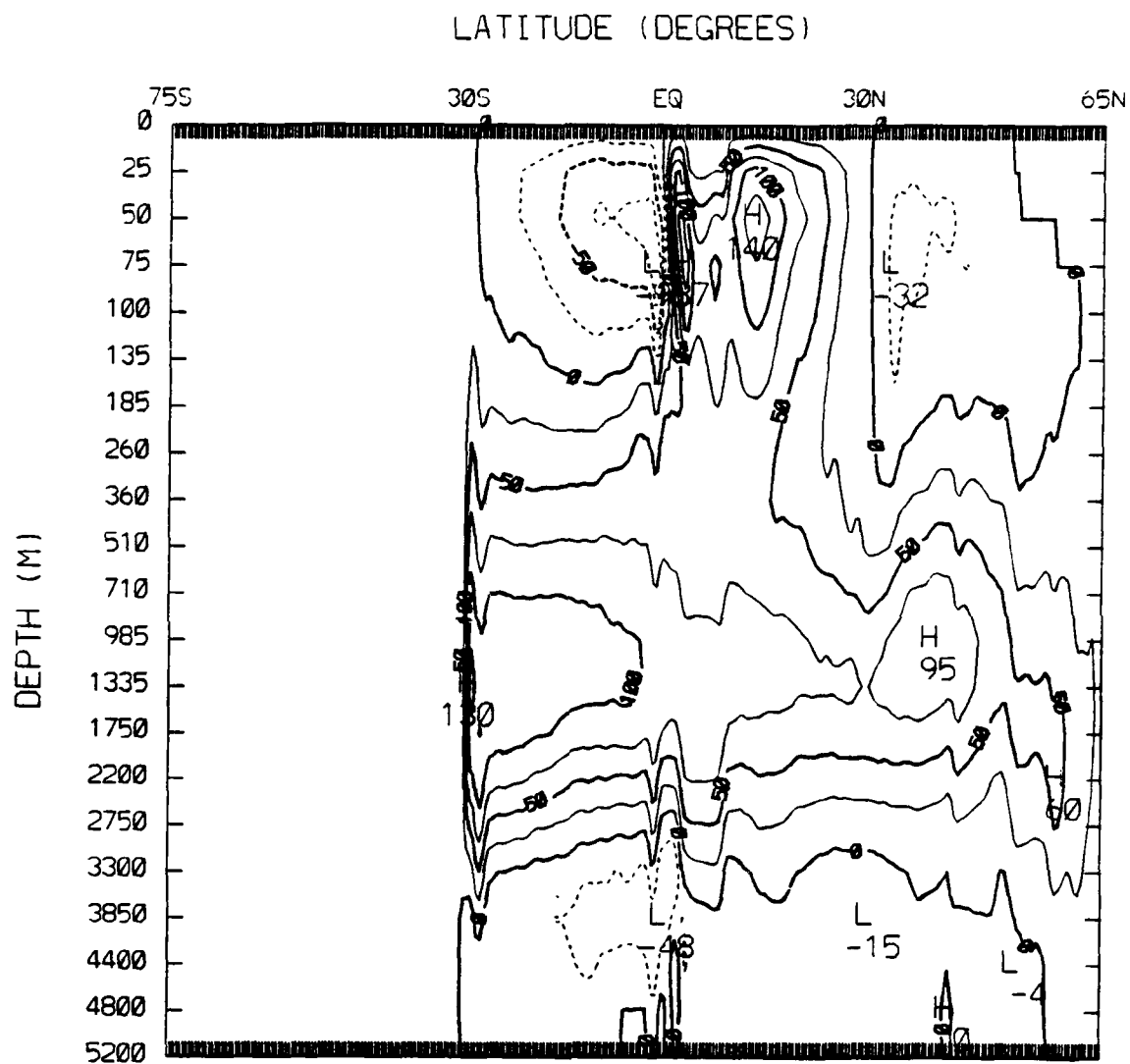


Figure A.24 Same as Figure A.22 but for Atlantic ocean basin.

LIST OF REFERENCES

- Bennett, A.F., 1978: Poleward heat fluxes in Southern Hemisphere oceans. J. Phys. Oceanogr., 8, 785-798.
- Bettge, T., 1987: An ocean model processor for climate studies. NCAR Tech. Note TN-279+1A, 31 pp.
- Bryan, F., 1986: High-latitude salinity effects and interhemispheric thermohaline circulations. Nature, 323, 301-304.
- Bryan, K., 1969: A numerical model for the study of the world ocean. J. Computat. Phys., 4, 347-376.
- _____, 1982: Poleward heat transport by the ocean: observations and models. Annu. Rev. Earth Planet Sci., 10, 15-38.
- _____, and L.J. Lewis, 1979: A water mass model of the world ocean. J. Geophys. Res., 84, 2503-2517.
- Bryden, H.L., 1979: Poleward heat flux and conversion of available potential energy in the Drake Passage. J. Mar. Res., 37, 1-22.
- _____, and M.M. Hall, 1980: Heat transport by currents across 25°N latitude in the Atlantic Ocean. Science, 207, 884-886.
- Cox, M.D., 1975: A baroclinic numerical model of the world ocean: preliminary results. In Numerical models of ocean circulation, National Academy of Sciences, Washington, D.C., 107-120.
- _____, 1984: A primitive equation three-dimensional model of the ocean. GFDL Ocean Group Tech. Rep. No. 1, GFDL/NOAA, Princeton University, Princeton, 250 pp.
- Fu, L.-L., 1981: The general circulation and meridional heat transport of the subtropical South Atlantic determined by inverse methods. J. Phys. Oceanogr., 11, 1171-1193.
- Godfrey, J.S., and T.J. Golding, 1981: The Sverdrup relation in the Indian Ocean, and the effect of Pacific-Indian Ocean throughflow on Indian Ocean circulation and on the East Australian Current. J. Phys. Oceanogr., 11, 771-779.
- Gordon, A.L., 1971: Oceanography of Antarctic Waters. In Antarctic Oceanology I, Antarctic Res. Ser., 15, edited by J.L. Reid. American Geophysical Union, Washington, D.C., 169-203.

- _____, 1985: Indian-Atlantic transfer of thermocline water at the Agulhas Retroflection. Science, 227, 1030-1033.
- Hastenrath, S., 1982: On meridional heat transports in the world ocean. J. Phys. Oceanogr., 12, 922-927.
- Hellerman, S., and M. Rosenstein. 1983: Normal monthly wind stress over the world ocean with error estimates. J. Phys. Oceanogr., 13, 1093-1104.
- Hsiung, J., 1985: Estimates of global oceanic meridional heat transport. J. Phys. Oceanogr., 15, 1405-1413.
- Kamenkovich, V.M., M.N. Koshlyakov, and A.S. Monin, 1986: Synoptic Eddies in the Ocean, D. Reidel Publishing Company, Dordrecht, Boston, Lancaster, Tokyo, 443 pp.
- Levitus, S., 1982: Climatological atlas of the world ocean. NOAA Professional Paper No. 13, U.S. Government Printing Office, Washington, D.C., 173 pp., 17 microfiche.
- Meehl, G.A., W.M. Washington, and A.J. Semtner, Jr., 1982: Experiments with a global ocean model driven by observed atmospheric forcing. J. Phys. Oceanogr., 12, 301-312.
- Miller, J.R., G.L. Russell, and L.-C. Tsang, 1983: Annual oceanic heat transports computed from an atmospheric model. Dyn. Atmos. Oceans, 7, 95-109.
- Olson, D.B., and R.H. Evans, 1986: Rings of the Agulhas Current. Deep-Sea Res., 33, 27-42.
- Oort, A.H., and T.H. Vonder Haar, 1976: On the observed annual cycle in the ocean-atmosphere heat balance over the Northern Hemisphere. J. Phys. Oceanogr., 6, 781-800.
- Pacanowski, R., and S.G.H. Philander, 1981: Parameterization of vertical mixing in numerical models of tropical oceans. J. Phys. Oceanogr., 11, 1443-1451.
- Pickard, G.L. and W.J. Emery, 1982: Descriptive Physical Oceanography: An Introduction, Pergamon Press, Oxford, New York, Toronto, Sydney, Paris, Frankfurt, 249 pp.
- Roemmich, D., 1980: Estimation of meridional heat flux in the North Atlantic Ocean by inverse methods. J. Phys. Oceanogr., 10, 1972-1983.
- Sarmiento, J.L., and K. Bryan, 1982: An ocean transport model for the North Atlantic. J. Geophys. Res., 87, 394-408.

- Semtner, A.J., Jr., 1974: An oceanic general circulation model with bottom topography. Numerical Simulation of Weather and Climate, Tech. Rep. No. 9, Department of Meteorology, University of California, Los Angeles, 99 pp.
- _____, 1984: Modeling the ocean in climate studies. Annals of Glaciology, 5, 133-140.
- _____, 1986a: History and methodology of modelling the circulation of the world ocean. In Proceedings of the NATO Advanced Study Institute on Advanced Physical Oceanographic Numerical Modelling, edited by J.J. O'Brien, D. Reidel Publishing Company, Dordrecht, Boston, Lancaster, Tokyo, 23-32.
- _____, 1986b: Finite-difference formulation of a world ocean model. In Proceedings of the NATO Advanced Study Institute on Advanced Physical Oceanographic Numerical Modelling, edited by J.J. O'Brien, D. Reidel Publishing Company, Dordrecht, Boston, Lancaster, Tokyo, 187-202.
- _____, and R.M. Chervin, 1988: A high resolution robust-diagnostic simulation of the global ocean circulation. J. Phys. Oceanogr., in preparation.
- Takano, K., 1974: A general circulation model for the world ocean. Numerical Simulation of Weather and Climate, Tech. Rep. No. 8, Department of Meteorology, University of California, Los Angeles, 47 pp.
- Talley, I.D., 1984: Meridional heat transport in the Pacific Ocean. J. Phys. Oceanogr., 14, 231-241.
- Trenberth, K.E., 1979: Mean annual poleward energy transports by the oceans in the Southern Hemisphere. Dyn. Atmos. Oceans, 4, 57-64.
- Wunsch, C., 1980: Meridional heat flux of the North Atlantic Ocean. Proc. Natl. Acad. Sci., 77, 5043-5047.

INITIAL DISTRIBUTION LIST

	No. Copies
1. Defense Technical Information Center Cameron Station Alexandria, VA 22304-6145	2
2. Library, Code 0142 Naval Postgraduate School Monterey, CA 93943-5002	2
3. Chairman (Code 68Co) Department of Oceanography Naval Postgraduate School Monterey, CA 93943-5100	1
4. Chairman (Code 63Rd) Department of Meteorology Naval Postgraduate School Monterey, CA 93943-5100	1
5. Prof. A. J. Semtner (Code 68Se) Department of Oceanography Naval Postgraduate School Monterey, CA 93943-5100	1
6. Prof. D. C. Smith, IV (Code 68Si) Department of Oceanography Naval Postgraduate School Monterey, CA 93943-5100	1
7. Prof. M. L. Batteen (Code 68Bv) Department of Oceanography Naval Postgraduate School Monterey, CA 93943-5100	1
8. LCDR Wesley A. Barton Commander Submarine Group 5 158 Sylvester Road San Diego, CA 92106	2
9. Director Naval Oceanography Division Naval Observatory 34th and Massachusetts Avenue NW Washington, DC 20390	1

- | | |
|---|---|
| 10. Commander
Naval Oceanography Command
NSTL Station
Bay St. Louis, MS 39522 | 1 |
| 11. Commanding Officer
Naval Oceanographic Office
NSTL Station
Bay St. Louis, MS 39522 | 1 |
| 12. Commanding Officer
Fleet Numerical Oceanography Center
Monterey, CA 93943 | 1 |
| 13. Commanding Officer
Naval Ocean Research and Development Activity
NSTL Station
Bay St. Louis, MS 39522 | 1 |
| 14. Office of Naval Research (Code 420)
800 N. Quincy Street
Arlington, VA 22217 | 1 |
| 15. Commanding Officer
Naval Environmental Prediction Research Facility
Monterey, CA 93943 | 1 |
| 16. Chairman, Oceanography Department
U.S. Naval Academy
Annapolis, MD 21402 | 1 |
| 17. Dr. B. Buzbee, Director
Scientific Computing Division
National Center for Atmospheric Research
Boulder, CO 80307-3000 | 1 |
| 18. Dr. W. Washington, Director
Climate and Global Dynamics Division
National Center for Atmospheric Research
Boulder, CO 80307-3000 | 1 |
| 19. Dr. R. M. Chervin
Climate and Global Dynamics Division
National Center for Atmospheric Research
Boulder, CO 80307-3000 | 1 |
| 20. Mr. T. Bettge
Climate and Global Dynamics Division
National Center for Atmospheric Research
Boulder, CO 80307-3000 | 1 |

21. Dr. C. N. K. Mooers, Director 1
Institute for Naval Oceanography
Bldg. 1100, room 311
NSTL Station
Bay St. Louis, MS 39529
22. Dr. T. Spence, Director 1
Physical Oceanography Program
National Science Foundation
Washington, DC 20550
23. Dr. M. R. Riches 1
U.S. Department of Energy, ER-12
Carbon Dioxide Research Division
Washington, DC 20545
24. Prof. W. L. Gates 1
Climate Research Institute
Oregon State University
Corvallis, OR 97330
25. Prof. A. R. Robinson 1
Division of Applied Sciences
Pierce Hall, room 100D
Harvard University
29 Oxford Street
Cambridge, MA 02138
26. Prof. J. J. O'Brien 1
Department of Meteorology
Meteorology Annex
435 PSA Bldg.
Florida State University
930 Wildwood
Tallahassee, FL 32306
27. Dr. K. Bryan 1
Geophysics Fluid Dynamics Program
Princeton University GF04
Princeton University
P.O. Box 308
Princeton, NJ 08540

END

DATE

FILMED

9-88

DTIC